THEORETICAL AND NUMERICAL INVESTIGATION ON VIBRATIONAL NONEQUILIBRIUM EFFECT IN DETONATION

UY CHUN KIT

PhD

The Hong Kong Polytechnic University

2021

The Hong Kong Polytechnic University

Department of Mechanical Engineering

THEORETICAL AND NUMERICAL INVESTIGATION ON VIBRATIONAL NONEQUILIBRIUM EFFECT IN DETONATION

Uy Chun Kit

A thesis submitted in partial fulfillment of the requirements for the degree
of Doctor of Philosophy

June, 2020

Certificate of Originality

I hereby declare that this thesis is my own work and that, to the best of my knowledge and belief, it reproduces no material previously published or written, nor material that has been accepted for the award of any other degree or diploma, except where due acknowledgement has been made in the text.

_____

Uy Chun Kit, Ken

Abstract

This thesis attempts to elucidate the effect of vibrational nonequilibrium in detonation by theoretically modelling. A simplified vibrational-chemical coupling mechanism is constructed by correlating single-step/two-step Arrhenius equations (denoting chemical reaction) and the Landau-Teller model (denoting vibrational relaxation) with Park's two-temperature model. Two issues are demonstrated based on these coupling kinetics, which include 1) the extension of the ZND detonation model to predict half-reaction length when detonation is under significant vibrational nonequilibrium and 2) the stability behaviour of detonation under significant vibrational nonequilibrium. A time ratio denoting the ratio of chemical reaction time scale and the vibrational relaxation time scale is utilized throughout this study and it represents the different state of vibrational nonequilibrium. In the first half of the thesis, it is concluded that the elongation of half reaction length at the state of nonequilibrium is observed due to the reduction of overall chemical reaction rate, whereas in the second half of the thesis, it is shown that the detonation is stabilized at vibrational nonequilibrium state through a normal mode linear stability analysis. The results obtained in the analytical approach are compared with that using a numerical approach by CE/SE scheme, and these findings are well verified. The theoretical derivation in the detonation model indicates that vibrational nonequilibrium and thus the vibrational-chemical coupling mechanism plays an important role in gaseous detonation physics and should be examined further in future detonation simulations.

Acknowledgements

I would first like to thank my supervisor Prof. WEN Chih-Yung, who provided me an opportunity to join his team as an internship first and continued the work in my Ph.D. study. His patient guidance helped me in all the time of research and writing of this thesis. I would also like to thank Dr. SHI Lisong and Dr. SHEN Hua for their insightful comment and encouragement in the research, and every colleague from the High-speed Thermo-fluid and MAV/UAV Laboratory. Last but not least, I would like to thank my family and friends for supporting me spiritually throughout the writing of this thesis and my life in general.

Table of Contents

List of Figures

List of Tables

Nomenclature

C_v	Heat capacity at constant volume
E	Total specific energy
e	Total specific internal energy
E_a	Activation energy
$E_{a,ind}$	Activation energy for induction model
$E_{a,r}$	Activation energy for reaction model
e_v	Specific vibrational energy
f	Degree of overdrive
h	Specific enthalpy
h^f	Specific enthalpy of formation
k_b	Backward reaction rate
k_c	Equilibrium constant
k_f	Forward reaction rate
k_{ind}	Pre-exponential factor for induction model
k_r	Pre-exponential factor for reaction model
$\mathcal{L}_{1/2}$	Half-reaction length
$\mathcal{L}_{ind}$	Induction zone length
$\mathcal{L}_r$	Reaction zone length
M	Mach number
MW	Molecular weight of species
N	Molar mass of species
p	Pressure
Q	Heat of reaction
R	Universal gas constant
s^0	Standard state specific entropy
t	Time
T_{tr}	Translational-rotational temperature
T_v	Vibrational temperature
u	Velocity
v'_k	Stoichiometric coefficient (forward)
v''_k	Stoichiometric coefficient (backward)
x	Propagation length
Y	Molar fraction for the corresponding species
α	Disturbance eigenvalue
β	Reaction progress variable for induction model

Nomenclature

γ	Specific heat ratio
ϵ	Degree of freedom of molecules/atoms
η	Characteristic vibrational temperature normalized with post-shock state
ϑ	Characteristic vibrational temperature
λ	Reaction progress variable for reaction model (Mass fraction of product)
μ	Reduced mass
ρ	Density
ϱ	Heat of reaction normalized with post-shock state
τ_c	Chemical reaction time
τ_{v}	Vibrational relaxation time
$\tau^{c/\mathrm{v}}$	Time ratio of chemical time scale versus vibrational time scale
υ	Specific volume
ϕ	Activation energy normalized with post-shock state
χ	Ratio of translational-rotational energy versus the total internal energy in terms of specific heats at constant volume
ψ	Perturbation to the shock
ω_{v}	Rate change for vibrational relaxation model
ω_β	Rate change for induction model
ω_λ	Rate change for reaction model
Superscript	
$-$	Dimensional form
Subscript	
avg	Geometric average
eq	Thermal equilibrium state
Neq	Vibrational nonequilibrium state
s	Post-shock state
tr	Translation-rotational mode
v	Vibrational mode
vn	von Neumann state
0	Initial reactant state or pre-shock state

Chapter 1 Introduction

Detonation is a supersonic combustion wave induced by shock and has been studied for over 100 years. With the abrupt increase in pressure and temperature due to the shock compression, the combustion of reactant is initiated, and the reactant is transformed into products through a heat release process. The continuous energy production through the chemical reactions sustained the propagation of shock wave and thus the detonation.

Safety of gaseous detonation is always a concern in various engineering applications, such as mine gas explosions, combustible gas (i.e. natural gas) leakage, and hydrogen-combustion in the nuclear plant. Because of the high thermodynamic efficiency in detonation, application in pulse detonation engine design is possible and has been studied over decades through various modelling and simulation [1, 2]. In recent years, phenomena of deflagration to detonation transition (DDT) has also been applied in studying Type Ia supernova explosion [3]. All these findings relied on the understanding of fundamental detonation physics.

1.1   Classic detonation theory

Historically, detonation has been discovered since the fifteenth century, but the relative research on this phenomenon is found only until the late seventeenth century. In the 1880s, Rankine and Hugoniot analyzed the conservation equations between the states on both sides of a shock wave. At the same time, several studies have been conducted to measure the detonation velocity in a variety of fuels and demonstrated that the supersonic detonation waves are different from that of the deflagration wave [4, 5]. Right after their work, a theory estimating the detonation velocity of an explosive mixture was formulated by Chapman and Jouguet in the early twentieth century. By assuming infinitely fast chemical reactions across the detonation wave and the establishment of chemical equilibrium at the downstream side, the Chapman-Jouguet (CJ) theory aims to provide an insight in predicting the minimum detonation velocity for a reactant at a given initial condition. Data from many up-to-date experiments still show that the approximation of detonation speeds by CJ theory is very satisfactory.

However, around the mid-twentieth century, physicists realized that the ignorance of detonation structure within a reaction zone in this simple theory may be crucial in explaining the propagation mechanism of the detonation wave. A well-known

detonation theory named after three scientists, which is the Zel'dovich–von Neumann–Döring (ZND) model [6-8], was then proposed to describe specifically the transition process from reactants to products with a simplified chemical model. A leading shock is presented in the detonation model followed by a heat release zone described by chemical kinetics. As the leading shock wave passes by, the reactant is compressed, and the chemical reaction is initiated after a short induction period. The auto-ignition via adiabatic shock compression continues to provide energy in terms of expansion wave behind the shock front and thus sustains the detonation propagation. With a chosen chemical model (usually the single-step Arrhenius model for simplicity), the ZND equations are integrated across the profile from upstream to downstream and thermodynamic properties can be evaluated within the zone. The concept of progress variable in reaction model is introduced such that different intermediate equilibrium states can be defined in the analysis (in terms of intermediate Hugoniot curve). Overall, the consideration of a detailed transition process and thus the laminar structure of a detonation wave in a one-dimensional ZND model can be regarded as an attempt to provide a more rigorous justification for the CJ theory [9].

However, the steady ZND model is not capable of explaining the multi-dimensional or non-steady detonation wave in experimental observation. Interaction between transverse waves across the leading shock front in self-propagating detonation wave forms a characteristic cellular structure which is attributed to the onset of detonation instabilities. Nevertheless, the analysis of the ZND model is still important as the detonation physics behind can be easily manifested in terms of theoretical derivations.

1.2   Development of detonation stability analysis

In reality, cellular instability in the forms of cell or diamond pattern can be observed when detonation propagates in a two-dimensional rectangular channel [10]. In this context, the ZND wave in multidimensional form is inherently unstable to small perturbations in the flow, since triple points are continuously formed by the interaction between the Mach stem and the incident shock during the wave propagation. The study of detonation stability is therefore important in lots of engineering applications.

Since the direct analysis of stability in a time-dependent three-dimensional detonation is not feasible, researchers seek another way to analyze this problem and linear stability analysis is thus carried out. Erpenbeck is the first one to apply this analytical tool in studying the stability of an idealized detonation via an initial value Laplace transform approach [11-13]. By analyzing the governing equations in the presence of one-

dimensional perturbation, the overall stability behavior is demonstrated, and the neutral stability boundary is interpolated in his studies. Fickett & Wood [14] has computed the same case in one-dimensional form using the method of characteristics and found that the results agreed with each other. However, information regarding the number of unstable modes, the disturbance growth rate, and frequency are not revealed completely in these researches. Those details have not been addressed until 1990, when Lee & Stewart [15] analyze the same problem using the normal mode approach instead, in which the authors applied a numerical shooting technique on the acoustic boundary at the end of the reaction zone. Based on the variation of independent parameters in the model (i.e., the activation energy and the degree of overdrive), the growth rate and the frequencies of disturbance for different unstable modes are determined in terms of eigenvalues, and the neutral stability limit is identified accordingly. After that, the approach of normal mode linear stability analysis has been extended to deal with two-dimensional perturbations [16, 17], and other forms of detonation related to different mechanisms, for instance, pathological detonation, spinning detonation, and curved detonation [18-20].

Direct numerical simulation in studying detonation stability becomes favourable only in recent decades, thanks to the development of the advanced numerical scheme and computational technology. The benefit of using numerical approach over linear stability analysis is that the nonlinearity of the problem involving time-dependent reactive Euler equations can be retained fully in the former case during the integration. Moreover, the interpretation of the numerical result in multi-dimensional stability can be investigated separately [9]. However, since the growth rate or decay rate of the pulsation is slow near the stability boundary, the simulation of these cases takes time to determine the exact limit, and the results are also sensitive to the choice of grid resolution. Examples of the relative detonation stability studies by simulations can be found in [21-25].

As the nonlinear effect becomes dominant when the detonation is away from the stability limit, the stability behavior evaluated in linear stability analysis and that in direct numerical simulation can be very different, i.e., the bifurcations point to multi unstable modes and its relative frequencies. Nevertheless, linear stability analysis remains a powerful tool in studying detonation stability for the first step, as the estimation of neutral stability limits and frequencies near the stability boundary is fairly accurate without large computation cost [19]. Comparison between both the analytical and the numerical approaches are often adopted as a strategy to validate the findings, which could be seen in many literature [26-29].

1.3 The effect of vibrational relaxation in chemistry

In the meantime, with the emerging high-power computational development, multi-dimensional numerical studies on the investigation of detonation cellular structures become one of the research interests in this area. Studies show that the cellular structure originated from the instability of the shock front is induced by unsteady coupling between dynamic flow and chemical reaction, and the size and the regularity of these structures depend on the given initial condition and the type of mixture used. Despite detailed chemical kinetics has been applied in the simulation, researchers found that there is always a persistent discrepancy in cell size and cell patterns between experimental results and numerical works [30-32]. In recent times, Taylor et al. [32] proposed that the thermodynamic equilibrium assumption may not be always valid by comparing the scale of ignition time and vibrational relaxation time in H_2/air detonation and concluded that vibrational nonequilibrium effects may be crucial in high-temperature reactive flows. According to their study on stoichiometric H_2/air detonation at 1 atm and 300 K, the ratio of the ignition delay time to the vibrational relaxation time under the post-shock state of 28 atm and 1540 K is less than 3 for H_2 and less than 2 for N_2 for a CJ detonation, assuming that the gas mixture is in thermodynamic equilibrium [33]. Apart from their report, the importance of vibrational nonequilibrium effects on supersonic combustion has also been investigated by Voelkel et al. [34] and Koo et al. [35] with detailed chemical reactions.

Right after their work, Shi et al. [36] conducted a numerical study on H_2/O_2/Ar detonation with both Park's two-temperature and coupled-vibration-chemistry-vibration (CVCV) models to investigate the effects of vibrational relaxation and coupling between molecular vibrations and chemical reactions on the detonation cell size. They revealed that the computed detonation cell size is increased when the vibrational relaxation mechanism is considered in chemical kinetics. In their studies, numerical simulations with the thermal equilibrium assumption on H_2/O_2/Ar detonation using detailed chemistry often gives an averaged cell width lower than that from the experimental measurement by a factor of 2 [32, 36]. With the application of Park's two-temperature model and CVCV model separately in the simulation, the disparity in cell width has been greatly narrowed down to a factor of 1.33 and 1.32, respectively.

From the theoretical perspective, Tarver was the first one to consider the thermodynamic nonequilibrium in the ZND model, and the extended theory was formulated as the nonequilibrium ZND (NEZND) theory in the 1980s [37-39]. In his theory, a detonation wave profile is divided into four discrete zones, including (1)

leading shock front with compressed unreacted mixture; (2) relaxation zone for rotational-vibrational modes of unreacted gases; (3) a thin zone where chemical energy is released by rapid chain propagation and branching reactions; and (4) another relaxation zone for the expansion of product gas towards thermodynamic equilibrium at the CJ state. Later, this model has been extended to study detonation related to condensed explosives [40].

1.4   Objective of the thesis

Despite plenty of numerical simulations and experimental studies considering the role of vibrational nonequilibrium effect on detonation, classical theoretical efforts remain the cornerstone of detonation physics. The step-by-step thermal equilibrium assumption in Tarver's work may not always be valid particularly in gaseous detonation, since a continuous evolution of the detonation dynamics is missing in the NEZND model. On the other hand, an appropriate description of chemical kinetics in ZND theory is important in determining the detonation structure across the profile. Conventionally, the single-step Arrhenius model is applied because of its simplicity. However, with the enhanced knowledge on the effects of vibrational relaxation in detailed chemical kinetics through numerical study, it is suggested that the coupling of chemical and vibrational effect should be further examined in detonation theory also.

The objective of the present thesis is thus to construct an extended ZND model with the vibrational-chemical coupling effect included, instead of two discrete zones describing the chemical reaction and the vibrational relaxation separately in Tarver's work. The model is examined by parametric study and the result from this analytical approach is compared with that from a numerical analysis in H_2/O_2 detonation. Moreover, the concept of vibrational-chemical coupling mechanism is applied in studying the stability of detonation propagation.

In constructing the extended ZND model, chemical models and vibrational relaxation model are taken to be the simplest forms to facilitate the theoretical model derivation. Because of the one-dimensionality of the ZND model, the half-reaction length instead of the cell sizes is considered as the characteristic length throughout the study. From the previous report, it is known that half-reaction length is directly related to detonation cell size [41]. In their work, the ratio of the detonation cell sizes to the characteristic reaction zone widths is described by a semi-empirical correlation in a function of two stability parameters, one of which is the dimensionless effective activation energy, and the other one is the empirical parameter describing the relation between chemical

energy and initial thermal energy of the explosives [41]. One-dimensional space-time conservation element and solution element (CE/SE) is introduced and is served as the primary numerical method in this research.

To address the role of the changes of 1) activation energy in chemical models, 2) time ratio of chemical reaction time scale to vibrational relaxation time scale and 3) characteristic vibrational temperature in the corresponding chemical kinetics in the extended ZND model, a parametric study is conducted and is summarized in this report. Both single-step and two-step Arrhenius models are considered. A criterion at which vibrational nonequilibrium effect becomes important is illustrated through this study.

Furthermore, the prediction of half-reaction length between analytical and numerical solution is obtained by comparing the result from the extended ZND model and that from the simulation. Due to the simplicity of the extended ZND model, compared with the computation-costly numerical simulation with detailed chemistry, the former model can serve as one of the analytical tools in large-scale H_2/O_2 detonation simulation, while the major detonation physics are retained.

Considering the detonation stability, a single-step chemistry with vibrational relaxation mechanism is first demonstrated by direct numerical simulation. Possibility of the shift of neutral stability limit in both the CJ detonation and the overdriven detonation under different time scale ratio of the chemical time scale to the vibrational time scale is demonstrated. This part of the research provides an insight into how the effect of the vibrational-chemical coupling effect can be manifested in stabilizing or destabilizing the detonation propagation.

To validate the numerical results obtained in the detonation stability problem, a normal mode linear stability analysis is constructed with one-dimensional perturbation in the final part. Stability spectrum by varying 1) activation energy in the chemical model, 2) degree of overdrive and 3) characteristic vibrational temperature is obtained at different time ratios of chemical reaction time scale to vibrational relaxation time scale. The neutral stability limit and period of oscillation computed in both approaches are compared to see if the results match. Justification of the detonation stability analysis is provided.

Chapter 2 Mathematical formulation in both analytical and numerical models

From statistical thermodynamic, there are a total of four energy modes in molecules: translational, rotational, vibrational, and electronic mode. Under the assumption of the thermal equilibrium state, all the energy modes are characterized by a single temperature only. Nevertheless, for a typical condition in gaseous detonation (i.e. H_2/O_2 detonation), the temperature range behind the shock wave can reach thousands of Kelvin. Translational equilibrium is quickly established right after the shock compression in this temperature range, while rotational mode required 10 to 20 molecular collisions to reach the equilibrium [32]. However, vibrational equilibrium requires thousands of collisions and thus it is notably important in this report. Under this nonequilibrium state, different energy modes can be characterized by different state temperatures, named translational, rotational, and vibrational temperature, respectively, while the contribution of electronic mode can be ignored in practical application for diatomic gas [42]. In this chapter, both the conventional ZND model and the extended ZND model considering vibrational relaxation mechanism are described in detail and they are considered as the analytical models. For the numerical model, the CE/SE method is presented together with the corresponding reactive Euler equations. Validation of the code with a case of piston detonation is provided.

2.1 Classic ZND theory

The classic ZND model describes the transition zone between the upstream (reactant) and downstream (product) states by a chemical reaction process. Reactants are first heated and compressed adiabatically by a leading shock. Active radical species are then produced in the induction zone right after the shock. When a sufficient amount of radical species is generated, rapid chain-branching reactions take place, and consequently, products are formed at the end of the reaction. During this process, chemical energy is released in a form of heat, which brings an increase in temperature and leads to a drop in pressure and density in the reaction zone. In this model, thermal equilibrium related to the four energy modes is often assumed. While ignoring viscous effects, the corresponding steady one-dimensional conservation equations are given by

$$\frac{d}{dx}(\rho u) = 0, \tag{2.1}$$

$$\frac{d}{dx}(p + \rho u^2) = 0, \tag{2.2}$$

$$\frac{d}{dx}[(\rho E + p)u] = 0, \tag{2.3}$$

$$\frac{d}{dx}(\rho u \lambda) = \rho \omega_\lambda \tag{2.4}$$

For an ideal gas, E can be expressed as follows,

$$E = e + \frac{u^2}{2} = \frac{p}{\rho(\gamma - 1)} - \lambda Q + \frac{u^2}{2} \tag{2.5}$$

ω_λ in Eq. (2.4) denotes the reaction rate depending on which chemical model is chosen for the study. In this case, a temperature-dependent single-step Arrhenius model is adopted and is commonly used to describe the change of reaction progress variables λ [9, 43, 44]. The expression is:

$$\omega_\lambda = \frac{d\lambda}{dt} = k_r(1 - \lambda)\exp\left(-\frac{E_{a,r}}{T}\right) \tag{2.6}$$

λ is in the range from 0 to 1, where 0 is for the reactant state and 1 is for the product state (denoting the establishment of chemical equilibrium).

By integrating the continuity, momentum, and energy equations, i.e., Eqs. (2.1) - (2.3). The Rayleigh lines and Hugoniot curves on the pv plane can be described as follows,

$$u^2 = v^2 \frac{p - p_0}{(v_0 - v)}, \tag{2.7}$$

$$\frac{pv - p_0 v_0}{\gamma - 1} + \frac{1}{2}(p + p_0)(v - v_0) - \lambda Q = 0 \tag{2.8}$$

Note that the above equations are normalized by the unburned state (denoted as the subscript 0 and the non-dimensional formulas will be presented in Eq. (2.34)) and the corresponding state properties can be expressed as below:

$$\rho_0 = p_0 = T_0 = 1, u_0 = \sqrt{\gamma}M_0, e_0 = \frac{1}{\gamma - 1} \tag{2.9}$$

where M_0 is the Mach number of gas at the unburned state. Together with the equation of state,

$$pv = T \tag{2.10}$$

The Rayleigh line and Hugoniot curve equations, i.e., Eq. (2.7) and (2.8), become

$$\gamma M_0^2 = \frac{p-1}{1-v}, \tag{2.11}$$

$$\frac{pv-1}{\gamma-1} + \frac{1}{2}(p+1)(v-1) - \lambda Q = 0 \tag{2.12}$$

Since the ZND solutions are the intersections of the Rayleigh line and Hugoniot curves, i.e., Eq. (2.11) and (2.12), the equations are reformulated in terms of p and v and is expressed as, (subscript 0 is dropped out for convenience)

$$v = \frac{(\gamma M^2 + 1)}{M^2(\gamma + 1)}[1 \mp w\xi(\lambda)], \tag{2.13}$$

$$p = \frac{(\gamma M^2 + 1)}{(\gamma + 1)}[1 \pm \gamma w\xi(\lambda)], \tag{2.14}$$

$$\xi(\lambda) = \sqrt{1 - \frac{\lambda q}{\Omega}}, \quad \Omega = \frac{\gamma(M^2-1)^2}{2M^2(\gamma^2-1)}, \quad w = \frac{M^2-1}{\gamma M^2 + 1} \tag{2.15}$$

The derivation of the above solution strictly follows the work by Erpenbeck [11] and repeated by He et al. [43]. Temperature profile can be found by applying the equation of state, i.e., Eq. (2.10). The two roots with a negative and positive sign in Eq. (2.13) (similar to that with a positive and negative sign in Eq. (2.14)) denote the strong and weak detonation solution, respectively. In this study, a strong solution is presented. By integrating across the reaction zone for the rate ω_r, all thermodynamic variables within the zone can be readily obtained. One of the significances in the ZND model is that it can be adopted as the initial condition for a dynamic detonation simulation [43].

2.2 Extended ZND theory with vibrational relaxation and the ratio of translational-rotational energy over total internal energy in terms of heat capacity at constant volume

In this extended model, only the translational-rotational mode is assumed to be at

equilibrium right after the shock. The vibrational relaxation process is taken into account as explained in the previous section. Thus, the energy equation, i.e., Eq. (2.5) is redefined as below:

$$E = e + \frac{u^2}{2} = \frac{\chi p}{\rho(\gamma - 1)} + e_v - \lambda Q + \frac{u^2}{2}, \tag{2.16}$$

$$e_v = \frac{\vartheta}{\exp(\vartheta/T_v) - 1}, \tag{2.17}$$

$$\chi = \frac{C_{v,\text{tr}}}{C_{v,\text{tr}} + C_{v,v}\dfrac{dT_v}{dT_{\text{tr}}}} \approx \frac{C_{v,\text{tr}}}{C_{v,\text{tr}} + C_{v,v}\dfrac{T_v}{T_{\text{tr}}}}, \tag{2.18}$$

$$C_{v,\text{tr}} = \frac{\epsilon}{2}R, \tag{2.19}$$

$$C_{v,v} = \left(\frac{\partial e_v}{\partial T_v}\right)_{const.\,vol} = \frac{(\vartheta/T_v)^2\exp(\vartheta/T_v)}{[\exp(\vartheta/T_v) - 1]^2}R \tag{2.20}$$

The specific heat ratio γ is assumed to be constant during the analysis. The degree of freedom is thus evaluated by $\epsilon = 2/(\gamma - 1)$, based on its relation with γ. Notably, the internal energy in Eq. (2.16) is separated into two parts, i.e. $\chi p/\rho(\gamma - 1)$ for the translational-rotational energy and e_v for the vibrational energy. Vibrational energy is modelled with a harmonic oscillator [42]. χ is defined as the ratio of translational-rotational energy versus the total internal energy in terms of specific heats at constant volume C_v, where $C_{v,\text{tr}}$ and $C_{v,v}$ are defined accordingly from the viewpoint of statistical thermodynamics [42]. In other words, the ratio of the translational-rotational energy to the vibrational energy may vary as the detonation propagates, but the total energy content is conserved. Notably, χ is in approximated form due to the existence of dT_v/dT_{tr} in the expression, and thus it is not applicable in numerical simulation as its derivative cannot be resolved completely. ϑ is the characteristic vibrational temperatures normalized with respect to initial temperature here.

With the modification in the energy equation, the extended Rankine-Hugoniot relation can be reconstructed. It is defined as the jump condition between the initial energy state at the low temperature range (the vibrational state is not excited) and the vibrationally excited energy state. The Rayleigh line would be the same as Eq. (2.11) as it is the combination of mass and momentum conversation equations only, while the Hugoniot curve is expressed in the following:

$$\frac{\chi p \upsilon - 1}{\gamma - 1} + \frac{1}{2}(p + 1)(\upsilon - 1) + e_v - \lambda Q = 0 \tag{2.21}$$

Equating Eq. (2.11) and Eq. (2.21) gives the new ZND solution in terms of p and υ as shown below:

$$\upsilon = \frac{(\gamma M^2 + 1)(1 + \varsigma/\gamma)}{M^2(\gamma + 1 + 2\varsigma)}[1 \mp w_\upsilon(\varsigma)\xi(\lambda, e_v, \varsigma)], \tag{2.22}$$

$$p = \frac{(\varsigma + 1)(\gamma M^2 + 1)}{(\gamma + 1 + 2\varsigma)}\left[1 \pm \gamma w_p(\varsigma)\xi(\lambda, e_v, \varsigma)\right] \tag{2.23}$$

where

$$\varsigma = \chi - 1, \tag{2.24}$$

$$w_\upsilon(\varsigma) = \frac{M^2 - 1}{(\gamma M^2 + 1)(1 + \varsigma/\gamma)}, w_p(\varsigma) = \frac{M^2 - 1}{(\gamma M^2 + 1)(\varsigma + 1)}, \tag{2.25}$$

$$\xi(\lambda, e_v, \varsigma) = \sqrt{1 - \frac{\lambda Q}{\Omega(\varsigma)} + \frac{e_v}{\Omega(\varsigma)} + \frac{\varsigma^2}{\Phi_1} + \frac{\varsigma}{\Phi_2}}, \tag{2.26}$$

$$\Omega(\varsigma) = \frac{\gamma(M^2 - 1)^2}{2M^2[\gamma^2 - 1 + 2\varsigma(\gamma - 1)]}, \tag{2.27}$$

$$\Phi_1 = \frac{\gamma^2(M^2 - 1)^2}{(\gamma M^2 - 1)^2}, \Phi_2 = \frac{\gamma(M^2 - 1)^2}{2(\gamma M^4 + 1)} \tag{2.28}$$

The two roots with negative and positive signs in Eq. (2.22) (positive and negative signs in Eq. (2.23), correspondingly) again indicate the strong and weak detonation solution, respectively. Strong detonation solution is taken for investigation.

To manifest the vibrational-chemical coupling effect, Park's two-temperature model is applied [45] because of its simplicity in the formulation. Temperature T in single-step Arrhenius model, i.e. Eq. (2.6) is replaced by an averaged temperature T_{avg} and is shown as

$$T_{avg} = \sqrt{T_{\text{tr}}T_{\text{v}}} \tag{2.29}$$

where T_{v} is the vibrational temperature and T_{tr} is the translational-rotational temperature denoting for the corresponding energy state distribution, respectively. To evaluate T_{v} at each point of state across the profile, the Landau-Teller model was taken to describe the energy transfer rate ω_{v} between the translational-rotational energy and the vibrational energy,

$$\omega_v = \frac{de_v}{dt} = \frac{e_v^{eq} - e_v}{\tau_v} \tag{2.30}$$

where e_v^{eq} is the vibrational energy at equilibrium state, i.e. when vibrational temperature T_v is equal to translational-rotational temperature T_{tr}. τ_v is the vibrational relaxation time and can be expressed empirically with a model formulated by Millikan and White [46]. The value of T_v can then be obtained through Newton's Iteration between each position intervals in a function of vibrational energy e_v, i.e., Eq. (2.17) and is shown below:

$$F(T_n) = \frac{\vartheta}{\exp(\vartheta/T_n) - 1} - e_v = 0, \tag{2.31}$$

$$F'(T_n) = \frac{\vartheta^2/T_n^{\,2}}{[\exp(\vartheta/T_n) - 1]^2} \exp(\vartheta/T_n), \tag{2.32}$$

$$T_{n+1} = T_n - \frac{F(T_n)}{F'(T_n)} \tag{2.33}$$

where in $F(T_n)$, i.e., Eq. (2.31), the variable T_n is the unknown to be determined. $F'(T_n)$ in Eq. (2.32) is the differentiation form of $F(T_n)$. The converged solution of T_n can then be obtained within several loops for a specified tolerance, i.e. 1.0^{-10} in this study.

The physical quantities illustrated in both the conventional ZND and extended ZND model are nondimensionalized with respect to the state of the unburned reactants as follows (the superscript $-$ denoted for dimensional variable):

$$\rho = \frac{\bar{\rho}}{\bar{\rho}_0}, p = \frac{\bar{p}}{\bar{p}_0}, T = \frac{\bar{T}}{\bar{T}_0}, \vartheta = \frac{\bar{\vartheta}}{\bar{T}_0}, u = \frac{\bar{u}}{\sqrt{R\bar{T}_0}}, \tag{2.34}$$

$$x = \frac{\bar{x}}{\bar{x}_0}, t = \frac{\bar{t}}{\bar{x}_0/\sqrt{R\bar{T}_0}}, k_r = \frac{\bar{k}_r}{\sqrt{R\bar{T}_0}/\bar{x}_0},$$

$$E = \frac{\bar{E}}{R\bar{T}_0}, E_{a,r} = \frac{\bar{E}_{a,r}}{R\bar{T}_0}, Q = \frac{\bar{Q}}{R\bar{T}_0}$$

where $\bar{x}_0$ can be replaced by $\mathcal{L}_{1/2}$. $\mathcal{L}_{1/2}$ is the half-reaction length at the thermal equilibrium case and is defined as the distance where λ increases from 0 to 0.5, i.e. half of the initial reactant is consumed.

2.2.1 Evaluating vibrational relaxation time scale by Millikan and White model

Regarding the evaluation of vibrational relaxation time scale in common gas molecules, i.e. H_2, O_2, etc., Millikan and White [46] have developed an empirical model to correlate the data set from the experiment. This model has also been widely used in other studies related to vibrational nonequilibrium effect [33, 35, 36]. The expression is as:

$$\bar{\tau}_{v,i-j} = \frac{1}{\bar{p}} \exp\left[A\left(\bar{T}^{-\frac{1}{3}} - B\right) - 18.42\right], \tag{2.35}$$

$$A = 0.00116\mu^{1/2}\bar{\vartheta}^{4/3}, B = 0.015\mu^{1/4}, \tag{2.36}$$

$$\mu = \frac{N_i N_j}{N_i + N_j} \tag{2.37}$$

μ is the reduced mass of the colliding pair and is defined when primary species i interacts with species j through molecular collisions. Besides, the model requires the input of corresponding $\bar{p}$, $\bar{T}$, and $\bar{\vartheta}$ for primary species i across the profile. For information, characteristic vibrational temperatures of different molecules are listed in Table 2.1 below.

Table 2.1 Characteristic vibrational temperature of molecules from Shi et al. [36].

Molecules	$\bar{\vartheta}$ (K)
H_2	5989
O_2	2250
OH	5140
HO_2	1577, 2059, 5325
H_2O	2297, 5266, 5409

The vibrational relaxation time of species i in a mixture of different gases, i.e., species i (self-interaction), j and k can be expressed by the following equation:

$$\frac{1}{\bar{\tau}_{v,i}} = \frac{Y_i}{\bar{\tau}_{v,i-i}} + \frac{Y_j}{\bar{\tau}_{v,i-j}} + \frac{Y_k}{\bar{\tau}_{v,i-k}} \tag{2.38}$$

where Y is the molar fraction for the corresponding species interacting with primary species i. $\bar{\tau}_{v,i-i}$, $\bar{\tau}_{v,i-j}$ and $\bar{\tau}_{v,i-k}$ are the vibrational relaxation time of species i infinitely dilute in species i (self-interaction), k, and l, respectively [33]. Corresponding $\bar{\tau}_v$ can then be obtained through the summation of all the terms.

2.2.2   Evaluating vibrational relaxation time scale by a fixed time ratio

This section shows another way of evaluating vibrational time scale by introducing a fixed time ratio $\tau^{c/v}$,

$$\tau^{c/v} \equiv \frac{\tau_c}{\tau_v} \tag{2.39}$$

where τ_c is the chemical time scale. In this report, τ_c is often regarded as the time for which half of the reactant is consumed, i.e. λ increases from 0 to 0.5, and it varies with the choice of parameters in the chemical model. Therefore, with the fixed parameter set in chemistry (and thus fixed τ_c) and the different choice of $\tau^{c/v}$, the corresponding vibrational time scale τ_v can be determined through this relation. It is expected that if $\tau^{c/v}$ increased to a certain value (i.e. $\tau_c \gg \tau_v$), the effect of vibrational relaxation can be ignored. In other words, the definition of time ratio $\tau^{c/v}$ reveals the condition under which the vibrational nonequilibrium effect is significant in gaseous detonation.

Notably, the empirical model formulated by Millikan and White [46] for the vibrational relaxation time estimation requires the input of reduced mass evaluated from the molecular masses of the tested mixture, and temperature and pressure in the corresponding time step. In other words, the vibrational relaxation time changes along the profile right after the shock based on the mixture composition, but the variation is within the same order accuracy in the hydrogen-related detonation simulation. The assumption of constant $\tau^{c/v}$ along the profile is therefore a reasonable analysis for the parametric study with the extended ZND model.

2.2.3   Special features in the extended ZND model compared with the classic ZND model

Having a close look at the square root term $\xi(\lambda, e_v, \varsigma)$ in Eq. (2.26) and comparing it with that in the conventional ZND expression, i.e. $\xi(\lambda)$ in Eq. (2.15), extra terms $e_v/\Omega(\varsigma)$, ς^2/Φ_1 and ς/Φ_2 are presented. This implies that the newly established ZND model does not only include the chemical kinetics, i.e. $\lambda Q/\Omega(\varsigma)$, but also the vibrational relaxation effect in evaluating the thermodynamic variables along the detonation profile.

At the beginning of the reaction (i.e. $\lambda = 0$) where vibrational energy state is not yet excited, i.e. $\chi = 1$ and thus $\varsigma = 0$, $\lambda Q/\Omega(\varsigma)$, ς^2/Φ_1 and ς/Φ_2 in Eq. (2.26) are zero.

e_v is a function of T_v (Eq. (2.17) and T_v is equal to T_0 at this stage. Since value of e_v is much less than unity, $\xi(\lambda, e_v, \varsigma)$ is considered to be 1. As the chemical reaction goes on, λ reaches the value of 1 at the end of reaction. Thermodynamic properties v and p in Eq. (2.22) and (2.23) (and thus T evaluated from the equation of state, i.e. Eq. (2.10)) are constant at the end of reaction since the CJ state is reached. Therefore, $\xi(\lambda, e_v, \varsigma)$ at the CJ state should be zero. In the conventional ZND profile, i.e., Eq. (2.13) and Eq. (2.14), the value of ξ is always between 0 and 1, which indicates the end and the start of chemical reaction, respectively.

In reality, γ is not a constant under vibrational nonequilibrium assumption as $C_{v,v}$ varies. Nevertheless, the use of constant γ eases the analysis in mathematical derivation such that the vibrational-chemical coupling mechanism behind the detonation physics can be manifested clearly. With this practice, $\xi(\lambda, e_v, \varsigma)$ may show a negative value near the end of reaction as the assumption of constant γ in the analysis has not been compensated yet. Therefore, the criterion for fixing $\xi(\lambda, e_v, \varsigma)$ in a range from 0 to 1 should be strictly followed based on the analysis in the classic ZND model. Figure 1 shows the typical variations of λ and ξ along the ZND profile.
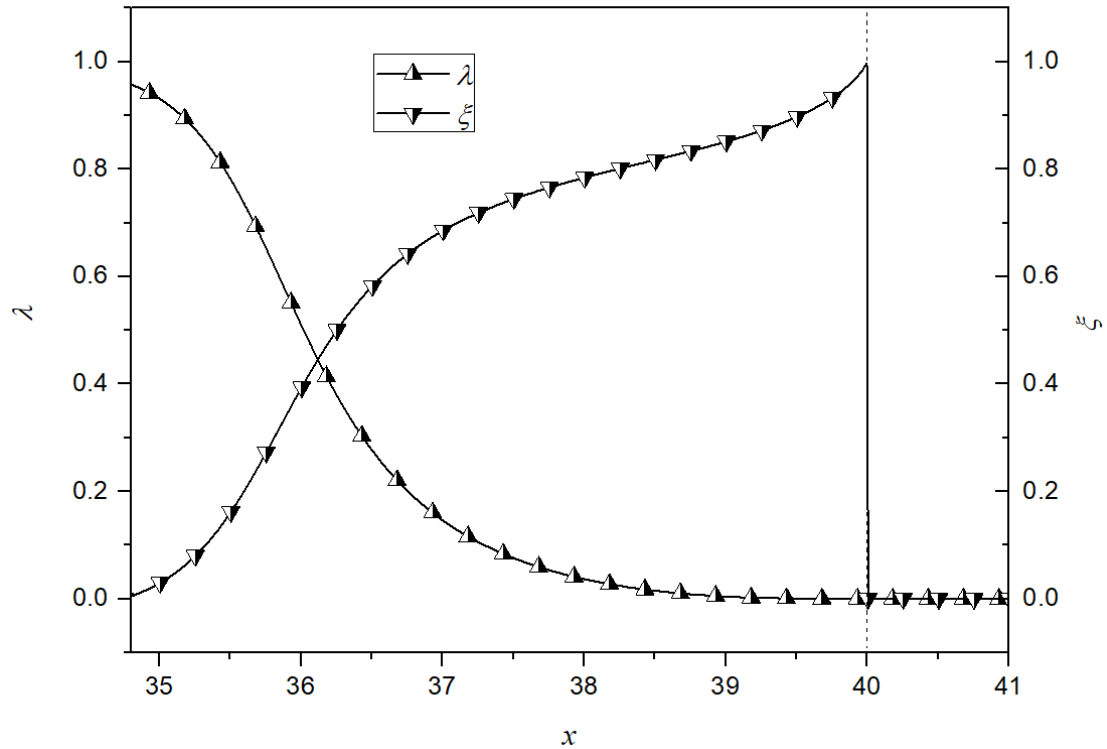
Figure 2.1 Variations of λ and ξ along the ZND profile with γ=1.2, Q=50, $E_{a,r}$=50 at $\tau^{c/v}$=0.25 and $\bar{\vartheta}$=2250 K for the nonequilibrium case (one of the test cases in section 3.1 later). The shock is encountered at normalized x = 40 and reaction starts right after

the shock. As seen, ξ approaches zero gradually when λ is advancing to 1.

On the other hand, the vibrational relaxation process continues even the chemical reaction comes to the end. Through the exchange of energy denoted by the Landau-Teller model, i.e., Eq. (2.30), T_v will eventually catch up with T_{tr} and thus value of e_v increases. Ratio χ decreased across the ZND profile accordingly. At the final state when vibrational equilibrium is reached, i.e., $T_v = T_{tr}$, χ becomes constant and therefore the criterion of $\chi < 1$ is always existed across the profile.

2.3 Extended ZND theory with vibrational relaxation but no ratio of translational-rotational energy over total internal energy in terms of heat capacity at constant volume

Per discussion in section 2.2, χ is an approximated ratio and should not be applied in analysis involving its derivatives. Therefore, another formulation is constructed in this part specified for the numerical detonation stability analysis in Chapters 5 and 6. The energy equation is modified accordingly as below:

$$E = \frac{p}{\rho(\gamma - 1)} + e_v - \lambda Q + \frac{u^2}{2} = \frac{T_{tr}}{(\gamma - 1)} + e_v(T_v) - \lambda Q + \frac{u^2}{2} \tag{2.40}$$

As seen, the total energy content would be different from that considered in section 2.1 (Eq. (2.5)) and 2.2 (Eq. (2.16)), since an extra vibrational energy term is involved in the formulation without the specific heat ratio χ to compensate the effect. However, the system presented here favour the analysis in stability theory, where the effect of change of time ratio $\tau^{c/v}$ can be manifested clearly in shock pressure history. While the conservation of mass and momentum remains unchanged, i.e., Eq. (2.1) and (2.2), the Rayleigh line would be the same as that presented in Eq. (2.11). The corresponding Hugoniot curve is expressed as:

$$\frac{pv - 1}{\gamma - 1} + \frac{1}{2}(p + 1)(v - 1) + e_v - \lambda Q = 0 \tag{2.41}$$

By equating Eq. (2.11) and Eq. (2.41), the new steady-state ZND solution is rewritten as follow (subject to the specific volume v and pressure p):

$$v = \frac{\gamma M^2 + 1}{M^2(\gamma + 1)}[1 \mp w\xi(\lambda, e_v)], \tag{2.42}$$

$$p = \frac{\gamma M^2 + 1}{\gamma + 1}[1 \pm \gamma w \xi(\lambda, e_v)], \tag{2.43}$$

$$\xi(\lambda, e_v) = \sqrt{1 + \frac{e_v - \lambda q}{\Omega}}, \Omega = \frac{\gamma(M^2 - 1)^2}{2M^2(\gamma^2 - 1)}, w = \frac{M^2 - 1}{\gamma M^2 + 1} \tag{2.44}$$

where Eqs. (2.42) - (2.44) is nondimensionalized with the pre-shock state (or the state of unburned reactant 0). The evolution of λ and e_v can be evaluated by single-step Arrhenius model together with the Landau-Teller model in an averaged two-temperature model, i.e., Eq. (2.6), (2.29) and (2.30), analogous to the treatment in section 2.2.

For an overdriven detonation, a degree of overdrive f is defined based on the ratio of the steady detonation speed D versus the Chapman-Jouguet detonation speed D_{CJ} (and thus the Mach number), which is formulated as:

$$f = \left(\frac{D}{D_{CJ}}\right)^2 \tag{2.45}$$

where D_{CJ} is the Chapman-Jouguet (CJ) detonation velocity at equilibrium state and can be evaluated in terms of γ and Q as described in [11]:

$$D_{CJ}{}^2 = 1 + b(1 + 0.25b^2)^{1/2} + 0.5b^2, \tag{2.46}$$
$$b = 2(\gamma^2 - 1)Q/\gamma$$

2.4   Conservation equations in numerical simulation

Section 2.1, 2.2, and 2.3 describes a steady detonation model in theory by considering the jump conditions between the two states. To further confirm the findings in the theoretical detonation model, numerical studies are conducted for the comparison. Therefore, mathematical formulations in numerical work are presented in this section to simulate an unsteady self-propagating detonation. The conservation laws to describe a structure of one-dimensional (1-D) detonation can be written in the form of unsteady reactive Euler equations,

$$\frac{\partial \boldsymbol{U}}{\partial t} + \frac{\partial \boldsymbol{F}}{\partial x} = \boldsymbol{S} \tag{2.47}$$

where U, F, and S are the conserved variables, corresponding fluxes, and source terms, respectively. Applying the detail chemistry model under thermal equilibrium assumption, the above variables are described as follows

$$U = [\bar{\rho}_i, \bar{\rho}\bar{u}, \bar{\rho}\bar{E}]^T ,$$ (2.48)

$$F = [\bar{\rho}_i\bar{u}, \bar{\rho}\bar{u}^2 + \bar{p}, (\bar{\rho}\bar{E} + \bar{p})\bar{u}]^T ,$$ (2.49)

$$S = [\bar{\rho}_i\bar{\omega}_i, 0, 0]^T$$ (2.50)

where $\bar{\omega}_i$ is the rate of change caused by chemical reactions. If a single-step or a two-step Arrhenius model is used instead, the variables are formulated accordingly as:

$$U = [\rho, \rho u, \rho E, \rho \lambda, \rho \beta]^T ,$$ (2.51)

$$F = [\rho u, \rho u^2 + p, (\rho E + p)u, \rho \lambda u, \rho \beta u]^T ,$$ (2.52)

$$S = [0, 0, 0, \rho \omega_\lambda, \rho \omega_\beta]^T$$ (2.53)

where β is the progress variable for the induction time zone in the two-step Arrhenius model. It is set to be 0 initially for the two-step model and is set to be unity initially for the single-step model. The source terms of the two-step model will be discussed separately in Chapters 3 and 4, while the source term of the single-step model has been presented in Eq. (2.6).

Similarly, in vibrational nonequilibrium flows, an additional equation to describe the vibrational energy for all the species is involved. This energy mode is characterized by a single vibrational temperature $\bar{T}_v$ in the detailed chemistry model. The vectors are reorganized as,

$$U = [\bar{\rho}_i, \bar{\rho}\bar{u}, \bar{\rho}\bar{E}, \bar{\rho}\bar{e}_v]^T ,$$ (2.54)

$$F = [\bar{\rho}_i\bar{u}, \bar{\rho}\bar{u}^2 + \bar{p}, (\bar{\rho}\bar{E} + \bar{p})\bar{u}, \bar{\rho}\bar{e}_v\bar{u}]^T ,$$ (2.55)

$$S = [\bar{\rho}_i\bar{\omega}_i, 0, 0, \bar{\rho}\bar{\omega}_v]^T$$ (2.56)

If a single-step or two-step Arrhenius model is selected instead, the variables are reformulated as below

$$U = [\rho, \rho u, \rho E, \rho e_v, \rho \lambda, \rho \beta]^T ,$$ (2.57)

$$F = [\rho u, \rho u^2 + p, (\rho E + p)u, \rho e_v u, \rho \lambda u, \rho \beta u]^T ,$$ (2.58)

$$S = [0, 0, 0, \rho \omega_v, \rho \omega_\lambda, \rho \omega_\beta]^T$$ (2.59)

where ω_v (or $\bar{\omega}_v$) is the source terms of vibrational relaxation mechanism (Landau-

Teller model) and is presented in Eq. (2.30) before. Both the thermal (or vibrational) equilibrium (eq) case in Eqs. (2.51) - (2.53) and the thermal nonequilibrium (Neq) case (i.e. Eqs. (2.57) - (2.59)) are examined in this report. By applying Park's two-temperature model (shown in Eq. (2.29)) in the Neq case, the vibrational-chemical coupling effect is included for investigation. In Shi et al.'s work [47], the coupled vibration-chemistry-vibration (CVCVs) model [48] is also investigated in the simulation with hydrogen-related detonation. Nevertheless, this model is relatively complex compared with Park's model and is not appropriate in a theoretical demonstration. Noted that the equations related to the detailed chemical kinetics, i.e., Eqs. (2.48) - (2.50) and Eqs. (2.54) - (2.56), are calculated in the dimensional form (denoted as the superscript $-$) at first, and then the result is normalized for comparison with the one from simplified chemistry, i.e., Eqs. (2.51) - (2.53) and Eqs. (2.57) - (2.59), which is in non-dimensional form. For convenience, the superscript $-$ is dropped in sections 2.4.1 and 2.4.2.

2.4.1 Evaluation of thermodynamic properties

For Euler equations involving detailed chemical kinetics (referring from Shi [47]), i.e. Eqs. (2.48) - (2.50) and Eqs. (2.54) - (2.56), the pressure of the gas mixture is calculated from individual partial pressure and is expressed below:

$$p = \sum_{i=1}^{Ns} \frac{\rho_i R T_{tr}}{MW_i} \tag{2.60}$$

where MW_i is the molecular weight of the ith species.

The corresponding total energy per unit volume of mixture is shown below

$$E = \sum_{i=1}^{Ns} \rho_i h_i^f + \sum_{i=1}^{Ns} \rho_i C_{v,tr,i} T_{tr} + \frac{1}{2}\rho u^2 + \sum_{molecule} \rho_i e_{v,i}, \tag{2.61}$$

$$e_{v,i} = \frac{\vartheta_i}{\exp(\vartheta_i/T_v) - 1} \frac{R}{MW_i} \tag{2.62}$$

where h_i^f is the species enthalpy of formation obtained from NASA Glenn coefficients [49]. Noted that T_{tr} and T_v are equalized in the case of vibrational equilibrium. To determine the specific heat at constant volume for translational-rotational mode, it can

be given as

$$C_{v,\text{tr},i} = C_{v,\text{t},i} + C_{v,\text{r},i} = \frac{\epsilon}{2} \frac{R}{MW_i} \tag{2.63}$$

In this report, both the translational mode and the rotational mode for the specific heats at constant volume are assumed to be constant. The expression for $C_{v,\text{tr},i}$ is analogous to Eq. (2.19) while corresponding species are considered here. Degree of freedom ϵ depends on which type of molecules or atoms are being investigated and is listed below

$$C_{v,\text{t},i} = \frac{3}{2} \frac{R}{MW_i}, \tag{2.64}$$

$$C_{v,\text{r},i} = \begin{cases} 0 & \text{atoms} \\ \dfrac{R}{MW_i} & \text{diatomics} \\ \dfrac{3}{2} \dfrac{R}{MW_i} & \text{polyatomics} \end{cases} \tag{2.65}$$

For the specific heat at constant volume in vibrational mode, the value varies with the derivative of vibrational energy at the corresponding state across the profile and is calculated as follows,

$$C_{v,\text{v},i} = \frac{(\vartheta_i/T_\text{v})^2 \exp(\vartheta_i/T_\text{v})}{[\exp(\vartheta_i/T_\text{v}) - 1]^2} \frac{R}{MW_i} \tag{2.66}$$

Noted that the expression is again analogous to Eq. (2.20) while corresponding species are specified here. To obtain T_v from the vibrational energy terms for all species, Newton's Iteration is applied similarly to the case in Eqs. (2.31) - (2.33).

For the formulation involving a single-step or two-step Arrhenius model, i.e., Eqs. (2.51) - (2.53) and Eqs. (2.57) - (2.59), the expressions are comparatively simpler as it assumed that the reaction only consists of a single reactant and a single product. The total energy equation in the normalized form is analogous to Eq. (2.40). Other thermodynamic properties can then be evaluated through the equation of state, i.e. Eq. (2.10). In vibrational equilibrium case involving the consideration of $T_\text{v} = T_\text{tr}$ across the profile, T_tr cannot be explicitly determined through Eq. (2.42) and (2.43). A corresponding function of temperature is therefore established for Newton's Iteration and is given below:

$$G(T_n) = \left[\frac{T_n}{(\gamma - 1)} + e_v(T_n)\right] - \left(E + \lambda Q - \frac{u^2}{2}\right) = 0 , \tag{2.67}$$

$$G'(T_n) = \frac{1}{(\gamma - 1)} + \frac{\vartheta^2/T_n^2}{[\exp(\vartheta/T_n) - 1]^2} \exp(\vartheta/T_n) , \tag{2.68}$$

$$T_{n+1} = T_n - \frac{G(T_n)}{G'(T_n)} \tag{2.69}$$

In the case of vibrational nonequilibrium, the formulation to obtain T_v through Newton's Iteration would be the same as Eqs. (2.31) - (2.33).

2.4.2   Source terms for the detailed chemical kinetics

Considering the ZND theory or the extended ZND theory, the reaction is assumed to be completed in a single-step or two-step for simplicity. However, in reality, many intermediate reactions and species are produced before reaching the final state. To mimic the reaction mechanism and avoid the loss of information in simulation, detailed chemical kinetics with formulas [50, 51] is introduced in this section.

The elementary reaction for a detailed reaction model in dimensional form can be expressed in the following form:

$$\sum_{i=1}^{Ns} v'_{k,i} Y_i \leftrightarrow \sum_{i=1}^{Ns} v''_{k,i} Y_i \tag{2.70}$$

where $v'_{k,i}$ and $v''_{k,i}$ are the stoichiometric coefficients with integral numbers of each species in forward and backward reactions, respectively. For an Ns elementary reaction, the mass formation rate of the ith species (the source terms in Eq. (2.50) and Eq. (2.56)) is

$$\omega_i = MW_i \sum_{i=1}^{Ns} (v''_{k,i} - v'_{k,i}) q_k \tag{2.71}$$

The rate of progress variable q_i for which a third body is required in the reaction is expressed as:

$$q_k = B_k \left(k_{f,k} \prod_{i=1}^{Ns} [C_i]^{v'_{k,i}} - k_{b,k} \prod_{i=1}^{Ns} [C_i]^{v''_{k,i}} \right), \tag{2.72}$$

$$B_k = \begin{cases} 1 & \text{without third body effect} \\ \prod_{i=1}^{Ns} \delta_{k,i} C_i & \text{with third body effect} \end{cases} \tag{2.73}$$

where $k_{f,k}$ and $k_{b,k}$ are the reaction rate constants for forward and backward reactions, respectively. $C_i = \rho_i / MW_i$ is the molar density of the ith species and B_k is the factor contributed to the reactions involving a third body. B_k depends on the third-body coefficient $\delta_{k,i}$ if third body effect is presented in the kth reaction for species i.

As described by temperature-dependent Arrhenius law, the forward reaction rate constant $k_{f,k}$ is given as:

$$k_{f,k} = A_k T^{m_k} \exp \left(-\frac{E_{a,k}}{RT} \right) \tag{2.74}$$

where A_k is the pre-exponential factor, m_k is the temperature exponent, and $E_{a,k}$ is the activation energy for the kth reaction.

The backward rate constant $k_{b,k}$ and the forward reaction constant $k_{f,k}$ is related by the equilibrium constant $k_{c,k}$ as shown below:

$$k_{c,k} = \frac{k_{f,k}}{k_{b,k}}, \tag{2.75}$$

$$k_{c,k} = \exp \left[\sum_{i=1}^{Ns} (v''_{k,i} - v'_{k,i}) \left(\frac{s_i^0}{R_i} - \frac{h_i}{R_i T} \right) \right] \left(\frac{p_a}{RT} \right)^{\sum_{i=1}^{Nr} (v''_{k,i} - v'_{k,i})} \tag{2.76}$$

where p_a is the standard atmospheric pressure, R_i is the gas constant for species i, s_i^0 is the standard state specific entropy and h_i is the specific enthalpy. s_i^0 and h_i can be evaluated as follows:

$$\frac{h_i}{R_i T} = -\frac{a_{1i}}{T^2} + a_{2i} \frac{lnT}{T} + a_{3i} + a_{4i} \frac{T}{2} + a_{5i} \frac{T^2}{3} + a_{6i} \frac{T^3}{4} + a_{7i} \frac{T^4}{5} + \frac{b_{1i}}{T}, \tag{2.77}$$

$$\frac{s_i^0}{R_i} = -\frac{a_{1i}}{2T^2} - \frac{a_{2i}}{T} + a_{3i}\ln T + a_{4i}T + a_{5i}\frac{T^2}{2} + a_{6i}\frac{T^3}{3} + a_{7i}\frac{T^4}{4} + b_{2i} \tag{2.78}$$

a_i and b_i are the constants referring to the NASA Glenn coefficients [49].

To evaluate the rate of unimolecular reactions following Lindemann's approach, it requires the input of temperature-dependent Arrhenius equations, i.e., Eq. (2.74), for the high-pressure limit k_∞ and the low-pressure limit k_0. The rate constant of any pressure can be calculated as shown below:

$$k = k_\infty \left(\frac{P_r}{1 + P_r}\right) F \tag{2.79}$$

where the reduced pressure is given by

$$P_r = \frac{k_0}{k_\infty}[C] \tag{2.80}$$

$[C]$ is the molar density of the mixture. The factor F can be expressed in Troe's form with central factor F_c:

$$\log F = \left[1 + \left[\frac{\log P_r + c}{n - d(\log P_r + c)}\right]^2\right]^{-1} \log F_c, \tag{2.81}$$

$$c = -0.4 - 0.6 \log F_c, \tag{2.82}$$
$$n = -0.75 - 1.27 \log F_c, \tag{2.83}$$
$$d = 0.14 \tag{2.84}$$

In the case of vibrational nonequilibrium, the source terms related to vibrational relaxation mechanism are manifested by the Landau-Teller model, i.e., Eq. (2.30), together with the evaluation of τ_v from Millikan and White Method discussed in section 2.2.1. Park's two-temperature model, i.e., Eq. (2.29), is applied to characterize the effect of vibrational relaxation on reaction rate with averaged temperature T_{avg} and the forward Arrhenius equations of reaction rate (Eq. (2.74)) is reconstructed as follows:

$$k_{f,k} = A_k T_{avg}^{m_k} \exp\left(-\frac{E_{a,k}}{RT_{avg}}\right) \tag{2.85}$$

2.5   Description of the numerical CE/SE method

The conservation element and solution element (CE/SE) method, originally proposed by Chang et al. in the 1990s [52], unifies the treatment of both space and time by introducing two concepts: conservation element and solution element. This scheme is capable of capturing the shock structure without using Riemann solvers and is successfully implemented in the computation of hypersonic reentry flows [53, 54], detonation waves [36, 55], and compressible multiphase problems [56-58]. In this section, a one-dimensional local space-time CE/SE scheme on uniform meshes is introduced referring to Shi's work [47].

For a hyperbolic equation in one-dimensional (1-D)

$$\frac{\partial u}{\partial t} + \frac{\partial f}{\partial x} = 0 \tag{2.86}$$

where t and x can be considered as the coordinates of a two-dimensional Euclidean space. By Gauss' divergence theorem, Eq. (2.86) can be expressed in the differential form of integral conservation law as shown:

$$\iint_V \left(\frac{\partial u}{\partial t} + \frac{\partial f}{\partial x} \right) dV = \oint_{S(V)} \mathbf{h} \cdot d\mathbf{s} = 0 \tag{2.87}$$

where $\mathbf{h} = (f, u)$ is the vector consists of flux and conserved variable, $d\mathbf{s} = d\sigma \cdot \mathbf{n}$ in which $d\sigma$ is the infinitesimal length and $\mathbf{n}$ is the unit outward normal vector of a boundary segment on $S(V)$.

To integrate Eq. (2.87), a close space named the conservation element (CE) is set up as illustrated in Figure 2.2.
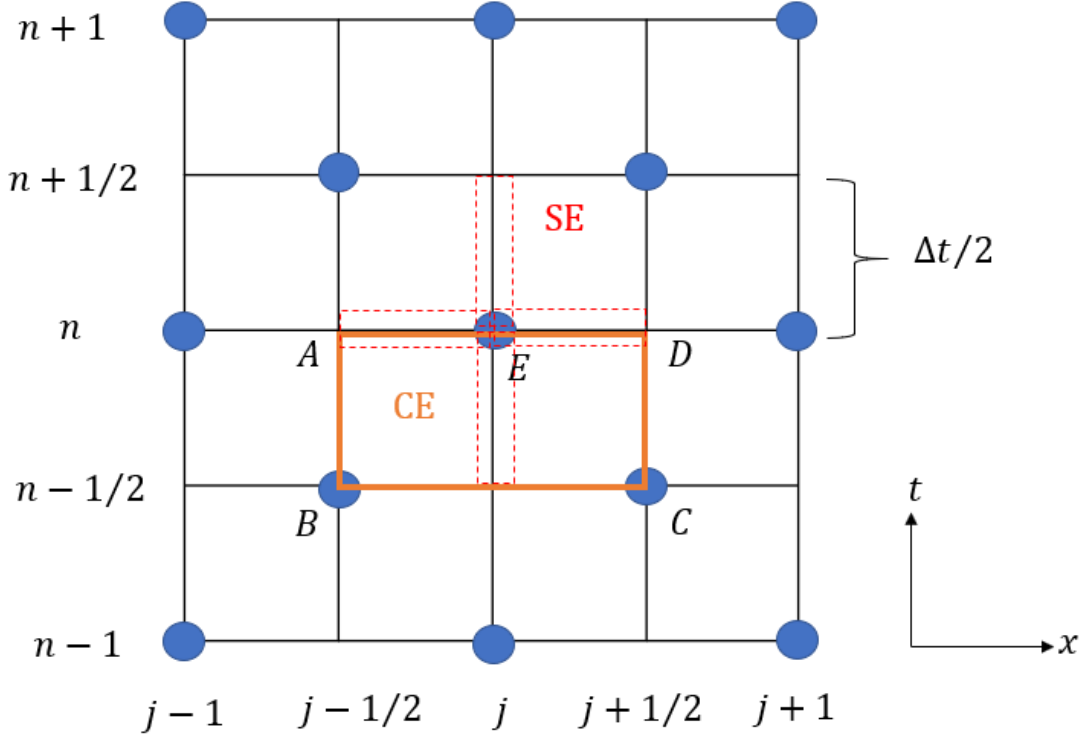
Figure 2.2 Configuration of conservation element (CE) and solution element (SE) for the one-dimensional CE/SE scheme.

Rectangle $ABCD$ is the corresponding CE at node E. To solve the value of node E based on the known values of nodes B and C, integration on each edge of CE is included, and Eq. (2.87) can be written as:

$$\oint_{ABCD} \mathbf{h} \cdot d\mathbf{s} = -\int_{AB} f(x,t)dt - \int_{BC} u(x,t)dx + \int_{DC} f(x,t)dt \tag{2.88}$$

$$+ \int_{AD} u(x,t)dx = 0$$

where the unit normal vectors pointing outward are (-1, 0) for AB, (0, -1) for BC, (1, 0) for DC and (0, 1) for AD.

The solution element (SE) is defined as the cross line of each node (For instance, SE of node E is shown in Figure 2.2). By using first-order Taylor expansion, the value of u and f can be approximated as follows at each SE,

$$u(x,t) = u_j^n + (u_x)_j^n(x - x_j) + (u_t)_j^n(t - t^n), \tag{2.89}$$
$$f(x,t) = f_j^n + (f_x)_j^n(x - x_j) + (f_t)_j^n(t - t^n) \tag{2.90}$$

To calculate the derivatives of flux f, the chain rule is applied as below

$$\frac{\partial f}{\partial x} = \left(\frac{\partial f}{\partial u}\right)\left(\frac{\partial u}{\partial x}\right) \tag{2.91}$$

The time derivative of u can be evaluated from Eq. (2.86),

$$\left(\frac{\partial u}{\partial t}\right)_j^n = -\left(\frac{\partial f}{\partial x}\right)_j^n \tag{2.92}$$

Notably, to calculate the derivative of u and f, the essential variables needed to be solved in each time step is u and u_x. Hence, Eq. (2.88) can be reconstructed with Taylor expansion as below:

$$\begin{aligned}
\oint_{ABCD} \mathbf{h} \cdot d\mathbf{s} = &-\int_0^{\frac{\Delta t}{2}} \left[(f)_{j-\frac{1}{2}}^{n-\frac{1}{2}} + (f_t)_{j-\frac{1}{2}}^{n-\frac{1}{2}} t\right] dt \\
&- \int_0^{\frac{\Delta x}{2}} \left[(u)_{j-\frac{1}{2}}^{n-\frac{1}{2}} + (u_x)_{j-\frac{1}{2}}^{n-\frac{1}{2}} x\right] dx \\
&- \int_{-\frac{\Delta x}{2}}^{0} \left[(u)_{j+\frac{1}{2}}^{n-\frac{1}{2}} + (u_x)_{j+\frac{1}{2}}^{n-\frac{1}{2}} x\right] dx \\
&+ \int_0^{\frac{\Delta t}{2}} \left[(f)_{j+\frac{1}{2}}^{n-\frac{1}{2}} + (f_t)_{j+\frac{1}{2}}^{n-\frac{1}{2}} t\right] dt + \int_{-\frac{\Delta x}{2}}^{\frac{\Delta x}{2}} [(u)_j^n + (u_x)_j^n x] dx \\
&= 0
\end{aligned} \tag{2.93}$$

Simplify Eq. (2.93) to evaluate u_j^n gives the explicit form below:

$$\begin{aligned}
u_j^n = &\frac{\Delta t}{2\Delta x}\left[(f)_{j-\frac{1}{2}}^{n-\frac{1}{2}} + (f_t)_{j-\frac{1}{2}}^{n-\frac{1}{2}}\frac{\Delta t}{4}\right] + \frac{1}{2}\left[(u)_{j-\frac{1}{2}}^{n-\frac{1}{2}} + (u_x)_{j-\frac{1}{2}}^{n-\frac{1}{2}}\frac{\Delta x}{4}\right] \\
&+ \frac{1}{2}\left[(u)_{j+\frac{1}{2}}^{n-\frac{1}{2}} - (u_x)_{j+\frac{1}{2}}^{n-\frac{1}{2}}\frac{\Delta x}{4}\right] - \frac{\Delta t}{2\Delta x}\left[(f)_{j+\frac{1}{2}}^{n-\frac{1}{2}} + (f_t)_{j+\frac{1}{2}}^{n-\frac{1}{2}}\frac{\Delta t}{4}\right]
\end{aligned} \tag{2.94}$$

The value of node A (and node D) can be approximated through Taylor expansion from SE of node B and E (and from SE of node C and E, respectively) as shown:

$$(u)^n_{j-\frac{1}{2}} = (u)^{n-\frac{1}{2}}_{j-\frac{1}{2}} + (u_t)^{n-\frac{1}{2}}_{j-\frac{1}{2}} \frac{\Delta t}{2} = (u)^n_j - (u_x)^n_j \frac{\Delta x}{2}, \tag{2.95}$$

$$(u)^n_{j+\frac{1}{2}} = (u)^{n-\frac{1}{2}}_{j+\frac{1}{2}} + (u_t)^{n-\frac{1}{2}}_{j+\frac{1}{2}} \frac{\Delta t}{2} = (u)^n_j + (u_x)^n_j \frac{\Delta x}{2} \tag{2.96}$$

The spatial derivative $(u_x)^n_j$ can then be calculated from both sides

$$(u_x^-)^n_j = -\frac{(u)^{n-\frac{1}{2}}_{j-\frac{1}{2}} + (u_t)^{n-\frac{1}{2}}_{j-\frac{1}{2}} \frac{\Delta t}{2} - (u)^n_j}{\Delta x/2}, \tag{2.97}$$

$$(u_x^+)^n_j = \frac{(u)^{n-\frac{1}{2}}_{j+\frac{1}{2}} + (u_t)^{n-\frac{1}{2}}_{j+\frac{1}{2}} \frac{\Delta t}{2} - (u)^n_j}{\Delta x/2} \tag{2.98}$$

With a weighted function, $(u_x)^n_j$ can be averaged as follows:

$$(u_x)^n_j = \frac{\left|(u_x^+)^n_j\right|^a (u_x^-)^n_j + \left|(u_x^-)^n_j\right|^a (u_x^+)^n_j}{\left|(u_x^+)^n_j\right|^a + \left|(u_x^-)^n_j\right|^a} \tag{2.99}$$

where a is set between 1 and 2 such that the numerical instability near the discontinuity can be avoided.

2.6   Verification of numerical code

For validation of the numerical scheme, a case of piston-supported detonation is simulated one-dimensionally at $Q=50$, $E_a=50$, $\gamma=1.2$, and $f=1.6$. Figure 2.3 shows the computed shock pressure history at a grid resolution of 10 points per half-reaction length ($10/\mathcal{L}_{1/2}$), $20/\mathcal{L}_{1/2}$, $40/\mathcal{L}_{1/2}$ and $80/\mathcal{L}_{1/2}$, respectively. The corresponding averaged period of oscillation is 7.60, 7.43, 7.37, and 7.34, in which the percentage error of difference is at most 0.01% compared with the same cases presented in Shen & Parsani's work [44]. The code with the CE/SE scheme should be well validated.
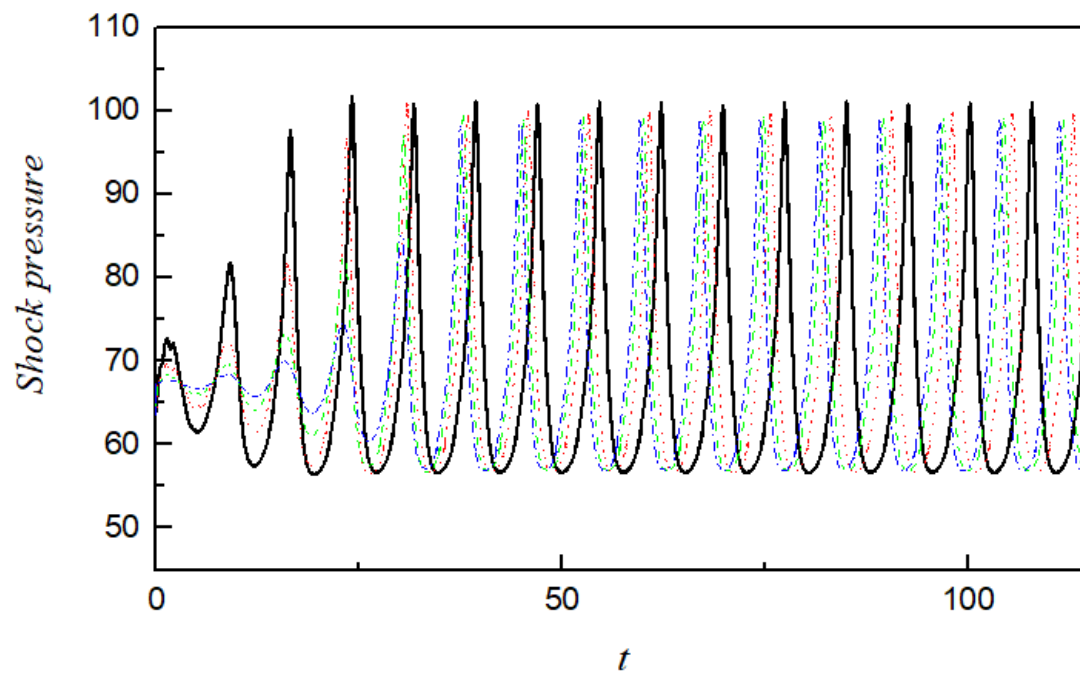
Figure 2.3 Shock pressure history for 1D piston-supported detonation at $Q=50$, $E_a=50$, $\gamma=1.2$ and $f=1.6$ with resolution $10/\mathcal{L}_{1/2}$ (black solid), $20/\mathcal{L}_{1/2}$ (red dotted), $40/\mathcal{L}_{1/2}$ (green dashed) and $80/\mathcal{L}_{1/2}$ (blue dot-dash) respectively.

Chapter 3 Parametric study on the extended detonation model at vibrational nonequilibrium

In Chapter 2, the extended ZND theory with χ is established in section 2.2 based on the vibrational-chemical coupling mechanism proposed. In this one-dimensional simplified model, half-reaction length is crucial in manifesting the coupling effect as it is closely related to the detonation cell size in simulation. From the previous studies, it is revealed that the detonation cell size is enlarged in the case of vibrational nonequilibrium. Thus, the elongation of half reaction length is expected also under the same assumption. To further clarify the critical condition for which the vibrational relaxation effect is significant, different key parameters in the model are being studied systematically in both the thermal equilibrium and nonequilibrium cases.

The parametric studies presented in this chapter are divided into four parts. Single-step Arrhenius model, i.e., Eq. (2.6), is considered for the first three part, with different values of the non-dimensional parameters – activation energy $E_{a,r}$, time ratio $\tau^{c/v}$ and characteristic vibrational temperature ϑ being tested. Since γ and Q only change the thermodynamic properties at the initial (reactant) state and end (product) state but not the detonation structure within the reaction zone (i.e. the gradient across the profile and thus the half-reaction length), these values were kept constant throughout the analysis. In this study, γ is set as 1.2 and Q is set as 50. The critical $\tau^{c/v}$ at which the vibrational relaxation should be considered is discussed.

However, the chain-initiation stage cannot be represented effectively in a single-step Arrhenius model if it is comparatively important in a chemical reaction [59]. Therefore, in the last part, a two-step Arrhenius chemical model is investigated with a combination of both an induction zone model and a chemical reaction model. The temperature-dependent induction time model without a step function is shown below:

$$\omega_\beta = \frac{d\beta}{dt} = k_{ind}\beta\exp\left[E_{a,ind}\left(\frac{1}{T_{vn}} - \frac{1}{T}\right)\right] \tag{3.1}$$

where T_{vn} is the von-Neumann temperature at shock front and can be evaluated from the equilibrium Rankine-Hugoniot relation, i.e., Eqs. (2.13) - (2.15), with the given γ and Q. k_{ind} is the preexponential factor and $E_{a,ind}$ is the corresponding activation energy for induction time model, respectively. β is the progress variable for induction

29

process and it equals to 0 at the start of the induction zone right behind the shock. As time goes on (by integrating across the profile), β increases to the value of 1 at the end of the zone. Once the limit of $\beta = 1$ is reached, exothermic reaction starts automatically in the next stage, which is governed by Arrhenius equations for chemical reaction, i.e., Eq. (2.6). The induction zone length $\mathcal{L}_{ind}$ is thus defined in the region where $0 \leq \beta \leq 1$. Other parameters are summarized in Table 3.1.

Table 3.1 Parameters used in the extended ZND profile simulations.

Parameter commonly used in both conventional and extended ZND model	
γ	1.2
Q	50
k_i	17
k_r	2400
Parameter used in modified ZND model only (vibrational nonequilibrium case)	
$\bar{T}_0$	300 K
R_{o_2}	259.8 J/kg K

Noted that initial temperature $\bar{T}_0$ and gas constant for oxygen R_{o_2} were chosen to normalize e_v following the simulation of $H_2/O_2/Ar$ detonation by Shi et al. [36].

The critical $\tau^{c/v}$ again is discussed in this part while keeping the ratio of $\mathcal{L}_{1/2}$ and $\mathcal{L}_{ind}$ to be 2:1 under the thermal equilibrium state. Through these studies, a physical picture of how the vibrational nonequilibrium effect can play a role in temperature-dependent reaction models in gaseous detonation is illustrated.

Note that the length of the domain of interest is 1000 $\mathcal{L}_{1/2}$. Over 200 mesh points were used per half-reaction length in the integration of the ZND profile in each case. All the properties are normalized with respect to initial reactant state (0 state). For reference, the content discussed in this chapter has been published in [60].

3.1   Dependence on activation energy using single-step Arrhenius model

In this section, activation energy $E_{a,r}$ ranged from 10 to 50 were selected to be examined with an increase in 10 increments at each trial. The time ratio $\tau^{c/v}$=0.25 was selected to have a value less than unity such that the vibrational relaxation time scale is significantly longer than the chemical reaction time scale across the profile (in other words, the case is at vibrational nonequilibrium state). Notably, in a typical $H_2/O_2/Ar$

detonation, oxygen is one of the major reactants in the simulations. Therefore, to evaluate the vibrational energy term e_v, $\bar{\vartheta}$=2250 K for oxygen molecules was selected.

Figure 3.1 shows the profiles of temperature T and mass fraction of reactant Z for cases with $E_{a,r}$=10 and $E_{a,r}$=50. Comparing the two cases, the nonequilibrium case of $E_{a,r}$=50 has a much longer half reaction length, with a slower reaction rate (flatten slope in the Z curve) initially. The half-reaction length in the nonequilibrium case of $E_{a,r}$=50 is 4 times larger that of the half-reaction length in the equilibrium case, whereas the elongation of half reaction length is double compared with the equilibrium case at $E_{a,r}$=10. Although the chemical model applied is in single-step Arrhenius form without any induction time model, i.e., Eq. (2.6), it provides a clue that the overall reaction rate in the vibrational nonequilibrium case is always slower compared with that in the equilibrium case. One of the possible reasons is that the excitation of vibrational mode in molecules reduces the effective reaction temperature for the chemical reaction. At the start of the reaction right after the shock (i.e. $x<40$), there is a large deviation between translational-rotational temperature T_{tr} and vibrational temperature T_v. Translation-rotational mode reached the equilibrium shock state shortly while vibrational mode does not. As the vibrational relaxation process goes on, T_v will eventually approach to T_{tr} in the end. This can be manifested by the Park's two-temperature model, i.e., Eq. (2.29), in the Arrhenius equation, where T_{avg} has a close value to T_{tr} in the end of reaction. The features of the profiles presented here match with that of the one-dimensional numerical simulation by Shi et al. [36].
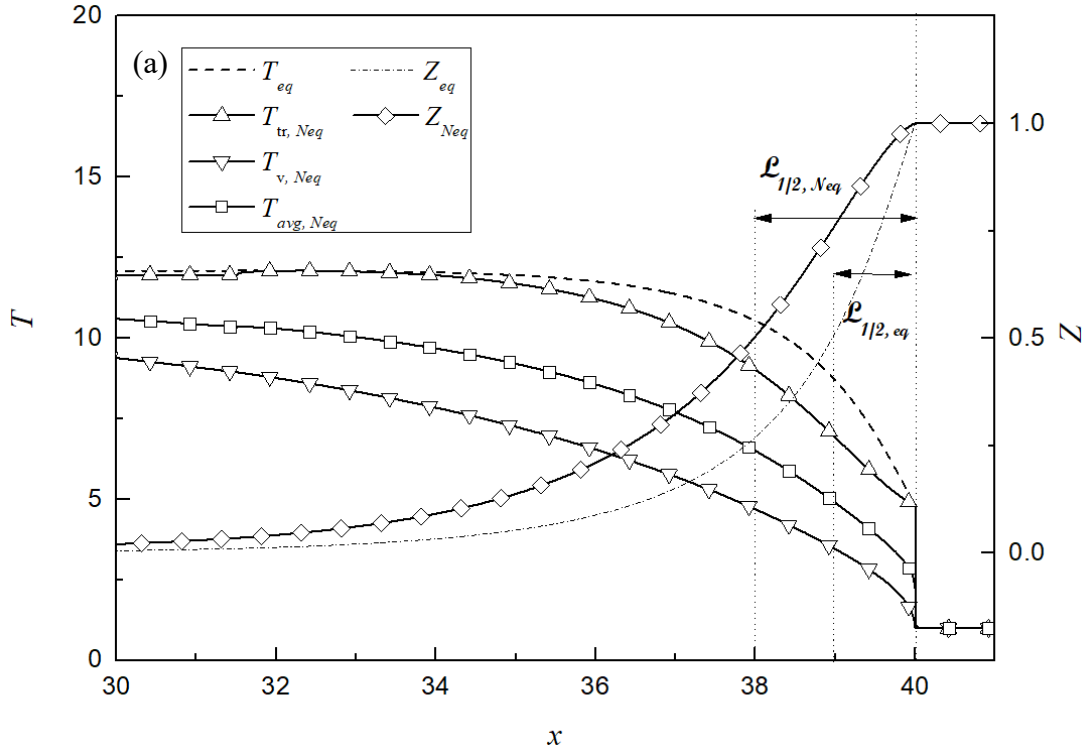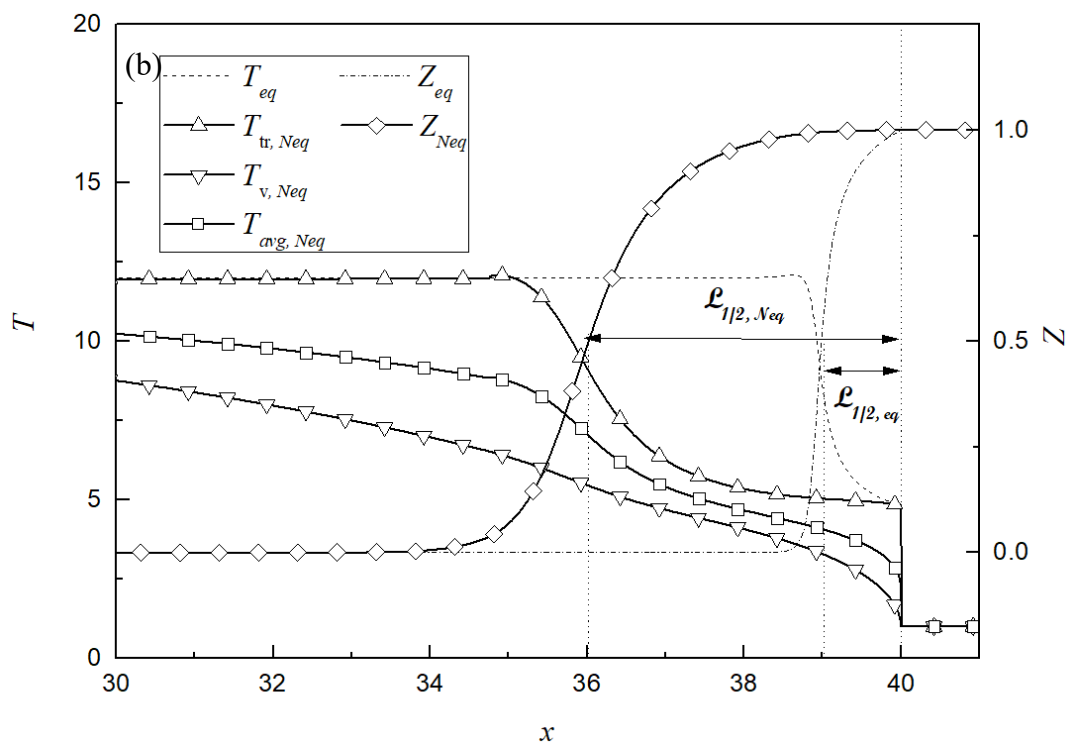
Figure 3.1 Temperature T and mass fraction of reactant Z profiles at the vibrational equilibrium state (*eq*) and the vibrational non-equilibrium state (*Neq*) using single-step Arrhenius model with (a) $E_{a,r}$=10 and (b) $E_{a,r}$=50 at $\tau^{c/v}$=0.25 and $\bar{\vartheta}$=2250 K.

Figure 3.2 Ratio of $\mathcal{L}_{1/2}$ for the nonequilibrium case to that of the equilibrium case versus $E_{a,r}$ at $\tau^{c/v}$=0.25 and $\bar{\vartheta}$=2250 K.

The ratio of half reaction length under the vibrational nonequilibrium (*Neq*) assumption to that under the vibrational equilibrium (*eq*) assumption (i.e., take the equilibrium $\mathcal{L}_{1/2}$ equals to unity as reference) versus the selected $E_{a,r}$ values are presented in Figure 3.2. As shown in the figure, the half-reaction length under the vibrational nonequilibrium assumption is at least double (at $E_{a,r}=10$) compared with that under the vibrational equilibrium assumption. The ratio can be up to four times that of the equilibrium $\mathcal{L}_{1/2}$ if high activation energy is implemented in the chemical model formulation, i.e., at $E_{a,r}=50$. Note that the degree of increase in $\mathcal{L}_{1/2}$ ratio depends on the choice of the initial state properties, such as γ and Q, but the trend of having longer half-reaction length with higher activation energy input under the thermal nonequilibrium assumption stands. This implies that the vibrational relaxation becomes significant if the chemical reaction mechanism with high activation energy is involved in the gas detonation problem.

3.2 Dependence on time ratio of chemical reaction time scale to vibrational relaxation time scale using single-step Arrhenius model

Recently, Taylor et al. [32] computed the ignition delay time τ_{ign} in H$_2$/air detonation and compared the value of τ_{ign} with that of vibrational relaxation time of H$_2$ equilibrating in H$_2$, $\tau_{H_2-H_2}^{vib}$. Their results revealed that τ_{ign} is less than 10 $\tau_{H_2-H_2}^{vib}$ in most detonation simulations. For instance, the ratio of ignition delay time to the vibrational relaxation time is less than 3 for H$_2$ under the post-shock state of a Chapman-Jouguet detonation (i.e., at 28 atm and 1540 K) with stoichiometric H$_2$-air mixture at 1 atm and 300 K initially. In order words, the chemical reaction time scale τ_c may not be always larger than the vibration relaxation time scale τ_v and the ratio of the two time scale may alter the result obtained in this type of detonation problem. Therefore, different time ratios $\tau^{c/v} = \tau_c/\tau_v -$ 0.25, 0.5, 1, 2, 3, 4, 5, 6 and 7 were tested to investigate how the calculated half-reaction length varies in different nonequilibrium conditions. Figure 3.3 shows the change of the half-reaction length $\mathcal{L}_{1/2}$ ratio defined in section 3.1 with the selected time ratio $\tau^{c/v}$ at $E_{a,r}=50$ and $\bar{\vartheta}=2250$ K. As seen, $\mathcal{L}_{1/2}$ ratio approaches to 1 as the time ratio $\tau^{c/v}$ increases and vice versa. When $\mathcal{L}_{1/2}$ ratio is at unity, it implies that the molecular state reached the thermal equilibrium condition, and the chemical time scale is relatively large compared with the vibrational relaxation time scale, i.e. $\tau_c/\tau_v > 7$. On the other hand, if $\mathcal{L}_{1/2}$ ratio is larger than 1, this indicates that the flow is at significant vibrational nonequilibrium and the vibrational relaxation time scale τ_v (or vibrational relaxation process) becomes comparably important. Under this state, the energy transfer between

translational-rotational mode and vibrational mode reduces the effective reaction temperature for the chemical reaction. Half reaction length is then extended because of a slower reaction rate in overall.

Figure 3.3 Ratio of $\mathcal{L}_{1/2}$ for the nonequilibrium case to that of the equilibrium case versus $\tau^{c/v}$ at $E_{a,r}=50$ and $\bar{\vartheta}=2250$ K.
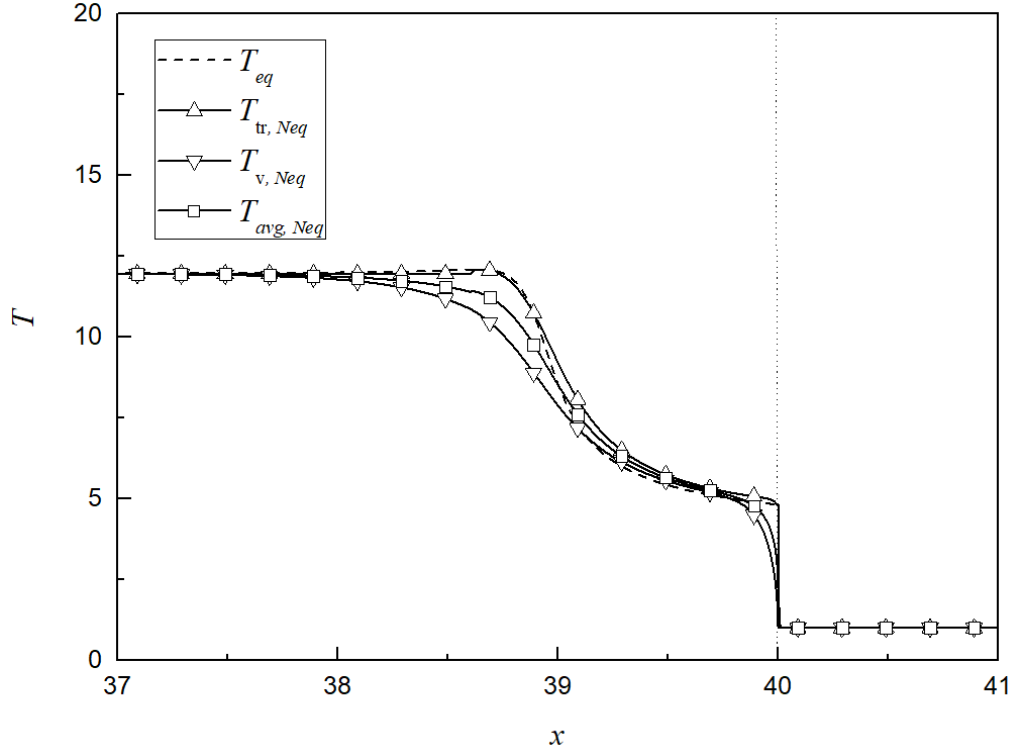
Figure 3.4 Temperature T and mass fraction of reactant Z along the ZND profile using single step Arrhenius model in the case of $\tau^{c/v}=7$ at $E_{a,r}=50$ and $\bar{\vartheta}=2250$ K.

Taking $\tau^{c/v}=7$ as an example for illustration, Figure 3.4 presents the largest $\tau^{c/v}$ case in this study where vibrational equilibrium is quickly established at the beginning of the reaction. Along the reaction profile, vibrational temperature T_v raises closely with T_{tr}. Referring to the Park's two temperature model [45] in Eq. (2.29), averaged temperature T_{avg} is thus expected to have close values with the temperature input in conventional ZND profile under the selected $\tau^{c/v}$, i.e. $T_{avg,Neq} \approx T_{eq}$. $\mathcal{L}_{1/2}$ calculated in both the conventional ZND solution and the modified ZND solution are then expected to be the same, as shown in the figure. This further demonstrates that the current extended ZND solution is not only capable of calculating the properties at vibrational nonequilibrium assumption but also the properties under thermal equilibrium.

In summary, under the given parameter settings (fixed $\gamma=1.2$ and $Q=50$), the critical $\tau^{c/v}$ at which the vibrational nonequilibrium effect is significant is suggested to be $\tau^{c/v} \leq 7$.

3.3   Dependence on characteristic vibrational temperature using single-step Arrhenius model

Regarding Table 3.1, the variation in the characteristic vibrational temperature $\bar{\vartheta}$ can be up to thousands of Kelvin. By selecting $\bar{\vartheta}$=2250 K, i.e., the vibrational temperature for O$_2$, as the unique characteristic temperature in section 3.1 and 3.2 for easier demonstration, one may argue that those results are also sensitive to the choice of $\bar{\vartheta}$. Therefore, a set of $\bar{\vartheta}$ was studied in this section from 2000 K to 6000 K with increased intervals of 1000 K in each trial.

Figure 3.5 shows the variation of $\mathcal{L}_{1/2}$ ratio with $\bar{\vartheta}$ at $E_{a,r}$=50 and $\tau^{c/v}$=0.25. As mentioned in section 3.1, $\tau^{c/v}$=0.25 was chosen such that the vibrational relaxation time scale is longer than the chemical reaction time scale across the profile to address the vibrational relaxation effect. In the selected $\bar{\vartheta}$ ranges, the variation of $\mathcal{L}_{1/2}$ ratio is within an order of 1 and decreases with the increasing $\bar{\vartheta}$. Although the $\mathcal{L}_{1/2}$ ratio decreases up to 20 % when $\bar{\vartheta}$ increases from 2000 K to 6000 K under vibrational nonequilibrium conditions, it is relatively not sensitive to $\bar{\vartheta}$, compared with the case of change in $E_{a,r}$ and $\tau^{c/v}$. Figure 3.6 compares the results of $\bar{\vartheta}$=6000 K with the results of $\bar{\vartheta}$=2250 K using the settings in section 3.2. Similarly, increasing $\bar{\vartheta}$ will bring down the $\mathcal{L}_{1/2}$ ratio under the same $\tau^{c/v}$. Both cases show the same conclusion that the $\mathcal{L}_{1/2}$ ratio approaches unity when $\tau^{c/v} \geq 7$.
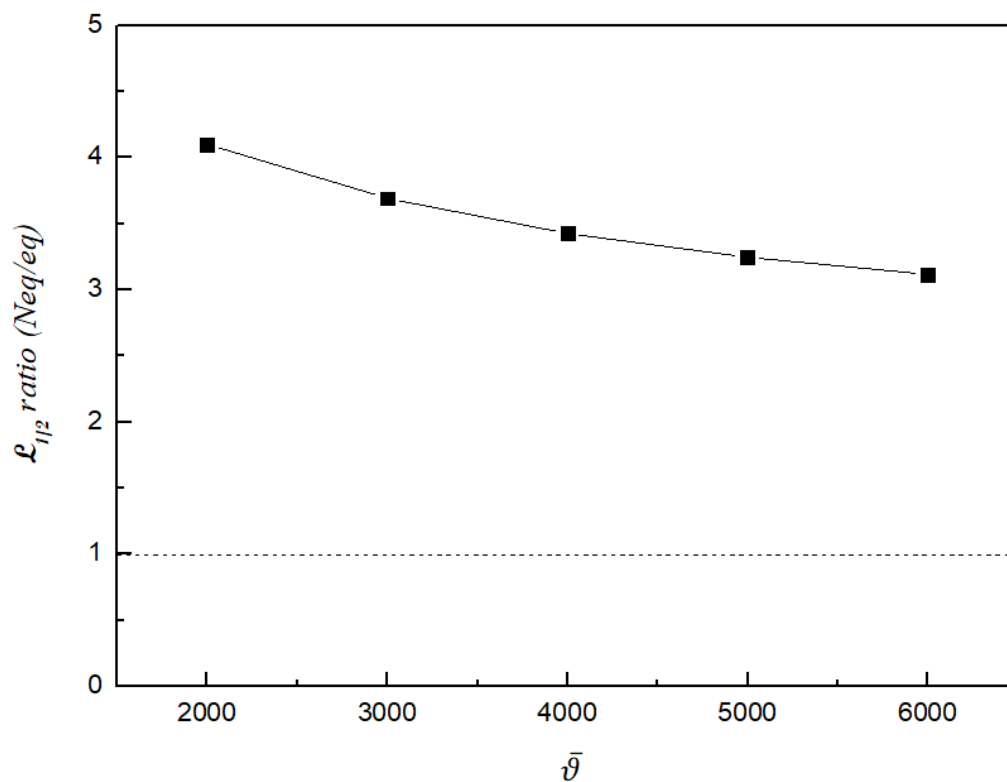
Figure 3.5 Ratio of $\mathcal{L}_{1/2}$ for the nonequilibrium case to that of the equilibrium case versus $\bar{\vartheta}$ at $E_{a,r}=50$ and $\tau^{c/v}=0.25$.
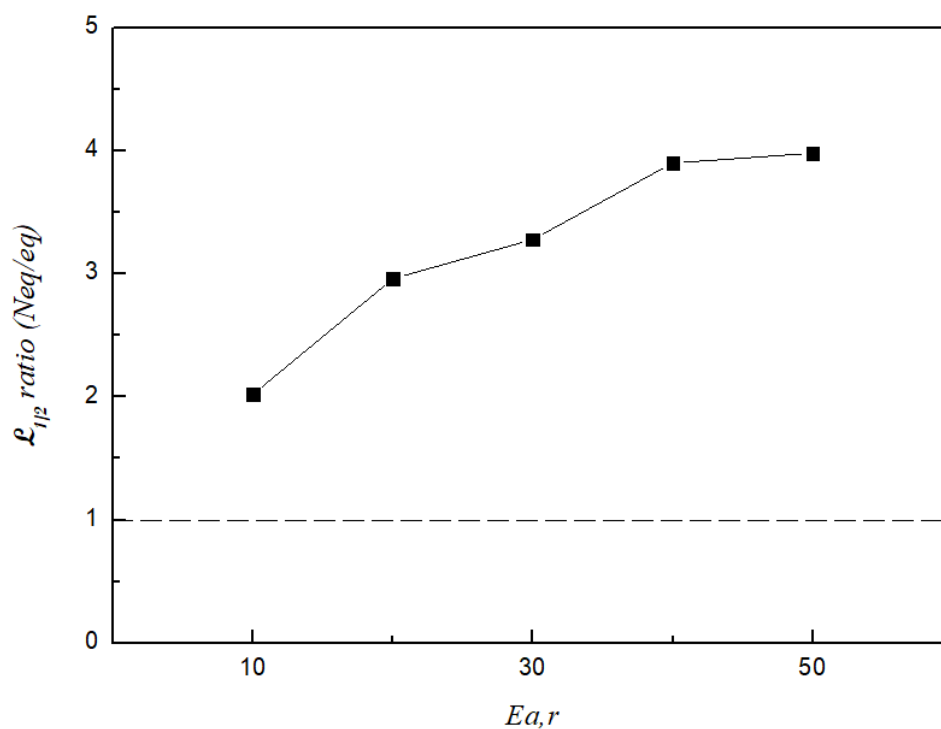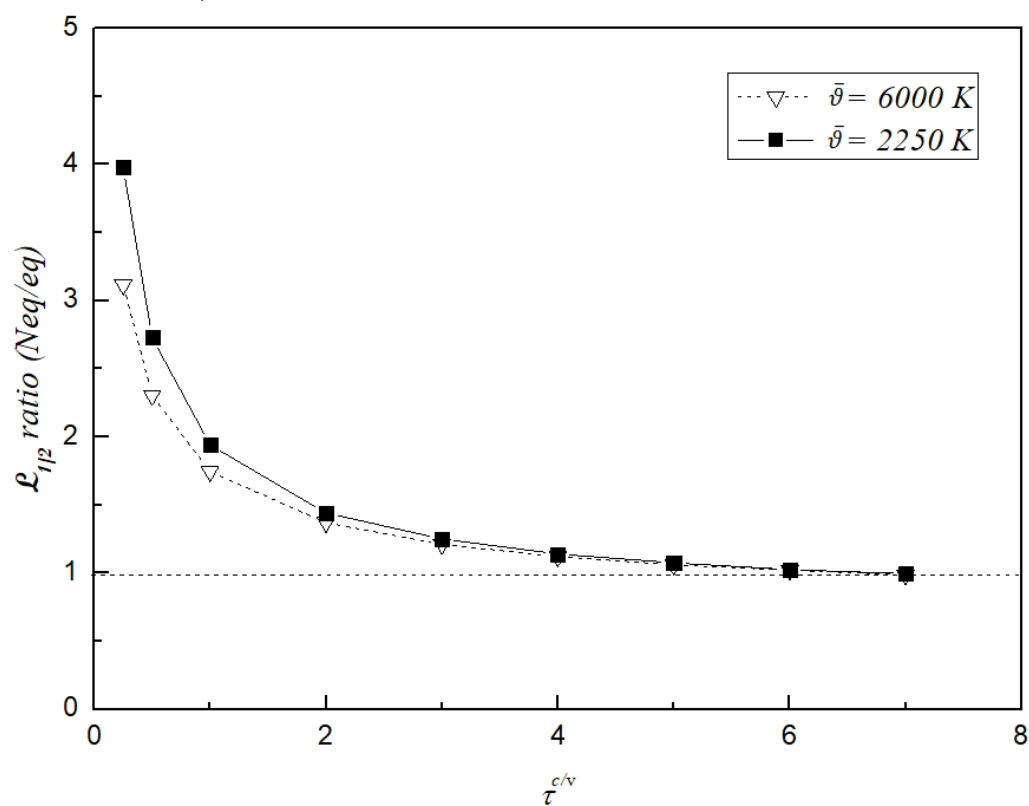

Figure 3.6 Ratio of $\mathcal{L}_{1/2}$ for the nonequilibrium case to that of the equilibrium case versus $\tau^{c/v}$ at $\bar{\vartheta}=6000$ K and at $\bar{\vartheta}=2250$ K. $E_{a,r}=50$

3.4   Dependence on time ratio of chemical reaction time scale to vibrational relaxation time scale using two-step Arrhenius model

Apart from the implementation of a single-step Arrhenius model, it is also common to apply the two-step model with an induction zone followed by a heat-released process in gas detonation simulations such as hydrogen-oxygen detonation [61]. With a change in the chemical model under extended ZND theory, a variation on time ratio $\tau^{c/v}$ were investigated while ratios of $\mathcal{L}_{ind}$ and $\mathcal{L}_{1/2}$ were set to be 1:2 under the thermal equilibrium assumption.

Figure 3.7 shows the extended ZND profile in both vibrational equilibrium and nonequilibrium cases and the time ratio of $\tau^{c/v}$=0.8 (analogous to τ_c/τ_v =0.25 for the single-step model case). Noted that $\tau_{1/2}$ defined in the current two-step model is the combination of both chemical reaction time scale τ_c and induction time scale τ_{ind}, i.e. $\tau^{c/v} \equiv \tau_{1/2}/\tau_v = (\tau_c + \tau_{ind})/\tau_v$, compared to the case of the single-step model in which $\tau^{c/v} \equiv \tau_{1/2}/\tau_v = \tau_c/\tau_v$. As shown in the figure, an induction zone is manifested right after the shock and both $\mathcal{L}_{ind}$ ratio and $\mathcal{L}_{1/2}$ ratio are elongated by a factor of 1.9 and 2.2, respectively. Similar to the approach in section 3.2, a range of time ratio $\tau^{c/v}$ are tested and presented in Figure 3.8. At this particular setting, the vibrational nonequilibrium effect is significant at $\tau^{c/v} \leq 5.5$. The shortening of critical $\tau^{c/v}$ compared to the case of using the single-step Arrhenius equation ($\tau^{c/v} \leq 7$) which shares the same setting in chemical reaction model, i.e., Eq. (2.6), implies that the consideration of the induction zone may bring a positive effect in establishing the thermal equilibrium during propagation. The $\mathcal{L}_{1/2}$ ratio of the two-step model is smaller than that of the single-step Arrhenius model at small $\tau^{c/v}$. Since the effects of three time scales τ_{ind}, τ_c and τ_v on the variation of detonation structure in two-step Arrhenius model are coupled with each other, the mechanisms involved are complicated and require further studies. Nevertheless, both the cases of using the single-step model and that of using a two-step model reveal the necessity of involving the contribution of the vibrational relaxation process in evaluating chemical reaction rates in gas detonation. Direct validation of the currently proposed ZND solutions with the numerical simulations using detailed chemistry coupled with vibrational relaxation mechanism will be presented in the next chapter.
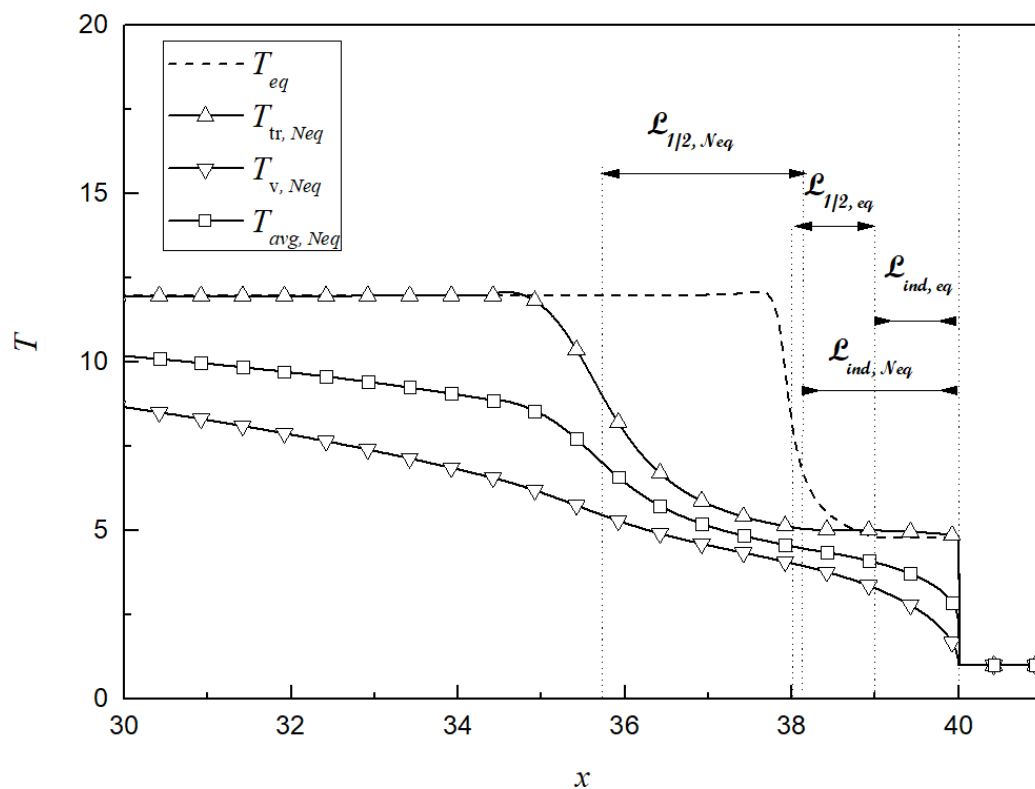
Figure 3.7 Temperature T at the vibrational equilibrium state (*eq*) and the vibrational non-equilibrium state (*Neq*) using two step Arrhenius model at $\tau^{c/v}=0.8$ and $\bar{\vartheta}=2250$ K.
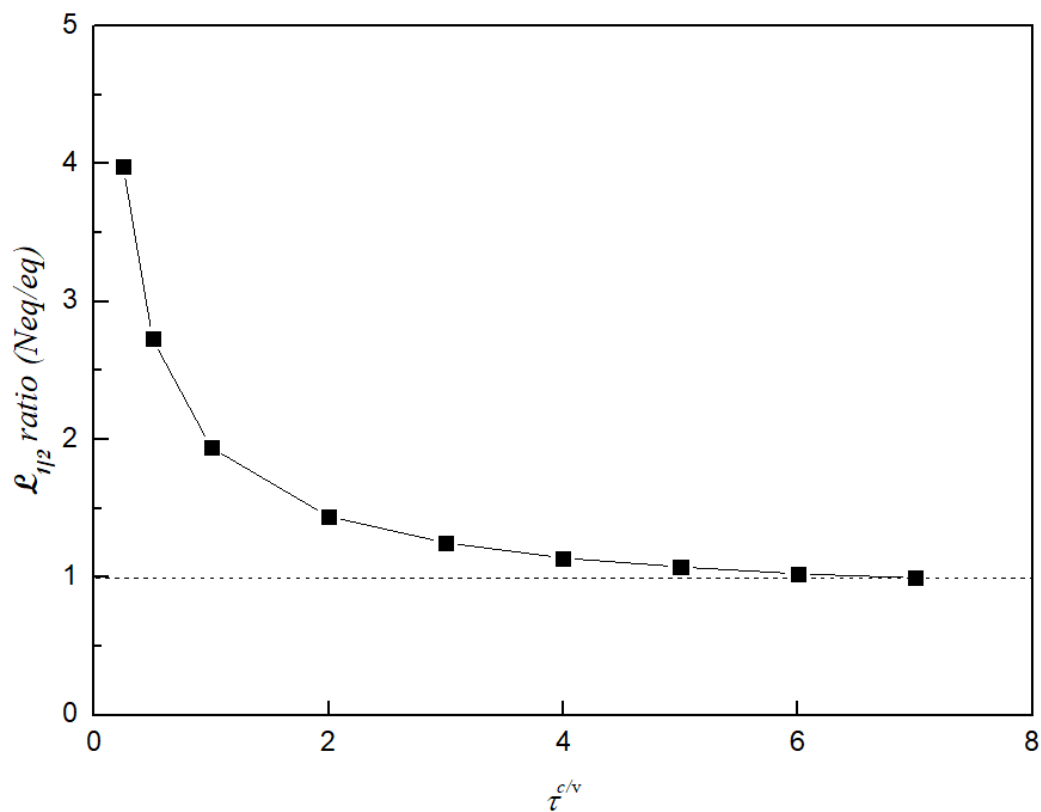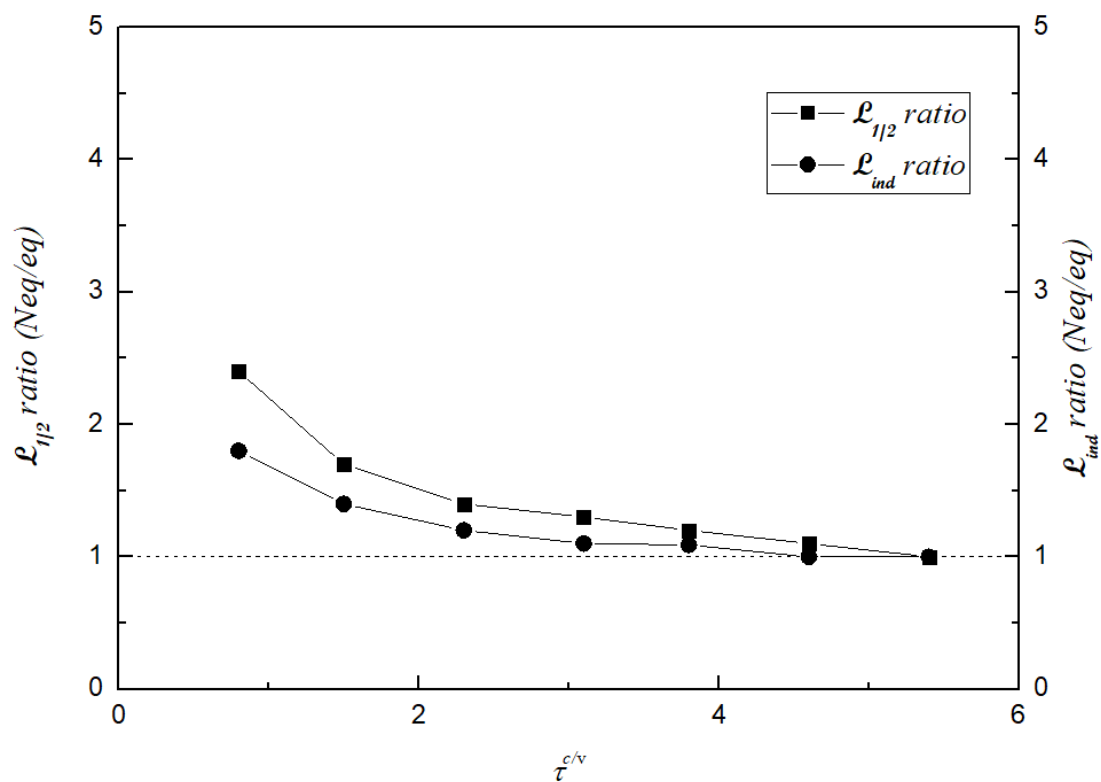

Figure 3.8 Ratios of $\mathcal{L}_{1/2}$ and $\mathcal{L}_{ind}$ for the nonequilibrium case to those of the

equilibrium case versus $\tau^{c/v}$ at $E_{a,r}$=50 and $\bar{\bar{\vartheta}}$=2250 K.

3.5　　Summary

The present investigation has performed a series of parametric studies on the extended ZND model with the consideration of the vibrational-chemical coupling effect. Through the analysis, a critical time ratio $\tau^{c/v}$ at which vibrational nonequilibrium should be concerned for each parameter change is presented. The half-reaction length is used as the standard to illustrate the vibrational nonequilibrium effect on gas detonation, which is defined as the distance from the shock front to where one-half of the reactants are consumed and is closely related to the detonation cell size. The induction length is considered in the two-step model if the chain-initiation process is substantial to the chemical reaction in the next stage. Taking the equilibrium half-reaction length as a reference, vibrational relaxation becomes dominant if the relative half-reaction length is elongated. A total of four scenarios is considered in this parametric study.

Consider the implementation of single-step Arrhenius model, the change of 1) activation energy $E_{a,r}$ in the chemical models; 2) the time ratio $\tau^{c/v}$ of the chemical half reaction time scale to the vibrational time scale, and 3) the characteristic vibrational temperature $\bar{\vartheta}$ in gaseous detonation are examined. Results reveal that the half-reaction length increases with increasing $E_{a,r}$, which is due to the slow dissociation rate under the vibrational excitation. Consequently, an extra distance (or reaction time) is required in the reaction zone under the condition of high activation energy. In the case of large $\tau^{c/v}$, i.e. $\tau_c \gg \tau_v$, the molecular vibrational state approaches equilibrium quickly and a reasonable agreement is found between the half-reaction length of the conventional ZND model and the extended ZND solution. The importance of the vibrational nonequilibrium effect on gas detonation is demonstrated when the scale of τ_v is comparable with τ_c, i.e. low $\tau^{c/v}$. Based on the study, dependence on the selected $\bar{\vartheta}$ range according to the analysis of hydrogen-related detonation is less significant compared with the change of $E_{a,r}$ and $\tau^{c/v}$. With the parameter setting of γ=1.2, Q=50, $\bar{T}_0$=300 K, R=259.8 J/kg K, and $E_{a,r}$=50 using single-step Arrhenius model, the criteria for that the vibrational relaxation mechanism should be considered is suggested to be $\tau^{c/v} \leq 7$, under the chosen $\bar{\vartheta}$. For the cases in which an induction process is considered in the two-step Arrhenius model, the criteria for that the vibrational relaxation mechanism should be considered is suggested to be $\tau^{c/v} \leq 5.5$, under the same parameter setting in the chemical reaction model. The result provides an insight that vibrational relaxation, which starts right after the shock in the induction zone for the cases using the two-step Arrhenius model, can substantially reduce $\mathcal{L}_{1/2}$ ratio compared to the case of the single-step Arrhenius model at small $\tau^{c/v}$. The critical $\tau^{c/v}$

thus decreases. This criterion depends on the fixed parameter setting in induction and reaction models.

Chapter 4 Prediction of half reaction length for H₂/O₂/Ar detonation with extended detonation model

As mentioned in the previous section, the establishment of the extended ZND model not only helps to reveal the vibrational-chemical coupling effect in fundamental detonation physics, but also provides a clue in predicting properties from large-scale detonation simulation. In this chapter, the possibility of using the extended ZND model to predict the half-reaction length for $H_2/O_2/Ar$ detonation simulation is investigated. For purposes of comparison with the numerical results under the state of vibrational nonequilibrium, data obtained from the one-dimensional (1D) CE/SE simulations with detailed chemical kinetics under thermal equilibrium assumption are first used to determine the parameters in both single-step Arrhenius equation (Eq. (2.6)) and two-step chain branching kinetics in the extended ZND model.

Considering the detonation driven by chain-branching kinetics, Ng et al. [21] introduced a temperature-sensitive Arrhenius equation with a step function to include the thermally neutral induction period right after the shock. This induction Arrhenius equation is further combined with the heat release stage and form a two-step model, formulated as follows (normalized with the initial state):

$$\omega_\beta = \frac{d\beta}{dt} = H(1-\beta) \cdot k_{ind}\exp\left[E_{a,ind}\left(\frac{1}{T_{vn}} - \frac{1}{T}\right)\right] \tag{4.1}$$

$$H(1-\beta)\begin{cases} = 1 \ if \ \beta \ < 1 \\ = 0 \ if \ \beta \ \geq 1 \end{cases} \tag{4.2}$$

$$\omega_\lambda = \frac{d\lambda}{dt} = [1 - H(1-\beta)] \cdot k_r(1-\lambda)\exp\left(-\frac{E_{a,r}}{T}\right) \tag{4.3}$$

The step function $H(1-\beta)$ in Eqs. (4.1) - (4.3) ensures that the heat release stage starts only if the induction period is ended at $\beta \geq 1$, while β is set to be 0 initially.

Hydrogen-oxygen detonation with 70% Argon dilution under an initial temperature of 300K is the selected condition in this study, in which the role of vibrational nonequilibrium effect has been thoroughly discussed by Shi et al. [36] before. In their study, a detailed chemistry model for high-pressure and high-temperature hydrogen

combustion involving 25 elementary reactions among 9 species by Burke et al. [62] is implemented, and a mesh size of 5 μm is sufficient for all simulations. For the calculation in vibrational relaxation mechanism, $\bar{\tau}_v$ is evaluated by both the primary reactants H2 and O2, with their corresponding species interactions, i.e. H2-H2, H2-O2, H2-Ar and O2-H2, O2-O2, O2-Ar, respectively. The mass fraction of the species H2:O2:Ar are set to be 2:1:7, which is analogous to the initial reactant mass fractions in the numerical simulation.

This chapter in particular aims at finding a simplified chemical-vibrational kinetics in the extended ZND model such that the half-reaction length predicted can be as close to that in numerical simulation, while the fundamental detonation physics can be retained in the meantime. The selected simplified model is then implemented in a 1D numerical simulation for justification. Notably, the content presented in this chapter has been published in [63].

4.1   Modified single-step & two-step Arrhenius model to fit with detail chemistry model

To obtain a similar reaction profile of the numerical simulation using detailed chemistry, the extended ZND model with both modified single-step and two-step models were integrated across the reaction zone with initial pressure set as 0.1, 0.2, 0.3, and 0.4 atm respectively. Following the approach in Taylor et al.'s work [64], the parameters in the single-step model (i.e., Eq. (2.6)) was reduced by a fitting process to the detailed chemistry model. In their discussion, Q and γ in the single-step model were fixed such that CJ detonation velocity (and hence the same CJ Mach number M_{CJ}) is always matched and then the preexponential factor k was adjusted with several choices of E_a to get the desired half reaction length $\mathcal{L}_{1/2}$ (usually set $\mathcal{L}_{1/2} = 1$ for easy reference). The choice of E_a followed the analysis of the thermodynamic data in detail chemical kinetics recently developed by Burke et al. [62], which has also been adopted by Shi et al. [36] and Taylor et al. [32], while the values of M_{CJ} and γ (on the product side) were taken from the results computed by Shi et al. [36] under the thermal equilibrium state. Q was evaluated through the relation $M_{CJ} = (2(\gamma^2 - 1)Q)^{1/2}$.

Considering the two-step chain-branching kinetics in Eqs. (4.1) - (4.3), $E_{a,ind}/T_{vn}$ and $E_{a,r}/T_{vn}$ were set to be 4 and 1, respectively, for the H2-O2 mixture in all initial pressure cases to ensure that $E_{a,ind} \gg E_{a,r}$, as mentioned in Ng et al.'s work [21]. Same values of γ and Q were adopted as calculated in modified single-step model. According to the numerical simulation results of Shi et al. [3], the ratio of induction zone length $\mathcal{L}_{ind}$

to reaction zone length $\mathcal{L}_r$ was set to be 1:1 (In other words, the ratio of $\mathcal{L}_{ind}$ to $\mathcal{L}_{1/2}$ is 1:2). Here, the reaction zone length $\mathcal{L}_r$ is defined as the zone starts from the end of the induction zone to where half of the reactant is consumed. A summary of other parameters is listed in Table 4.1. Noted that thermodynamic properties in von Neumann state were evaluated using Rankine-Hugoniot relation. Figure 4.1 presents the non-dimensionalized temperature and reactant mass fraction profiles at the thermal equilibrium state using (a) the modified single-step and (b) the two-step models, compared with those computed by CE/SE simulations using the detailed chemistry model. It is expected that the two-step model shows a better fitting to the numerical simulation than the single-step counterpart as an induction zone $\mathcal{L}_{ind}$ can be manifested clearly in the comparison. Although this induction process is absent in the modified single-step model, a fairly similar trend is still observed.

Table 4.1 Normalized parameters fitted with the data of 1D numerical simulation using the chemical kinetic model of Burke et al. [62].

Initial Pressure (atm)	γ (product side)	Q	E_a/T_{vn} (Single-step model)
0.1	1.45	11.9	4.2
0.2	1.44	13.7	4.4
0.3	1.44	15.0	4.4
0.4	1.44	15.3	4.4
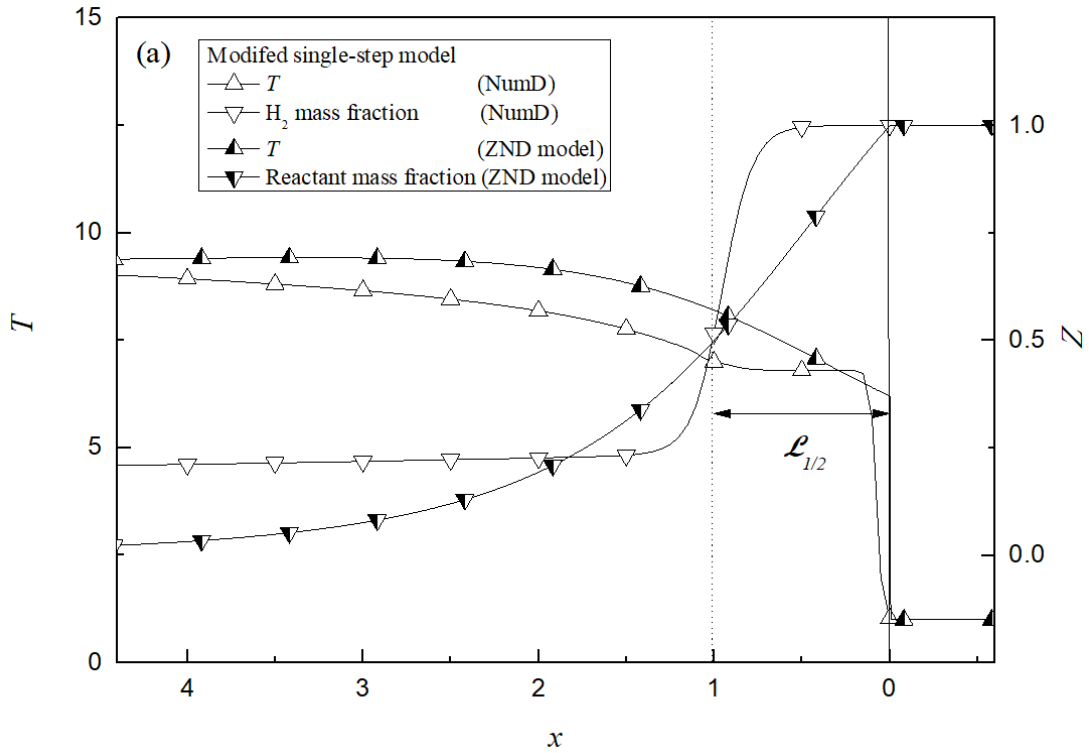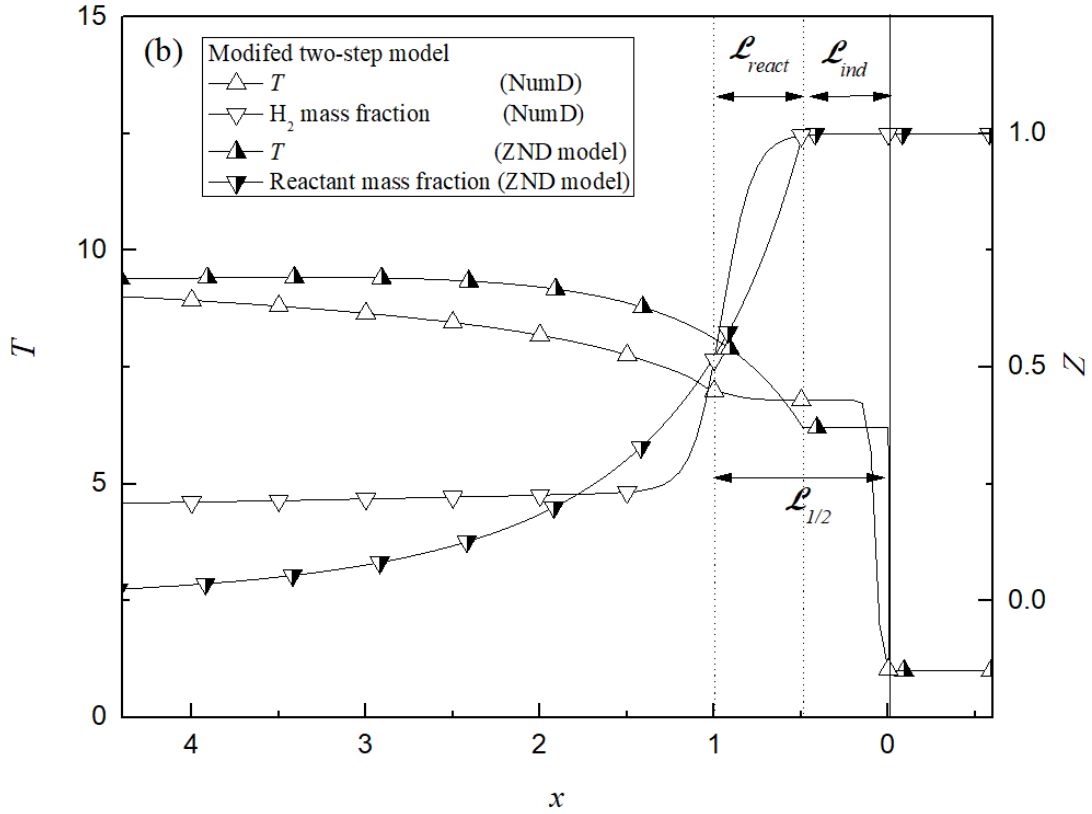
Figure 4.1 Comparison of normalized temperature T and reactant mass fraction Z profiles at the thermal equilibrium state using (a) the modified single-step model (b) the two-step model in the extended ZND model, with the numerical simulation results (NumD) using detailed chemistry model. Shock wave is encountered at normalized $x=$ 0 and propagates from left to right.

4.2 Comparison of half reaction length ratio estimated from the extended detonation model with numerical simulation

In the 1D numerical simulation with a detailed chemistry model, all possible species in the reaction are involved, whereas only a single species is considered in the extended ZND model with simplified chemistry. Therefore, in this study, either reactant H_2 or O_2 was chosen as the major species in the model for simplification and for purposes of comparison with the referred 1D CE/SE simulations. The two choices of reactant in the simplified chemical model is manifested in terms of the characteristic vibrational temperature $\bar{\vartheta}$ (i.e. $\bar{\vartheta}_{O_2}=2250$ K or $\bar{\vartheta}_{H_2}=5989$ K as referred from [65]). A total of four scenarios with vibrational nonequilibrium assumption were conducted in each initial pressure case as listed below.

Case (i): $\bar{\vartheta}_{H_2}$ is adopted in the modified single-step model.

Case (ii): $\bar{\vartheta}_{H_2}$ is adopted in the modified two-step model.

Case (iii): $\bar{\vartheta}_{O_2}$ is adopted in the modified single-step model.

Case (iv): $\bar{\vartheta}_{O_2}$ is adopted in the modified two-step model.

Figure 4.2 shows the half-reaction length ratios calculated from both the equilibrium and the nonequilibrium numerical simulations and from the extended ZND model with different characteristic vibrational temperature $\bar{\vartheta}$ under a selected initial pressure range. The 1D numerical simulations with thermal equilibrium (*eq*) and nonequilibrium assumptions (*Neq* (NumD)) in each initial pressure case are served as the benchmark for comparison. The half-reaction length ratio, $\mathcal{L}_{1/2}$ ratio is defined as the ratio of the half-reaction length at the vibrational nonequilibrium state (*Neq*) to the half-reaction length at the vibrational equilibrium state (*eq*), similar to the definition in Chapter 3. Notably, $\mathcal{L}_{1/2}$ ratio = 1 in the equilibrium simulation (shown as the dashed line in Figure 4.2) is set for the comparison with different predicted results. Focusing on the results under vibrational nonequilibrium, although the exact half-reaction lengths computed in different initial pressure cases are not the same (as shown in Shi et al.'s work [36]), the normalized half-reaction length ratio show small variations among different initial pressures cases. The prediction from the extended ZND model shows an elongation of half reaction length under vibrational nonequilibrium effect in every case, no matter $\bar{\vartheta}_{H_2}$ or $\bar{\vartheta}_{O_2}$ is applied in evaluating the vibrational relaxation time scale. Their growth trends of $\mathcal{L}_{1/2}$ ratio are similar to that of the vibrational nonequilibrium simulations using a detailed chemistry model. It implies that no matter what chemical kinetics is implemented in detonation theory or simulation, the vibrational nonequilibrium effect is crucial in the H$_2$/O$_2$ detonation and can be always manifested even in simplified chemical models in terms of elongated half-reaction length. These observations agree well with the conclusion discussed by Shi et al. [36] and that summarized in Chapter 3. The larger distance in reaction profile due to the lower chemical reaction rate across the profile under the presence of a vibrational relaxation mechanism can be explained by the inter-transfer mechanism of translational-rotational energy to vibrational energy.

Besides, as shown in Figure 4.2, better agreement with the 1D numerical result is observed if $\bar{\vartheta}_{H_2}$(Case (i) and (ii)) is used for prediction instead of $\bar{\vartheta}_{O_2}$ (Case (iii) and (iv)). The accuracy of prediction by using $\bar{\vartheta}_{H_2}$ in the single-step model and the two-step model ranges approximately from 1% to 11% and from 3% to 7%, respectively, whereas that by $\bar{\vartheta}_{O_2}$ ranges approximately from 14% to 20% and from 18% to 20%, respectively (also see Table 4.2). The closer prediction with numerical simulation by using $\bar{\vartheta}_{H_2}$ implies that H$_2$ might be a dominant reactant in the vibrational relaxation

mechanism for this particular reaction process. A similar conclusion from computation results has been discussed by Taylor et al.'s analysis [33] on estimating the vibrational nonequilibrium time scale in hydrogen-air detonation, in which they showed that vibrational relaxation time of H_2 is much longer than that of O_2, indicating the dominant role of H_2 in the vibrational relaxation process. Notably, regarding the natures of the selected chemical models in this study, the two-step model consists of more variables compared with that of the single-step model. In other words, the degree of freedom is much larger in the two-step model. Therefore, the choice of parameters (such as the activation energy or heat release term) must be more critical in order to have better predictions for the two Arrhenius equations representing the two zones
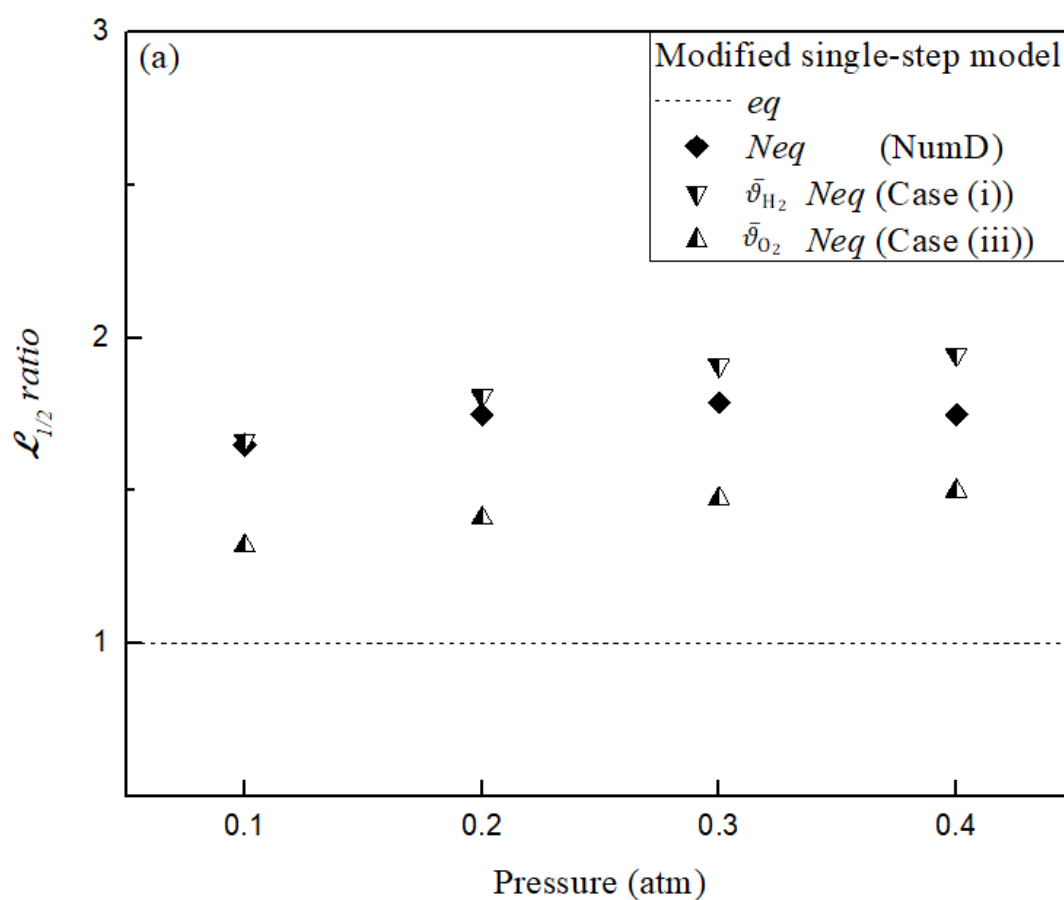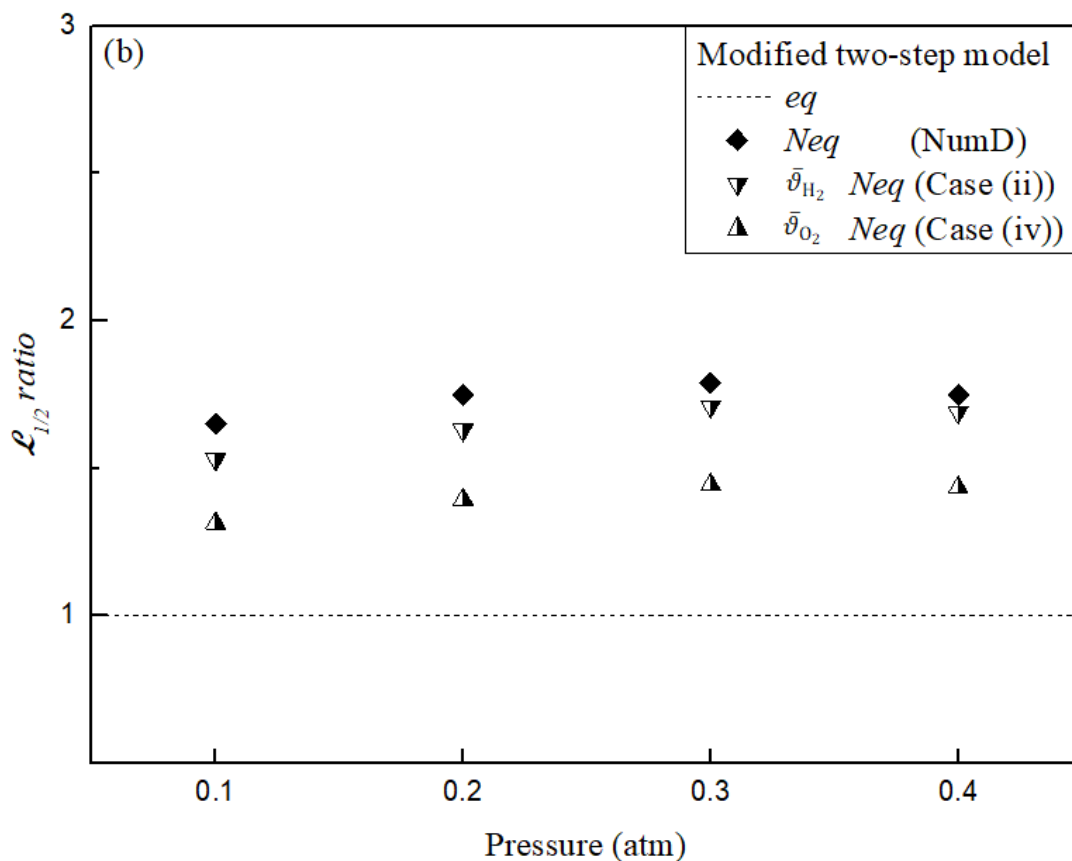
Figure 4.2 Half reaction length ratio versus initial pressure when considering (a) modified single-step model (b) modified two-step model in the extended ZND model with the reactant H_2 as the major species under the *Neq* state (Case (i) & Case (ii)) and the reactant O_2 as the major species under the *Neq* state (Case (iii) & Case (iv)). The results of 1D numerical simulations with the detailed chemistry model (NumD) under vibrational equilibrium state (*eq*) and vibrational nonequilibrium state (*Neq*) are also shown for comparison.

4.3 Implementation of the simplified chemical models into numerical simulation

Based on the result in section 4.2, adopting $\bar{\vartheta}_{H_2}$ in simplified chemistry yields a better prediction of the half-reaction length than that of $\bar{\vartheta}_{O_2}$. To justify the appropriateness of using these models in the prediction, 1D CE/SE numerical simulations were further conducted using modified single-step and two-step chemical models with $\bar{\vartheta}_{H_2}$ as the factor in evaluating the properties across the reaction profile, instead of the detailed chemistry model by Burke et al. [62]. The solution would be converged if 40 points per half-reaction length of the conventional ZND solution were used. Summary of cases with different initial pressure and different chemical models are presented in Table 4.2 and Table 4.3.

Table 4.2 Computed half-reaction length and calculation of corresponding $\mathcal{L}_{1/2}$ ratio in numerical simulation with simplified chemistry and $\bar{\vartheta}_{H_2}$ (NumS).

Chemical model	Pressure (atm)	eq $\mathcal{L}_{1/2}$	Neq $\mathcal{L}_{1/2}$	$\mathcal{L}_{1/2}$ ratio
Single-step	0.4	1.60	3.25	2.03
	0.3	1.58	3.18	2.01
	0.2	1.50	2.88	1.92
	0.1	1.40	2.45	1.75
Two-step	0.4	1.40	2.40	1.71
	0.3	1.40	2.45	1.75
	0.2	1.38	2.20	1.59
	0.1	1.33	1.99	1.50

Table 4.3 Comparison of $\mathcal{L}_{1/2}$ ratio among selected chemical models in simulation and extended ZND model.

Pressure (atm)	$\mathcal{L}_{1/2}$ ratio at Neq state				
	NumD	Case (i) ($\bar{\vartheta}_{H_2}$, Single-step)		Case (ii) ($\bar{\vartheta}_{H_2}$, Two-step)	
		ZND (%diff)	NumS (%diff)	ZND (%diff)	NumS (%diff)
0.4	1.75	1.95 (11.4%)	2.03 (16.0%)	1.69 (3.4%)	1.71 (2.3%)
0.3	1.79	1.91 (6.7%)	2.01 (12.3%)	1.71 (4.5%)	1.75 (2.2%)
0.2	1.75	1.81 (3.4%)	1.92 (9.7%)	1.63 (6.9%)	1.59 (9.1%)
0.1	1.65	1.67 (1.2%)	1.75 (6.1%)	1.53 (7.3%)	1.50 (9.1%)

Note: ZND = from extended ZND model;

NumS = from numerical simulation with simplified chemistry;

NumD = from numerical simulation with detailed chemistry;

%diff = |[(ZND or NumS)-NumD]/NumD x 100%|

Take the case of initial pressure at 0.4 atm for the single-step model as an example, the half-reaction length computed under vibrational equilibrium assumption is 1.60, whereas that computed under vibrational nonequilibrium assumption is 3.25. The $\mathcal{L}_{1/2}$ ratio calculated would be 3.25/1.60 = 2.03 as shown in Table 4.2 and Table 4.3 under Case (i) NumS. Other $\mathcal{L}_{1/2}$ ratio calculations are self-explanatory.

Referring to Table 4.3, the difference in the $\mathcal{L}_{1/2}$ ratio between the predicted solutions from extended ZND model (ZND) and the simulated solutions with simplified single-step and two-step chemical models (NumS) has the difference (%diff) at most of 16% with the simulations with detail chemistry model (NumD). At higher initial pressure range (i.e. the case of 0.4 and 0.3 atm), the two-step model shows a better prediction among the selected case study (with the smallest difference of 2.2%), while the one

with the single-step model shows better fitting at the lower initial pressure range (i.e. the case of 0.1 atm with the smallest difference of 1.2%). Overall, the use of a simplified single-step/two-step model can fairly predict the half-reaction length computed using a detailed chemistry model in the selected initial pressure range, and the appropriateness of using the extended ZND model is justified.

4.4   Practical implications

It is well known that the conventional ZND model is an ideal steady-state solution for the Euler simulations in a detonation problem. This chapter demonstrates that the extended ZND model with the consideration of vibrational relaxation mechanism is also analytically comparable with the steady-state solution computed under the same nonequilibrium assumption. Compared with the numerical simulations using a detailed chemistry model, the current extended ZND model and the simplified chemical models (i.e. single-step or two-step Arrhenius model) are much more economical to predict the half-reaction length and accordingly the detonation cell size in large scale H_2/O_2 detonation simulations under the state of vibrational nonequilibrium, while physics in chemical-vibrational coupling mechanisms mostly retained.

4.5   Summary

An extended ZND model with the consideration of the chemical-vibrational coupling effect presented in Chapter 3 was applied in this study to predict the half-reaction lengths of cases with stoichiometric $H_2/O_2/Ar$ detonation under different initial pressures. By choosing $\bar{\vartheta}_{H_2}$ or $\bar{\vartheta}_{O_2}$ alone in the extended ZND model along with the modified single-step and two-step chemical models, four scenarios under different initial pressures were demonstrated for model prediction. In summary, the matching of the prediction from the extended ZND model with single-step/two-step chemistry and that from numerical simulation using detailed chemistry are satisfactory. The accuracy of half reaction length prediction to the benchmark value by using $\bar{\vartheta}_{H_2}$ in the single-step model and that in the two-step model ranges approximately from 1% to 11% and from 3% to 7%, respectively, whereas that by $\bar{\vartheta}_{O_2}$ ranges approximately from 14% to 20% and from 18% to 20%, respectively. The closer predictions by using $\bar{\vartheta}_{H_2}$ (i.e. H_2 as the major reactant species) compared with those using $\bar{\vartheta}_{O_2}$ (i.e. O_2 as the major reactant species) indicate that H_2 is a dominant species in the vibrational relaxation mechanism for this particular case of $H_2/O_2/Ar$ detonation. To further justify whether the simplified chemical models are applicable in unsteady Euler numerical simulations, one-dimensional CE/SE simulations implemented with the modified single-step and

two-step chemical models were performed and the computed half-reaction lengths were compared with the results calculated from the extended ZND model and the simulations using the detail chemistry model under the same vibrational nonequilibrium assumption. Small discrepancies with the simulation using a detailed chemistry model were observed. To conclude, the extended ZND model is justified and can be treated as an analytical tool to predict the half-reaction length and accordingly the detonation cell size in large scale H_2/O_2 detonation simulations under thermal nonequilibrium assumption, while physics in chemical-vibrational coupling mechanisms mostly retained.

Chapter 5 Direct numerical simulation on vibrational-chemical coupling effect in one-dimensional stability

After the studies of the simplified vibrational-chemical coupling effect in gas detonation in previous chapters, it is interesting to know if the detonation stability behaviour also changed under this effect. Therefore, in this chapter, the stability of a detonation with this coupling mechanism is preliminarily investigated by utilizing direct numerical simulation. The formulation of the reactive Euler equations normalized with the initial state follows the discussion in section 2.3, and the corresponding steady ZND solution is given as the initial condition in the simulation. From Sharpe and Falle's work [25], they have identified that the setup of the initial steady solution is crucial in detonation stability analysis. Notably, the time ratio $\tau^{c/v}$ is adopted to represent the different states of thermal nonequilibrium in the detonation.

To obtain a numerical convergence in this study, an effective grid resolution of 128 points per half-reaction zone length is suggested in the literature [25], and this would be verified in this chapter also. Assuming the detonation wave propagates from left to right, a zero gradient boundary condition was initially set up at the left-hand side with a half-reaction length at least 1000 behind the shock position, such that the boundary effect could be avoided during computation.

The present numerical study aims to investigate the possibility of a shift in neutral stability boundary for the selected unstable case at different $\tau^{c/v}$. γ=1.2, Q=50, and ϑ=20 were fixed in the 1D detonation simulation. Note that ϑ was chosen arbitrarily here for easy demonstration. The detonation stability boundary for thermal equilibrium state in the presence of vibrational energy is determined in the first step, and two mildly unstable cases for a CJ detonation and an overdriven detonation are then investigated by changing the time ratio $\tau^{c/v}$. Through this study, a critical time ratio for which the solution converges to the equilibrium state is demonstrated.

5.1 Stability boundary for equilibrium state with vibrational energy included

Following the approach discussed in Shi et al. [36], the relaxation rate equation

(Landau-Teller model described in Eq. (2.30)) is always neglected in the computation of the thermal equilibrium case with vibrational energy term included in the energy equation, i.e., Eq. (2.40), since the vibrational equilibrium is assumed to be quickly established right behind the shock. In this case, the condition of $T_{tr} = T_v$ is held within the reaction zone.

To determine the stability boundary under this state, the shock pressure histories were computed by varying the activation energy E_a at fixed γ, Q and ϑ. Based on these histories obtained, the variation of the leading shock pressure of the detonation wave could be shown clearly as a function of time, while the shock pressure is normalized with respect to the von-Neumann pressure. With the recorded shock pressure grows with time, the detonation is regarded as unstable, and the behavior of the shock pressure profile would be vice versa in the case of stable detonation. For instance, the pressures histories of detonation at stable or unstable conditions are presented in Figure 5.1. As seen in Figure 5.1a for E_a=26.30, the perturbation of the propagating detonation decays with time, and this implies that a stable condition would be reached eventually. In contrast, the perturbation kept growing in the case of E_a=26.70 in Figure 5.1b. These results indicated that the neutral stability limit should lie within these two values, and it is found that the limit is approximately at E_a=26.47, above which the detonation is unstable. Compared with the neutral stability limit computed at thermal equilibrium without considering vibrational energy for the same γ and Q which is E_a=25.27 [25], the presence of vibrational energy stabilizes the detonation and raises the stability boundary accordingly.

Besides, a grid convergence study is conducted and is presented in Table 5.1. The determination of neutral stability limit under different resolutions confirms that 128 grids per half-reaction length of the steady-state ZND detonation is sufficient to obtain a converged value.

Table 5.1 Determination of neutral stability boundary for different numerical resolutions.

Grids per half-reaction length	E_a
8	26.36
16	26.38
32	26.44
64	26.46
128	26.47
256	26.47
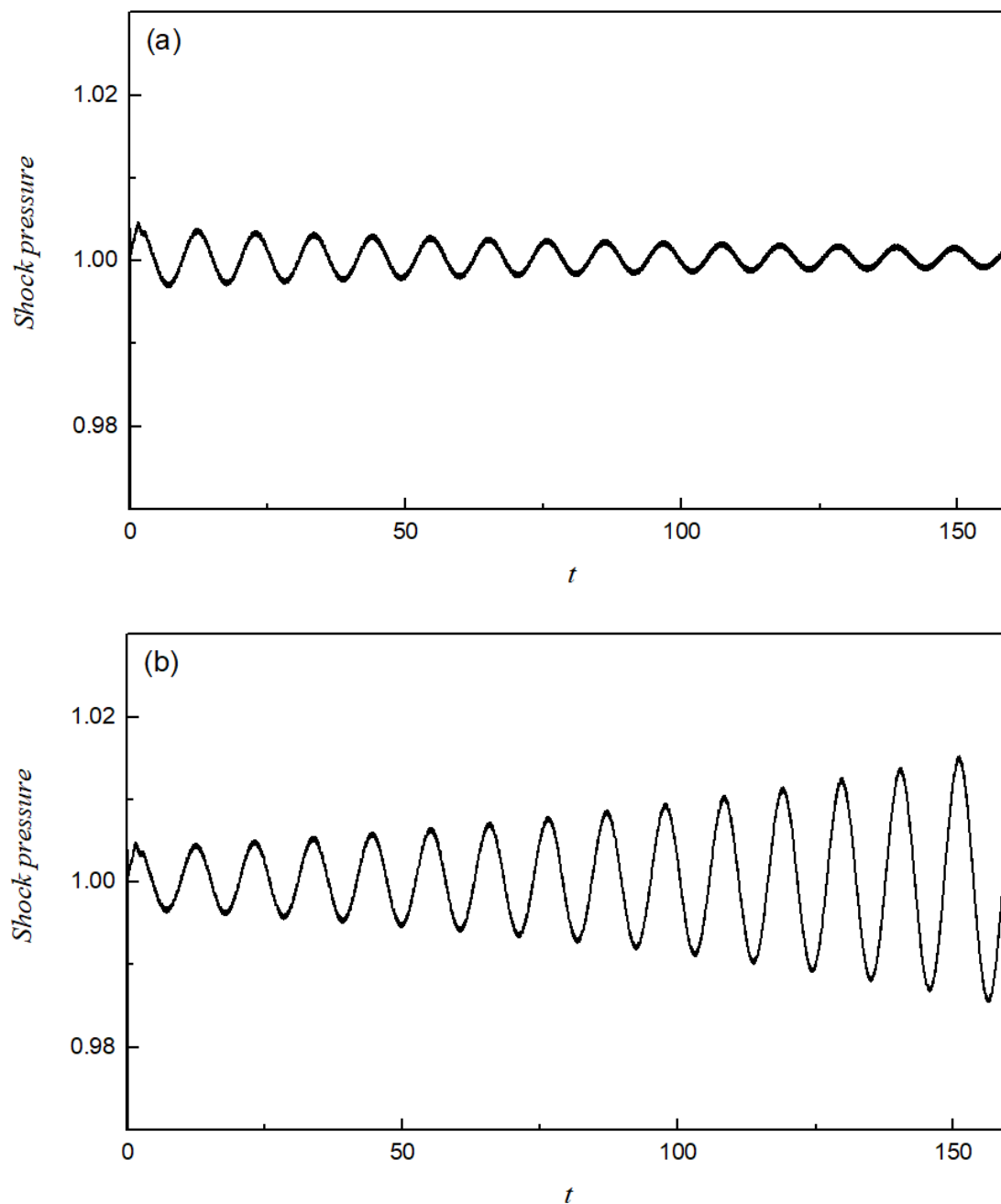
Figure 5.1 Shock pressure history at a) E_a=26.30 and b) E_a=26.70 under the thermal equilibrium (*eq*) assumption. Other fixed parameters are Q=50, γ=1.2, ϑ=20 and f=1.0.

5.2 Shock pressure history of a mildly unstable CJ detonation with different time ratio

It is known that detonation becomes unstable at high activation energy E_a. To study whether the propagating detonation would be stabilized at different states of vibrational nonequilibrium, the simulation is conducted at different ranges of $\tau^{c/v}$ in the case of

E_a=27, which is inherently unstable. Figure 5.2 shows the shock pressure histories for $\tau^{c/v}$ at 3, 5, 7, and 9 while the equilibrium cases are served as the benchmark. Generally, the peak amplitude is smaller and the period of oscillation becomes longer at small $\tau^{c/v}$. For instance, the averaged period of oscillation is 12.89 at $\tau^{c/v}$=3, whereas it is 10.66 at equilibrium case.

Figure 5.3 shows the temporal variations of peak pressure difference evaluated from the corresponding profiles in Figure 5.2. These data are obtained from the subtraction between each pressure peak and the 1st peak value along the shock pressure histories. Indeed, the 1st peak amplitude serves as a reference to identify whether the perturbation grows or decays with time. It is found that the decay rate of peak amplitude becomes faster at smaller $\tau^{c/v}$, and this deviates from the findings that a growing perturbation is expected at the same E_a under thermal equilibrium state. Both the decay of pulsation and the extended period of oscillation implies that the detonation is stabilized at the state of vibrational nonequilibrium. Refer to the definition of $\tau^{c/v} \equiv \tau_c/\tau_v$, the more thermal nonequilibrium is presented if $\tau^{c/v}$ decreases, denoting that τ_c is comparable with τ_v. At $\tau^{c/v}$=9, the recorded pulsation increases as time goes on, and this indicates that the detonation is unstable as it approaches the thermal equilibrium, i.e., $\tau_c \gg \tau_v$, and this similar trend is also observed in the benchmark result. With several computations in the range of 7< $\tau^{c/v}$ < 9, the critical $\tau^{c/v}$ for which the detonation is stabilized at E_a=27 is determined to be 7.2.

The stabilization in detonation under the thermal nonequilibrium is attributed to the exchange of energy between translation-rotational mode and vibrational mode, which reduces the overall chemical reaction rate eventually. This phenomenon is consistent with the investigation of change in half-reaction length at vibrational nonequilibrium in Chapter 3, in which the elongated half-reaction length at low $\tau^{c/v}$ is reported. In other words, it can be foreseen that the neutral stability limit of the activation energy shifts to a higher level if vibrational relaxation is significant in chemical kinetics.
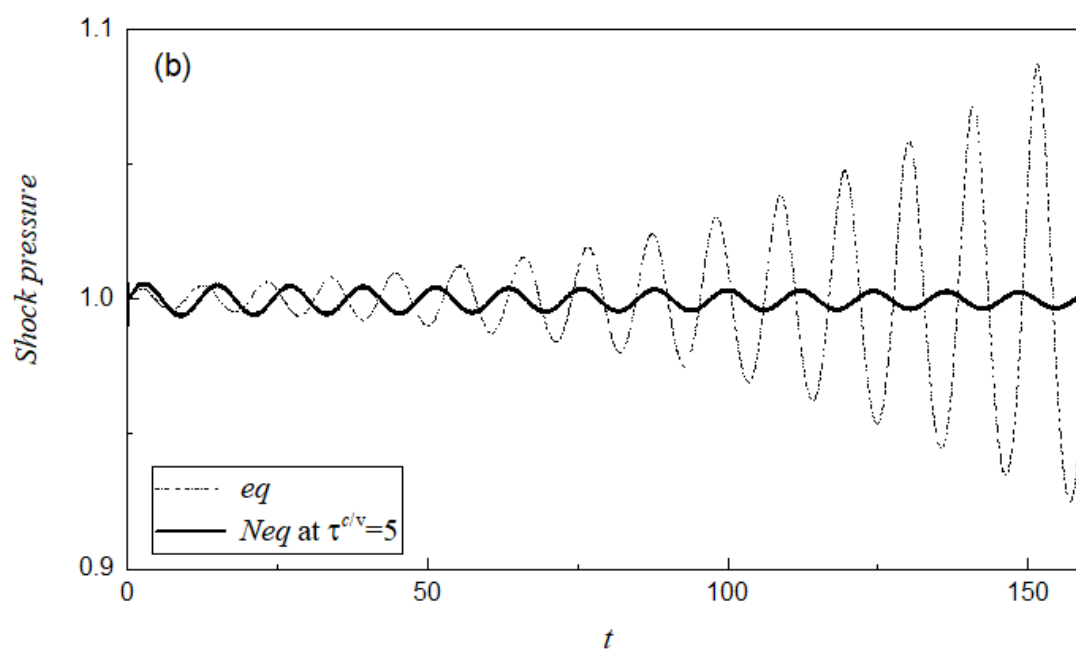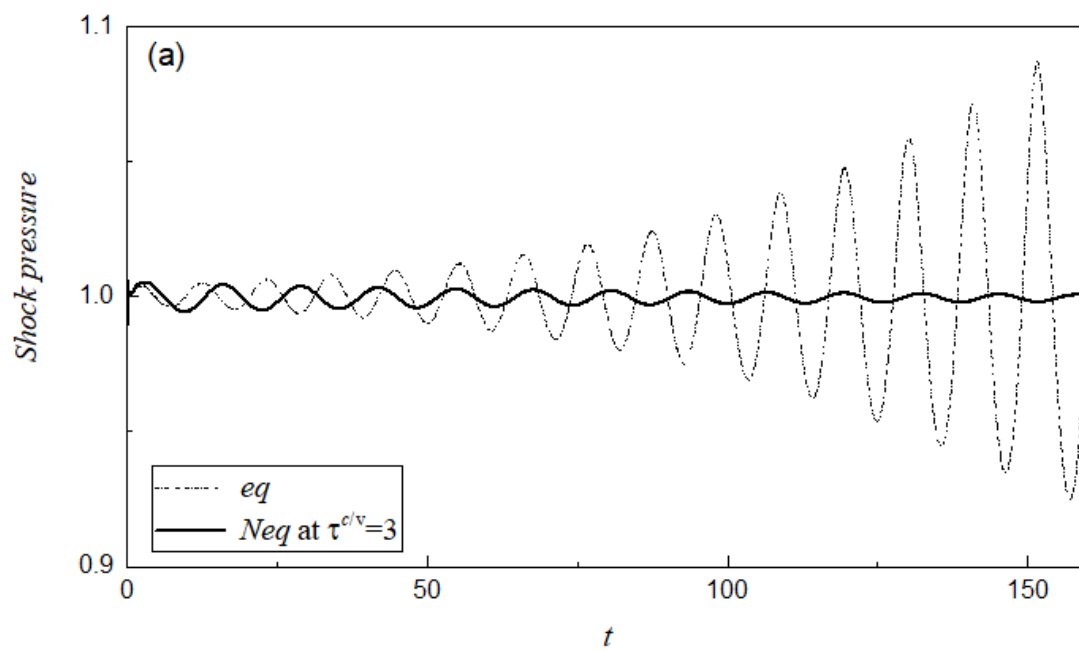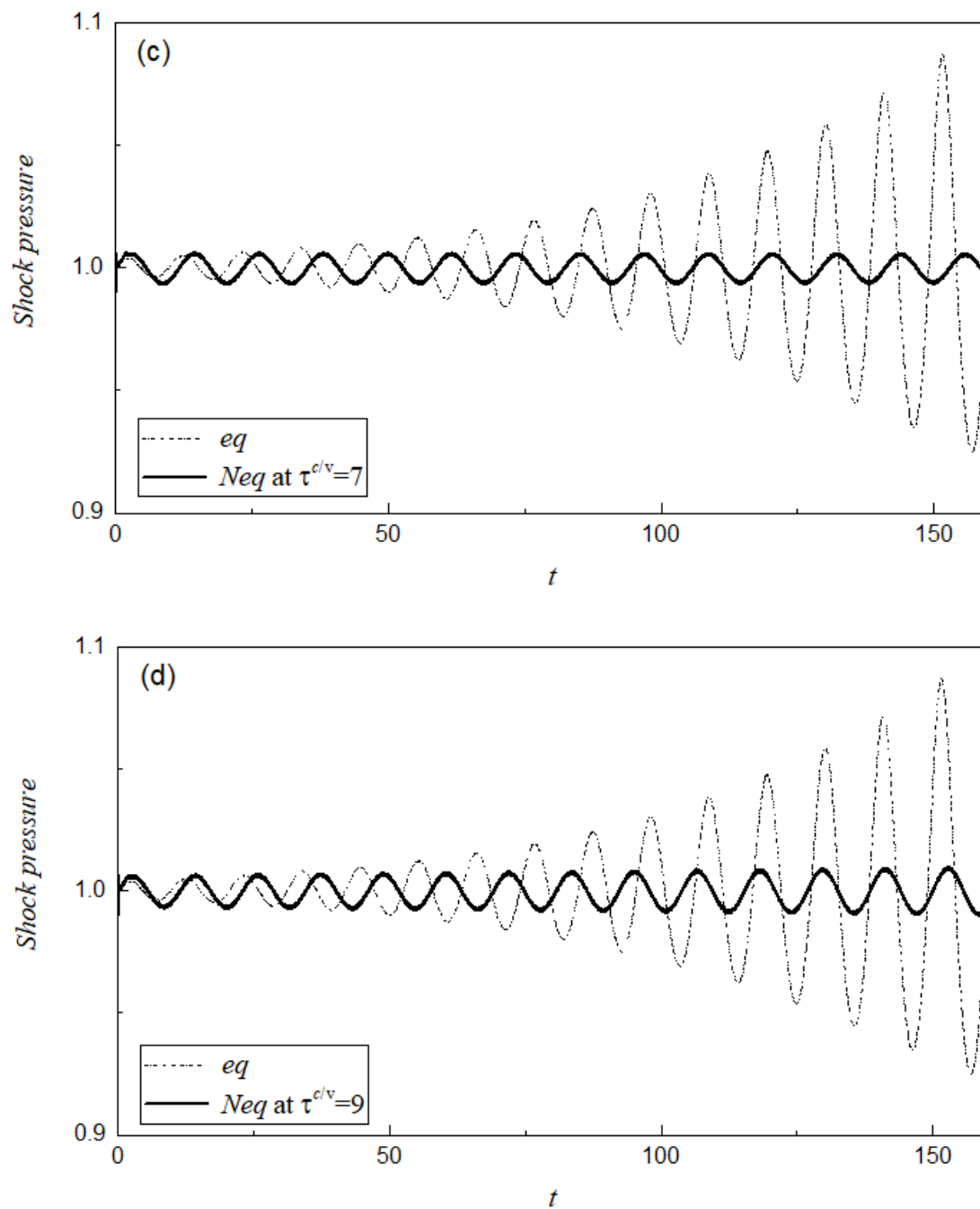
Figure 5.2 Shock pressure history at E_a=27 for thermal nonequilibrium (*Neq*) cases at a) $\tau^{c/v}$=3 (period = 12.89) b) $\tau^{c/v}$=5 (period = 12.10) c) $\tau^{c/v}$=7 (period = 11.75) and d) $\tau^{c/v}$=9 (period =11.51) with the equilibrium case (*eq*) (period = 10.66) as reference. Other fixed parameters are Q=50, γ=1.2, ϑ=20 and f=1.0.

Figure 5.3 The variations in the peak pressure difference with time for different vibrational nonequilibrium (*Neq*) cases in Figure 5.2 at $\tau^{c/v}$=3, 5, 7 and 9.

5.3 Shock pressure history of a mildly unstable overdriven detonation with different time ratio

As discussed in many literature, the increase in f can stabilize the pulsation of detonation in both direct numerical simulation and linear stability analysis. Since a detonation can be propagated in a piston-supported form in reality [9], the study of overdriven detonation is therefore common instability analysis. In addition, different modes of detonation propagation can be demonstrated through the change of f [26]. At thermal equilibrium, the detonation is always stable at f>1.731 [26], and therefore in this part, a mildly unstable case of overdriven detonation considering vibrational energy in chemical kinetics with f=1.6 at E_a=50, Q=50 and γ=1.2 is investigated by varying $\tau^{c/v}$. Figure 5.4 shows the shock pressure history with $\tau^{c/v}$=5, 10, 20 and 30. Similar to the analysis in section 5.2, a graph showing the peak difference is presented in Figure 5.5. Note that the initial damping in Figure 5.5 is due to the numerical startup error.

At this fixed f, the detonation is stabilized under low $\tau^{c/v}$, which shares similar observations as that in section 5.2. As $\tau^{c/v}$ decreases, a longer period of oscillation is resulted, in which the percentage increase can be up to 15% (at $\tau^{c/v}=5$) compared with that in the vibrational equilibrium cases. Referring to the peak difference analysis in Figure 5.5 and after several simulations, it is found that the critical $\tau^{c/v}$ below which the vibrational relaxation mechanism is significant (manifested in terms of decaying pulsation in profile) is around 21. In other words, the neutral stability limit of f can be shifted to a smaller value as $\tau^{c/v}$ decreases. Since both the increase of f (related to detonation speed) and the decrease of $\tau^{c/v}$ (related to vibrational relaxation) shows the effect of stabilization in the detonation, the competition between these two terms reduces the neutral stability limit of f accordingly.
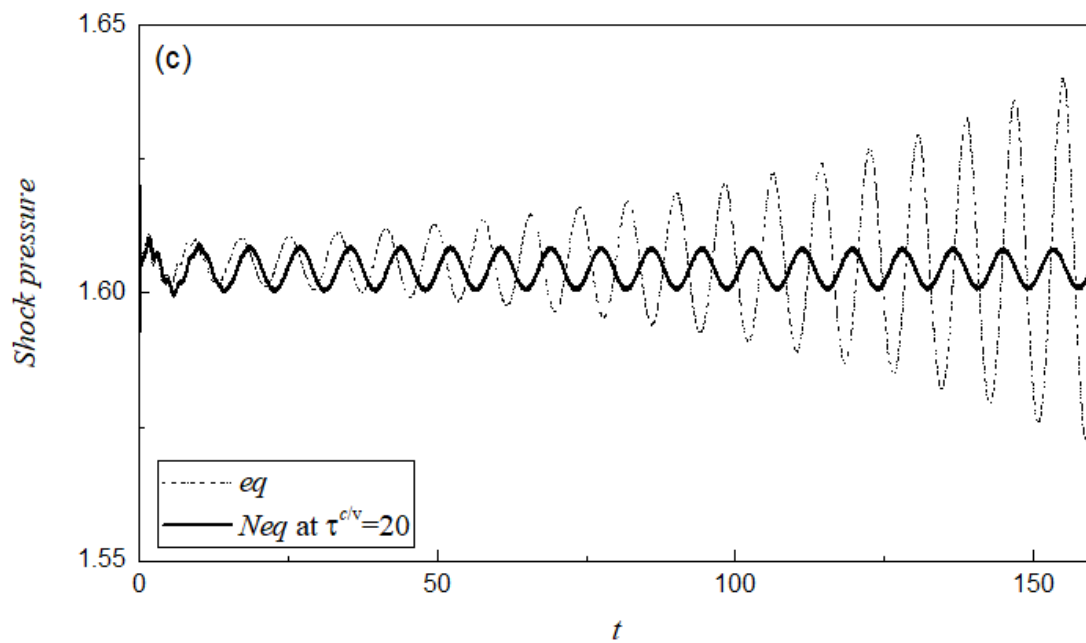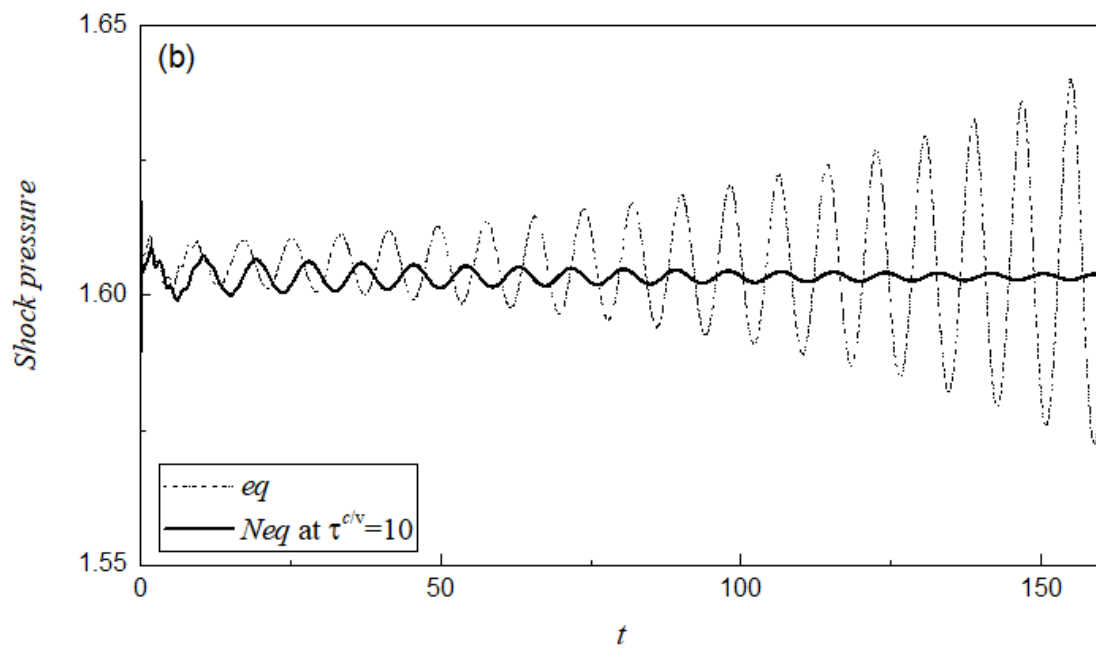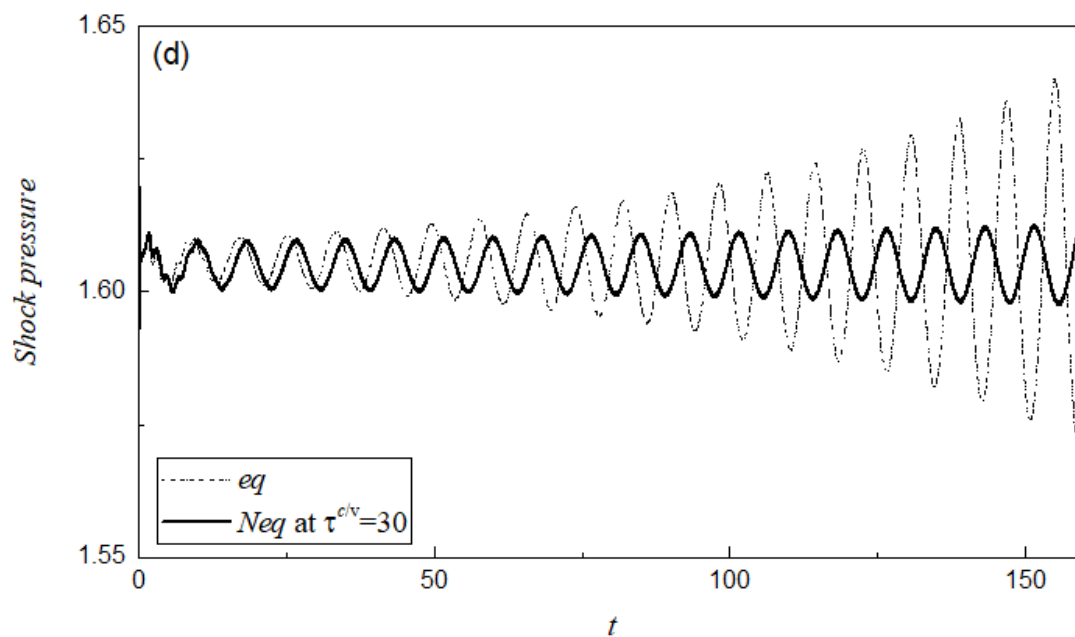
Figure 5.4 Shock pressure history at f=1.6 with vibrational nonequilibrium (*Neq*) case of a) $\tau^{c/v}$=5 (period = 9.32) b) $\tau^{c/v}$=10 (period = 8.74) c) $\tau^{c/v}$=20 (period = 8.43) and d) $\tau^{c/v}$=30 (period = 8.33) taking equilibrium case (*eq*) (period = 8.09) as reference. Other fixed parameters are Q=50, γ=1.2, ϑ=20 and E_a=50.
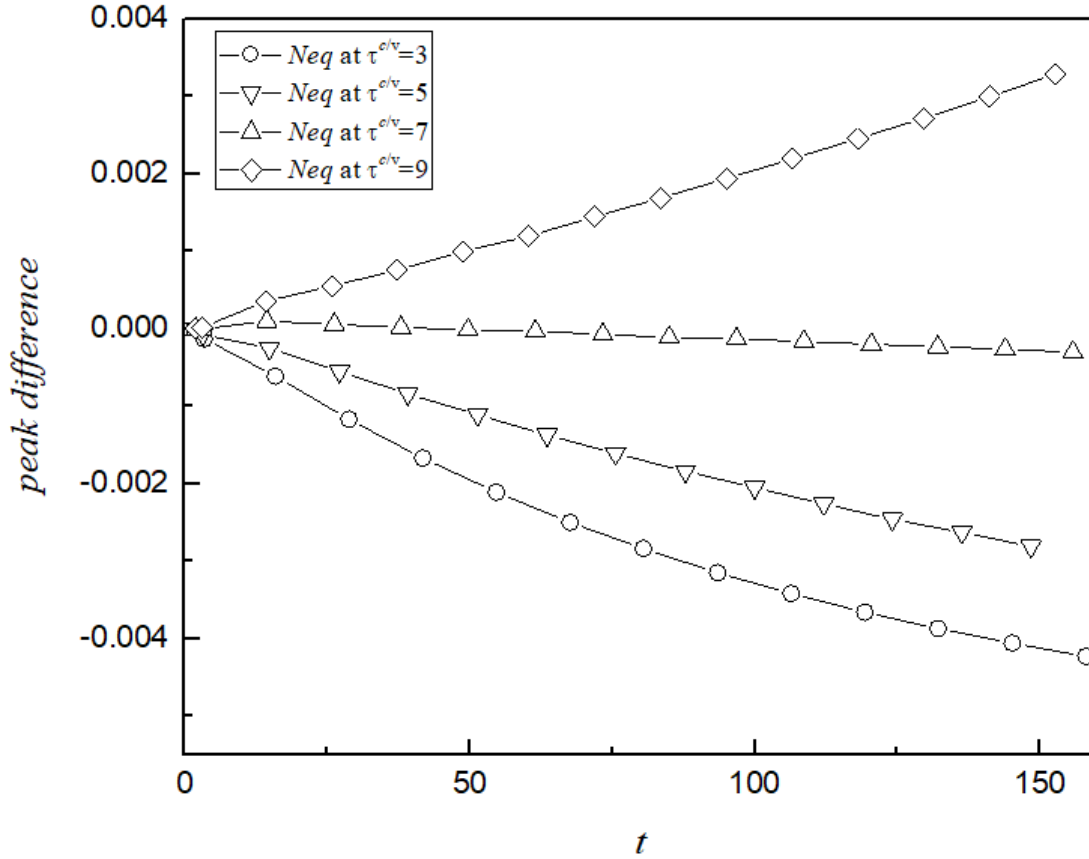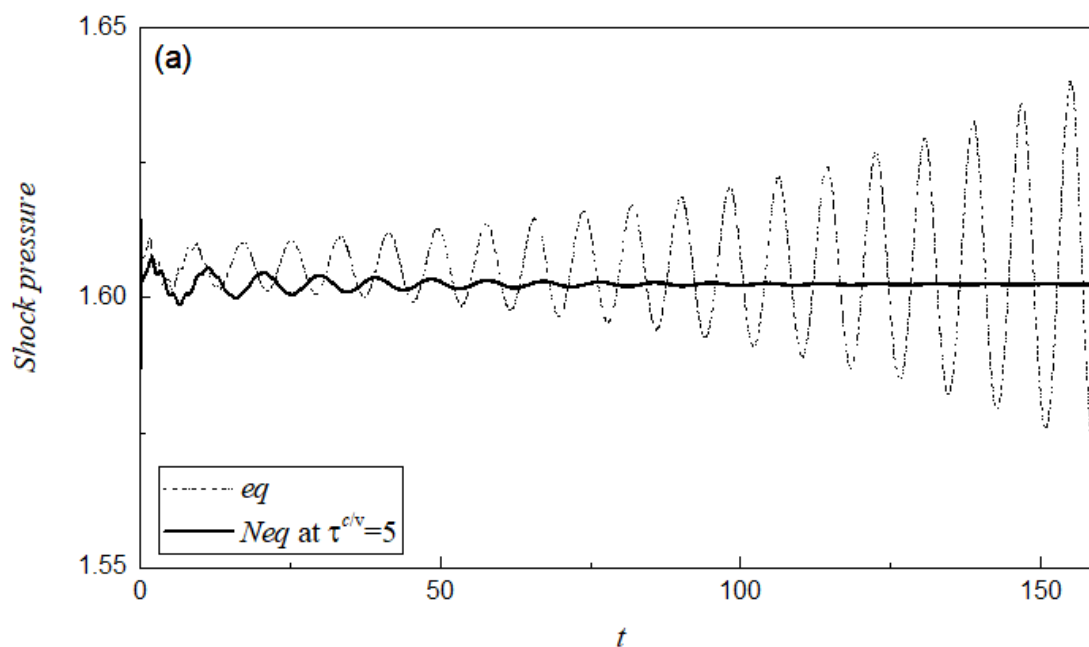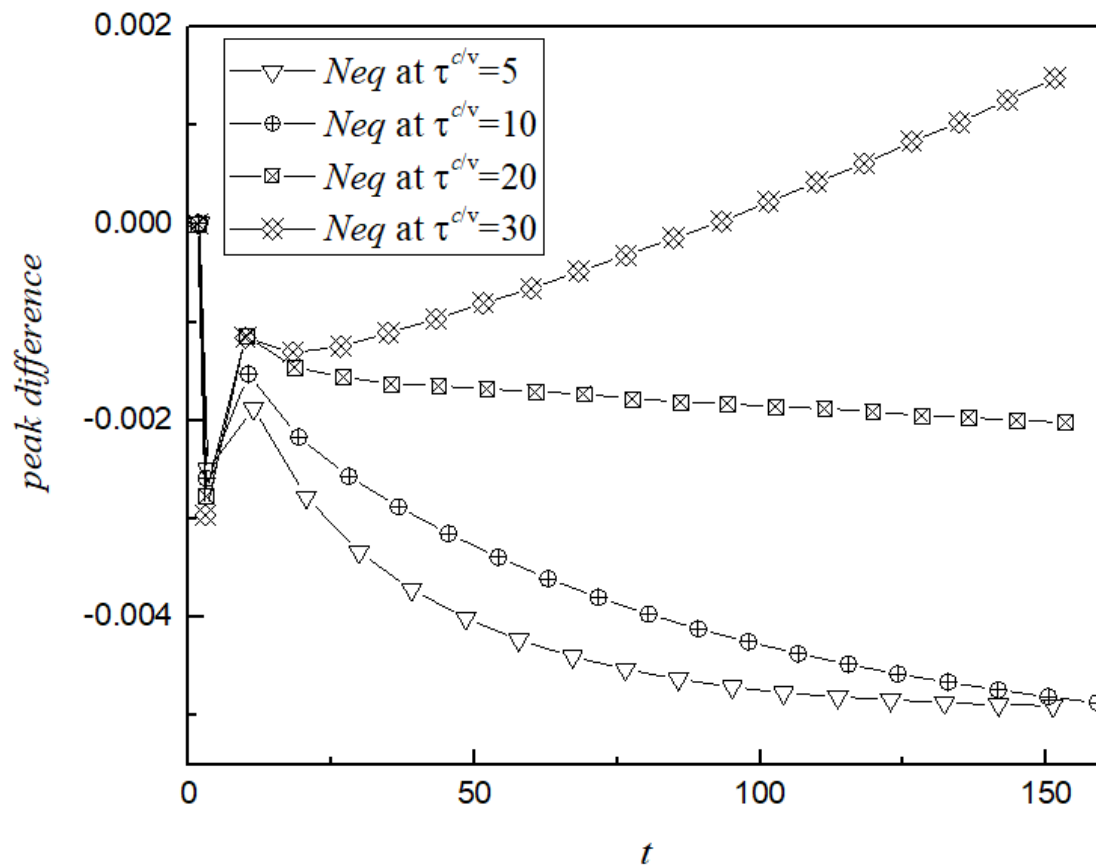
Figure 5.5 The variations in the peak pressure difference with time for different vibrational nonequilibrium (*Neq*) cases in Figure 5.4 at $\tau^{c/v}$=5, 10, 20 and 30.

5.4   Summary

In this chapter, 1D CE/SE numerical simulations of a propagating detonation were conducted by introducing the vibrational relaxation mechanism in single-step chemical kinetics related by averaged two-temperature model. A time ratio $\tau^{c/v}$ is introduced again here to describe the different degrees of vibrational nonequilibrium. To define a corresponding initial condition for the simulations, a steady-state ZND profile is constructed to include the vibrational energy terms. Under fixed parameters with γ=1.2, Q=50 and ϑ=20 the stability boundary of the activation energy under thermal equilibrium is determined to be E_a=26.47.

To elucidate whether the detonation would be stabilized or destabilized under different state of nonequilibrium/equilibrium, mildly unstable cases at equilibrium state for a CJ detonation and an overdriven detonation were simulated by varying $\tau^{c/v}$ while other parameters were fixed. For the case of CJ detonation at E_a=27, the shock pressure histories show that a smaller amplitude and longer period of oscillation are identified at smaller $\tau^{c/v}$. According to the peak difference analysis, the critical $\tau^{c/v}$ at which the vibrational relaxation mechanism becomes significant is 7.2. Referring to the chemical kinetics, the vibrational relaxation mechanism reduces the overall reaction rate attributed to the averaged two-temperature model, and thus stabilize the detonation pulsation in the profile. Higher activation energy is expected for the stabilization if the detonation is at vibrational nonequilibrium state, and a shift of neutral stability limit could be resulted as $\tau^{c/v}$ varies.

For the case of overdriven detonation at f=1.6, which is mildly unstable under the equilibrium state, the change of $\tau^{c/v}$ in the studies shows that the pulsation is stabilized as $\tau^{c/v}$ decreases, reflected by a small amplitude and a longer period of oscillation in the shock pressure history. Under these parameter settings, the critical $\tau^{c/v}$ below which the pulsation decays with time is approximately 21. Since both the change in f and $\tau^{c/v}$ are equally crucial in stabilizing the propagating detonation, the decrease in $\tau^{c/v}$ attributed to the significance of the vibrational-chemical coupling mechanism reduces the stability limit of f.

In this numerical study, the effect of the vibration-chemistry coupling effect is manifested by varying time ratio $\tau^{c/v}$. The results demonstrate that the detonation is

stabilized if vibrational relaxation is considered in the chemical kinetics, and hence a shift of neutral stability limit is expected. The actual stability limit for each studied case requires further simulations, and corresponding linear stability would be considered in the next chapter for verification.

Chapter 6　One-dimensional (1D) linear stability analysis of detonation involving vibrational-chemical coupling mechanism

In Chapter 5, a shift of neutral stability boundary with different time ratio $\tau^{c/v}$ is reported in detonation with vibration-chemistry coupling using direct numerical simulation (DNS). To quantitatively address the unstable mode in the stability spectra, linear stability analysis (LSA) is adopted here with the same chemical kinetics.

The content of this chapter would be divided into two parts mainly, with the LSA of idealization detonation being introduced first, followed by the LSA of detonation involving vibrational-chemical coupling kinetics. First, the governing equations of the detonation model are presented with respect to the post-shock state, unlike the formulation in previous chapters which are normalized with the pre-shock state (or initial reactant state). The benefit of using a post-shock state over the pre-shock state for scaling can provide a better description of the detonation structure and the stability behaviour, which has been illustrated in Short & Stewart's work [16]. Then a steady-state profile is considered with these equations. For the idealized detonation, LSA is formulated accordingly and is compared with the normal mode result in literature for validation. Second, LSA for detonation with the vibration-chemistry coupling mechanism is constructed. Normal mode linear stability spectra at different states of nonequilibrium denoted by $\tau^{c/v}$ are presented by varying three parameters in the model: the activation energy in simplified chemistry, the degree of overdrive, and the characteristic vibrational temperature in the vibrational relaxation model. For each state, the corresponding unstable mode and stability limit are identified. Finally, the governing equations are solved numerically so that the results from DNS and that from LSA are compared. Justification of using both analytical and numerical approaches to study detonation stability at vibrational nonequilibrium are provided, and a critical $\tau^{c/v}$ under which vibrational nonequilibrium becomes significant is suggested.

6.1　Governing equations

Following the work by Lee & Stewart [15] and Short & Stewart [16], all the parameters involved in the present normal mode linear stability analysis are nondimensionalized with the post-shock state, instead of the pre-shock state as discussed in previous

chapters. To avoid confusion, some of the important equations are presented again here with different reference frames or dimensions, such that the analysis would be favourable.

For a reactive flow propagates inside a channel, one-dimensional reactive Euler equations in the laboratory frame of reference (superscript l) can be formulated to describe the process: (nondimensionalized with the post-shock state)

$$\frac{Dv}{Dt} - v\nabla \cdot u^l = 0, \quad \frac{Du^l}{Dt} + v\nabla \cdot p = 0, \quad \frac{De}{Dt} + p\frac{Dv}{Dt} = 0 \tag{6.1}$$

The material derivative is defined as

$$\frac{D}{Dt} = \frac{\partial}{\partial t^l} + u^l \frac{\partial}{\partial x^l},$$

which is one-dimensional with a single velocity component u^l only. The corresponding internal energy equation at thermal equilibrium can be expressed as:

$$e = \frac{pv}{\gamma - 1} - \lambda\varrho, \quad T = pv. \tag{6.2}$$

If the flow is assumed to be under thermal nonequilibrium, the energy equations with vibrational energy included are redefined as

$$e = \frac{pv}{\gamma - 1} - \lambda\varrho + \varepsilon, \quad T_{\text{tr}} = pv, \tag{6.3}$$

$$\varepsilon = \frac{\eta}{\exp(\eta/T_v) - 1} \tag{6.4}$$

where ϱ, η, and ε denote the heat release, characteristic vibrational temperature, and specific vibrational energy, respectively. To describe the progress variable λ, single-step Arrhenius equations is applied as below,

$$\frac{D\lambda}{Dt} = r = K(1 - \lambda)\exp\left(-\frac{\phi}{T_a}\right), \tag{6.5}$$

where ϕ is the activation energy and K is the pre-exponential factor for the reaction.

For thermal equilibrium assumption, $T_a = T$ is defined (analogous to Eq. (6.2)), while for thermal nonequilibrium assumption, T_a is modelled by Park's two-temperature model, i.e., $T_a = \sqrt{T_{tr}T_v}$ analogous to Eq. (2.29).

For the energy transfer rate r_ε between translational-rotational mode and vibrational mode, the Landau-Teller model is utilized as follows:

$$\frac{D\varepsilon}{Dt} = r_\varepsilon = \frac{\varepsilon^{eq} - \varepsilon}{\tau_v} \tag{6.6}$$

ε^{eq} is the equilibrium vibrational energy which can be found by replacing T_v with T_{tr} in Eq. (6.4). As mentioned in section 2.2.2, a time ratio $\tau^{c/v}$ is introduced to determine τ_v by a fixed chemical time scale τ_c. With the known ε and T_{tr}, the corresponding T_v in each time step can be iterated by Newton's method.

As stated in the beginning, the density, pressure, temperature, and velocity in the above equations are nondimensionalized with respect to the corresponding dimensional thermodynamic properties and sound speed ($\bar{c}_s$) at the post-shock state (subscript as s). For the length scale, the steady half-reaction length $\mathcal{L}_{1/2}$ is chosen for nondimensionalization which is defined as the distance from the shock to the position where half of the reactant is consumed under the equilibrium condition, and for time, $\mathcal{L}_{1/2}/\bar{c}_s$. The scaled activation energy ϕ, heat release ϱ, and characteristic vibrational temperature η are defined as

$$\phi = \frac{\gamma \bar{E}_a}{\bar{c}_s^2}, \quad \varrho = \frac{\gamma \bar{Q}}{\bar{c}_s^2}, \quad \eta = \frac{\bar{\vartheta}}{\bar{T}_s} \tag{6.7}$$

for dimensional activation energy $\bar{E}_a$, heat release $\bar{Q}$, and characteristic vibrational temperature $\bar{\vartheta}$.

If these parameters are scaled with the pre-shock state (or initial reactant state), the expression would be defined as

$$E_a = \frac{\gamma \bar{E}_a}{\bar{c}_0^2}, \quad Q = \frac{\gamma \bar{Q}}{\bar{c}_0^2}, \quad \vartheta = \frac{\bar{\vartheta}}{\bar{T}_0}, \tag{6.8}$$

Substituting the above scales (named "Erpenbeck scale" in literature) into Eq. (6.2) to (6.6) is analogous to the formulations discussed in section 2.1 - 2.3.

6.2 Steady-state profile

A steady one-dimensional solution can be obtained through the Rankine-Hugoniot analysis of the reactive flow model discussed in section 6.1. For easy demonstration, a superscript * is added to specify the steady variables. According to the analysis by Erpenbeck [11] and He et al. [43], the corresponding Rayleigh line and the Hugoniot curve can be derived by integrating Eq. (6.1) at the steady-state. Assuming the steady detonation propagates from right to left at a speed of D_s^*, which is nondimensionalized with dimensional post-shock sound speed $\bar{c}_s$, the flow path at the shock-attached coordinate system can be formulated as $X = x^l + D_s^* t^l$. The flow Mach number M_s^* right behind the shock can then be described as

$$M_s^{*2} = \frac{(\gamma - 1)M^{*2} + 2}{2\gamma M^{*2} - (\gamma - 1)} \tag{6.9}$$

where M^* is the detonation Mach number nondimensionalized with respect to the dimensional pre-shock sound speed $\bar{c}_0$.

The corresponding steady variables right behind the shock are given as the shock boundary conditions as below:

$$v^* = p^* = T^* = 1, \quad u^* = M_s^*, \quad \lambda^* = 0, \quad \varepsilon^* = 0 \tag{6.10}$$

Notably, ε^* is assumed to be zero such that the vibration energy mode of reactants is activated right behind the shock. With these dimensionless variables provided, the Rankine-Hugoniot relation is rewritten in terms of v^* and p^* across the reaction zone and is expressed below (normalized by the post-state state properties):

$$v^* = \frac{\gamma M_s^{*2} + 1}{M_s^{*2}(\gamma + 1)} [1 \mp w\xi(\lambda^*, \varepsilon^*)], \tag{6.11}$$

$$p^* = \frac{\gamma M_s^{*2} + 1}{\gamma + 1} [1 \pm \gamma w\xi(\lambda^*, \varepsilon^*)], \tag{6.12}$$

$$\xi(\lambda^*, \varepsilon^*) = \sqrt{1 + \frac{\varepsilon^* - \lambda^* \varrho}{\Omega}}, \Omega = \frac{\gamma(1 - M_s^{*2})^2}{2M_s^{*2}(\gamma^2 - 1)}, w = \frac{1 - M_s^{*2}}{\gamma M_s^{*2} + 1} \tag{6.13}$$

The change in λ^* and ε^* at the corresponding shock position can be evaluated by Eqs. (6.5) and (6.6), respectively. Noted that the expressions in Eqs. (6.11) - (6.13) is similar

to that in Eqs. (2.42) - (2.44) but in different normalized form, i.e., in terms of M^* if the expression is normalized with respect to the pre-shock state.

Degree of overdrive f is utilized to specify an overdriven detonation and the detonation velocity D^* is then determined by the following relations:

$$f = \left(\frac{D^*}{D_{CJ}^*}\right)^2 \tag{6.14}$$

where D_{CJ}^* can be evaluated from Eq. (2.46). The newly established ZND profile with vibrational energy included is fully determined.

Figure 6.1 shows the changes of variables across the steady detonation wave with $Q=50$ (or $\varrho=10.39$), $E_a=50$ (or $\phi=10.39$), $\gamma=1.2$, $\vartheta=20$ (or $\eta=4.16$) and $f=1$. The thermal (vibrational) equilibrium case (*eq*) and nonequilibrium cases (*Neq*) at $\tau^{c/v}=3$, 5 and 7 are selected for demonstration. Since the equilibrium cases (*eq*) is served as a reference with no vibrational relaxation process involved, the two temperature T_{tr}^* and T_v^* are identical across the profile. Recalling the definition of $\tau^{c/v} \equiv \tau_c/\tau_v$, a small $\tau^{c/v}$ indicates that the detonation is under significant vibrational nonequilibrium and vice versa, which can be shown by λ^* also in terms of the slowest chemical reaction rate at $\tau^{c/v}=3$ compared with the other cases. Notably, the asymptotic solutions at the downstream state and the upstream state remain the same for all $\tau^{c/v}$, as the change of it only alters the steady detonation wave structure within the reaction zone but not the initial or end-state properties.
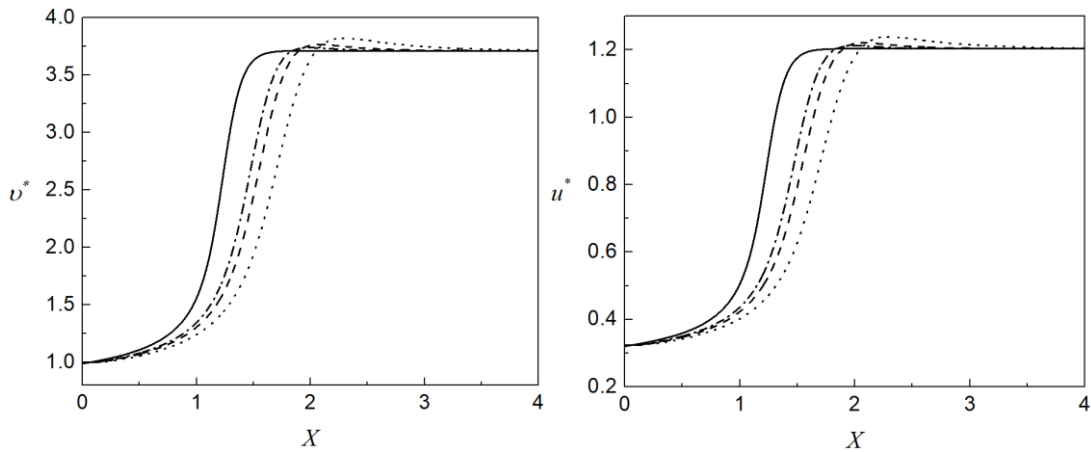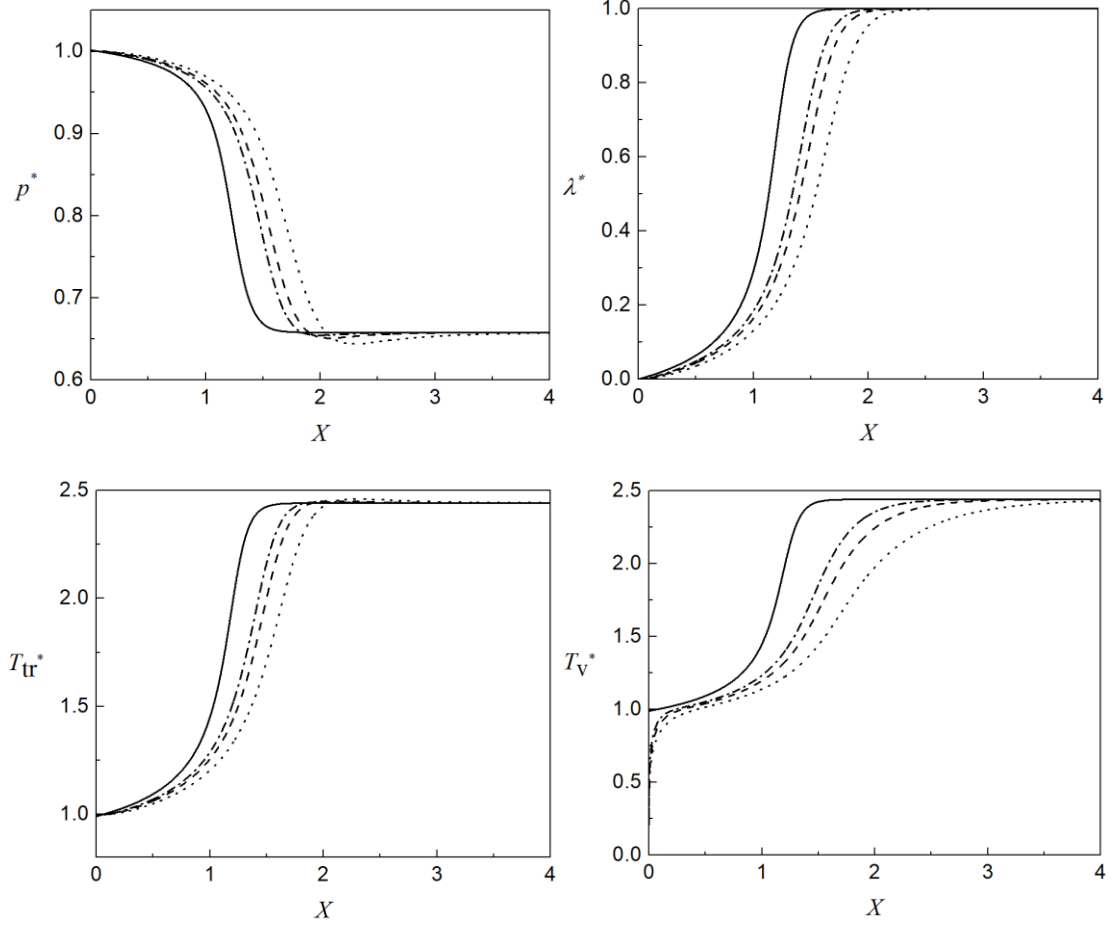
Figure 6.1 Steady ZND profiles for $Q=50$, $E_a=50$, $\gamma=1.2$, $\vartheta=20$ and $f=1$ for the vibrational equilibrium case (*eq*) (solid) and nonequilibrium cases (*Neq*) with $\tau^{c/v}=3$ (dotted), $\tau^{c/v}=5$ (dashed) and $\tau^{c/v}=7$ (dot-dash).

6.3   1D linear stability analysis of idealized detonation

Following the analysis in the work of Short & Stewart, a normal mode linear stability analysis of the steady detonation wave structure can be established by introducing one-dimensional perturbations in the shock-attached coordinated system as expressed below:

$$x = x^l + D_s^* t^l - \psi(t) \tag{6.15}$$

where $\psi(t)$ represents the perturbation to the shock. Perturbations to the steady detonation wave are then sought in the following forms

$$z = z^*(x) + z'(x) \exp(\alpha t), \quad \psi = \psi' \exp(\alpha t) \tag{6.16}$$

where

$$z = [v, u, p, \lambda]^{\mathrm{T}} \tag{6.17}$$

The real part of α, i.e., $\text{Re}(\alpha)$, is the growth rate of the disturbance whereas that of the imaginary part, i.e., $\text{Im}(\alpha)$, is the disturbance frequency. To construct the linearized perturbation equations for the complex perturbation eigenfunction $z'(x)$, Eq. (6.15)(6.1) and (6.16) is substituted into Eqs. (6.1) – (6.6) and is written in the following form

$$A^*\zeta_x + (\alpha \cdot I + C^*)\zeta - \alpha z_x^* = 0, \tag{6.18}$$
$$\zeta = z'/\psi' \tag{6.19}$$

I is the identity matrix and the matrices A^* and C^* are expressed as

$$A^* = \begin{bmatrix} u & -v & 0 & 0 \\ 0 & u & v/\gamma & 0 \\ 0 & \gamma p & u & 0 \\ 0 & 0 & 0 & u \end{bmatrix}^*, \tag{6.20}$$

$$C^* = \begin{bmatrix} -u_x & v_x & 0 & 0 \\ p_x/\gamma & u_x & 0 & 0 \\ C_{31} & p_x & C_{33} & C_{34} \\ -r_v & \lambda_x & -r_p & -r_\lambda \end{bmatrix}^*, \tag{6.21}$$

where

$$C_{31} = \frac{(\gamma - 1)\varrho}{v}\left[\frac{r}{v} - r_v\right], \tag{6.22}$$

$$C_{33} = \gamma u_x - \frac{(\gamma - 1)}{v}\varrho r_p,$$

$$C_{34} = -\frac{(\gamma - 1)}{v}\varrho r_\lambda,$$

The derivatives of $r(v, p, \lambda)$ (i.e., Eq. (6.5)) in C^* are

$$r_v = \frac{r\phi}{vT}, \quad r_p = \frac{r\phi}{pT}, \quad r_\lambda = -K\exp\left(-\frac{\phi}{T}\right) \tag{6.23}$$

From the linearization of the Rankine-Hugoniot shock relation, the perturbation shock condition is formulated as follows:

$$v' = \frac{4\alpha}{(\gamma + 1)M^{*2}M_s^*}\psi', \quad u' = \frac{2(1 + M^{*2})\alpha}{(\gamma + 1)M^{*2}}\psi', \tag{6.24}$$

$$p' = -\frac{4\gamma M_s^* \alpha}{\gamma + 1} \psi', \quad \lambda' = 0$$

which can be expressed in terms of ζ (Eq. (6.19))

$$\zeta(0) = \left[\frac{4\alpha}{(\gamma + 1)M^{*2}M_s^*}, \frac{2(1 + M^{*2})\alpha}{(\gamma + 1)M^{*2}}, -\frac{4\gamma M_s^* \alpha}{\gamma + 1}, 0 \right]^T$$

(6.25)

Lastly, an acoustic radiation condition [66] is applied at the end of the reaction zone such that no acoustic wave propagates upstream from infinity [16, 67] and is expressed in the form of

$$u' - \frac{v_b^*}{\gamma c_b^*} p' = 0$$

(6.26)

which can be expressed by the second and third terms of ζ

$$\zeta_2(\infty) - \frac{v_b^*}{\gamma c_b^*} \zeta_3(\infty) = 0$$

(6.27)

where v_b^* and c_b^* are the unperturbed specific volume and the isentropic sound speed in the burned reactant. This condition is applied when λ^* approaches to 1 at $x = \infty$, where the detonation should reach the equilibrium state.

To solve the linearized perturbation equations in Eq. (6.18) and determine the complex eigenvalues α and eigenfunction $z'(x)$, a two-point boundary value solution technique is utilized based on the numerical shooting method described in the work of Lee & Stewart [15]. The shooting starts from an initial guess of α, with the given initial condition in Eq. (6.25), Eq. (6.18) is integrated from the shock position towards the end of the zone denoting the thermal equilibrium point. A two-variable Newton-Raphson iteration is implemented such that α is iterated until the acoustic radiation condition in Eq. (6.26) is satisfied. A tolerance of 10^{-7} in real eigenfunctions at the boundary is allowed in the iteration.

6.3.1 Comparison of normal mode results in different literatures with the present work

Per discussion in the work of Kabanov & Kasimov (2018), the normal mode results obtained from LSA can be in different values depending on the different scaling, although they share the same physical interpretation. In this part, a comparison of the unstable spectra for fundamental modes between the present work and the literature is presented for parameters $\gamma=1.2$, $Q=50$, and $f=1$ under the thermal equilibrium state without considering vibrational energy (analogous to the formulation in section 6.3).

Table 6.1 Comparison of the unstable spectra for the fundamental modes between the present work and the normal mode results summarized in Erpenbeck scales at $\gamma=1.2$, $Q=50$ and $f=1$. The corresponding eigenvalues α consist of the real part (i.e., $\mathrm{Re}(\alpha)$) and the imaginary part (i.e., $\mathrm{Im}(\alpha)$).

E_a	Present work based on Short & Stewart scales [16]		Results of Kabanov & Kasimov [68] in Erpenbeck scales	
	$\mathrm{Re}(\alpha)$	$\mathrm{Im}(\alpha)$	$\mathrm{Re}(\alpha)$	$\mathrm{Im}(\alpha)$
50	0.726	0.000	1.743	0.000
	0.039	0.000	0.084	0.000
26	0.016	0.218	0.037	0.522
25.26	0.000	0.220	0.000	0.530
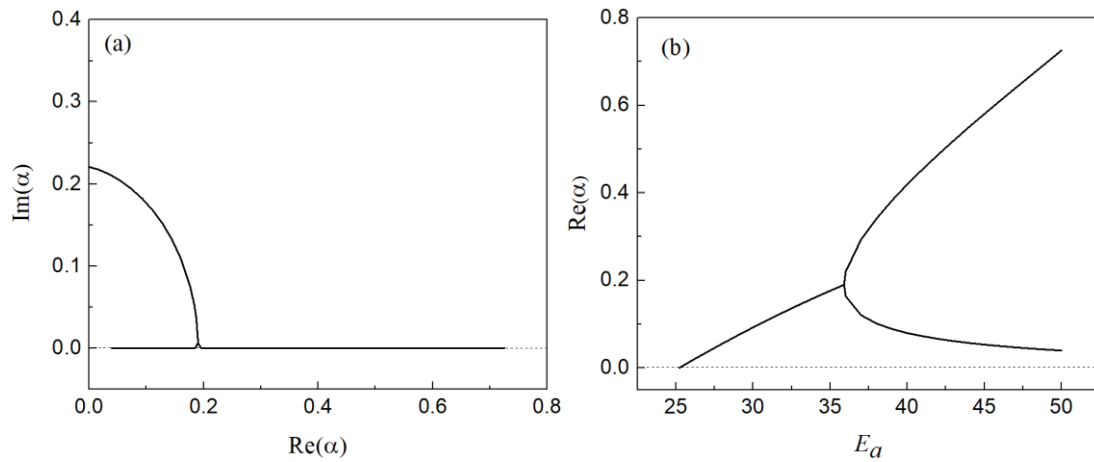
Figure 6.2 Stability spectrum showing (a) $\mathrm{Im}(\alpha)$ vs $\mathrm{Re}(\alpha)$ and (b) $\mathrm{Re}(\alpha)$ vs E_a for the fundamental mode at $\gamma=1.2$, $Q=50$ and $f=1$ under thermal equilibrium.

Table 6.1 shows the comparison of the normal mode results at the selected E_a range and Figure 6.2 shows the corresponding unstable spectrum. Referring to the study by Sharpe [17] and also the unstable spectrum determined in the present work (Figure 6.2),

the growth rate of the disturbance ($\text{Re}(\alpha)$) increases with E_a from the neutral stability limit, while its frequency decreases until a bifurcation point is reached. This point is shown to be at $E_a \approx 36$ (estimated to be E_a=35.91 in present work), in which a further increase of E_a would lead to the splitting of one oscillatory eigenmode into two nonoscillatory eigenmode, one of which would go to zero asymptotically whereas the other one would increase with E_a. The neutral stability limit below which the growth rate become undeterminable (in other words, the detonation is stable) is at E_a=25.22 in the present work, which is close with the estimation in literature, i.e., E_a=25.26. By comparing the eigenvalues obtained in the two scales in Table 6.1, the conversion factor from the present work to the Erpenbeck scale is approximately 2.4. Based on the analysis from Kabanov & Kasimov [68], the conversion factor can be calculated from the ratio of the nondimensional pre-exponential factor K in both scales. Following their approaches, the numerical value of this factor is deduced to be 2.403, which fits with the prediction from the corresponding eigenvalues presented in the table. Note that the data point at E_a=50 obtained in the present work has been compared graphically with the work of Short & Stewart on the two-dimensional (2D) LSA to ensure that the normal mode results are validated.

As mentioned in the above section, the difference of the scales in the present work with the Erpenbeck scale is that the latter one is normalized with respect to the pre-shock state properties. Although the use of the post-shock state for nondimensionalization is better in describing the detonation wave structure, the eigenvalues obtained in the Erpenbeck scales near the stability boundary can closely predict the corresponding disturbance frequency. For example, based on the $\text{Im}(\alpha)$ obtained at E_a=25.26 in LSA, the period of oscillation is expected to be $2\pi/0.53 = 11.855$, and this is fairly close to the averaged period of oscillation determined from the same case using DNS, i.e., 11.86. In this context, the analysis of the normal mode results using Erpenbeck scales is also considered in the following discussion as necessary.

6.4   1D linear stability analysis of detonation with vibrational relaxation

Following the analysis in section 6.3, a normal mode linear stability analysis of detonation with vibrational relaxation is constructed by the same coordinated system presented in Eq. (6.15) in the first step, but the perturbations to the steady detonation structure are sought with an extra equation denoted the vibrational relaxation in terms of ε as follows:

One-dimensional (1D) linear stability analysis of detonation involving vibrational-chemical coupling mechanism

$$z = z^*(x) + z'(x)\exp(\alpha t), \quad \psi = \psi'\exp(\alpha t) \tag{6.28}$$

where

$$z = [v, u, p, \lambda, \varepsilon]^\mathrm{T} \tag{6.29}$$

The corresponding linearized perturbation equations share the same form discussed in Eq. (6.18) and (6.19), but the matrices involved have been changed from 4 by 4 to 5 by 5 matrix due to the presence of vibrational relaxation model, i.e., Eq. (6.6). While $\boldsymbol{I}$ is still the identity matrix but in 5 by 5 instead, the matrices $\boldsymbol{A}^*$ and $\boldsymbol{C}^*$ are modified as follows:

$$\boldsymbol{A}^* = \begin{bmatrix} u & -v & 0 & 0 & 0 \\ 0 & u & v/\gamma & 0 & 0 \\ 0 & \gamma p & u & 0 & 0 \\ 0 & 0 & 0 & u & 0 \\ 0 & 0 & 0 & 0 & u \end{bmatrix}^*, \tag{6.30}$$

$$\boldsymbol{C}^* = \begin{bmatrix} -u_x & v_x & 0 & 0 & 0 \\ p_x/\gamma & u_x & 0 & 0 & 0 \\ C_{31} & p_x & C_{33} & C_{34} & C_{35} \\ -r_v & \lambda_x & -r_p & -r_\lambda & -r_\varepsilon \\ -r_{\varepsilon,v} & \varepsilon_x & -r_{\varepsilon,p} & 0 & -r_{\varepsilon,\varepsilon} \end{bmatrix}^* \tag{6.31}$$

where

$$C_{31} = \frac{(\gamma - 1)}{v}\left[\frac{\varrho r - r_\varepsilon}{v} - (\varrho r_v - r_{\varepsilon,v})\right], \tag{6.32}$$

$$C_{33} = \gamma u_x - \frac{(\gamma - 1)}{v}(\varrho r_p - r_{\varepsilon,p}),$$

$$C_{34} = -\frac{(\gamma - 1)}{v}\varrho r_\lambda,$$

$$C_{35} = \frac{(\gamma - 1)}{v}(r_{\varepsilon,\varepsilon} - \varrho r_\varepsilon)$$

The derivatives of $r(v, p, \lambda, \varepsilon)$ (i.e., Eq. (6.5)) in $\boldsymbol{C}^*$ are

$$r_v = \frac{r\phi}{2vT_a}, \quad r_p = \frac{r\phi}{2pT_a}, \tag{6.33}$$

$$r_\lambda = -K\exp\left(-\frac{\phi}{T_a}\right), \quad r_\varepsilon = \frac{\partial r}{\partial T_v} \cdot \frac{\partial T_v}{\partial \varepsilon},$$

where

$$\frac{\partial r}{\partial T_v} = \frac{r\phi}{2T_vT_a}, \quad \frac{\partial T_v}{\partial \varepsilon} = \frac{T_v^2[\exp(\vartheta/T_v) - 1]^2}{\vartheta^2\exp(\vartheta/T_v)}$$

74

One-dimensional (1D) linear stability analysis of detonation involving vibrational-chemical coupling mechanism

The derivatives of $r_\varepsilon(v,\ p,\ \varepsilon)$ (i.e., Eq. (6.6)) in $\boldsymbol{C}^*$ are

$$r_{\varepsilon,v} = \frac{\varpi}{\tau_v v}, \quad r_{\varepsilon,p} = \frac{\varpi}{\tau_v p}, \quad r_{\varepsilon,\varepsilon} = -\frac{1}{\tau_v} \tag{6.34}$$

$$\varpi = \frac{\vartheta^2}{pv} \frac{\exp(\vartheta/pv)}{[\exp(\vartheta/pv) - 1]^2}$$

For the perturbation shock condition, ε' is assumed to be zero and thus the expression for this condition in terms of ζ can be written as

$$\zeta(0) = \left[\frac{4\alpha}{(\gamma+1)M^{*2}M_s^*}, \frac{2(1+M^{*2})\alpha}{(\gamma+1)M^{*2}}, -\frac{4\gamma M_s^* \alpha}{\gamma+1}, 0, 0 \right]^{\mathrm{T}} \tag{6.35}$$

Again an acoustic radiation condition is considered at the boundary and the form is the same as that presented in Eq. (6.26) and (6.27), in which only ζ_2 (i.e., u'/ψ') and ζ_3 (i.e., p'/ψ') are involved. The numerical shooting method of solving the linearized perturbation equations would be the same as that discussed in section 6.3.

6.4.1 Stability spectrum by varying activation energy at different time ratio
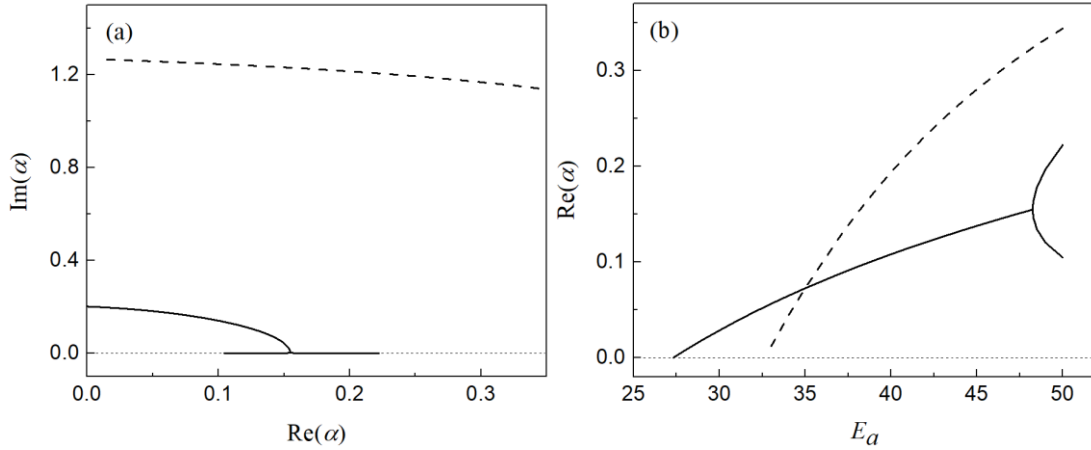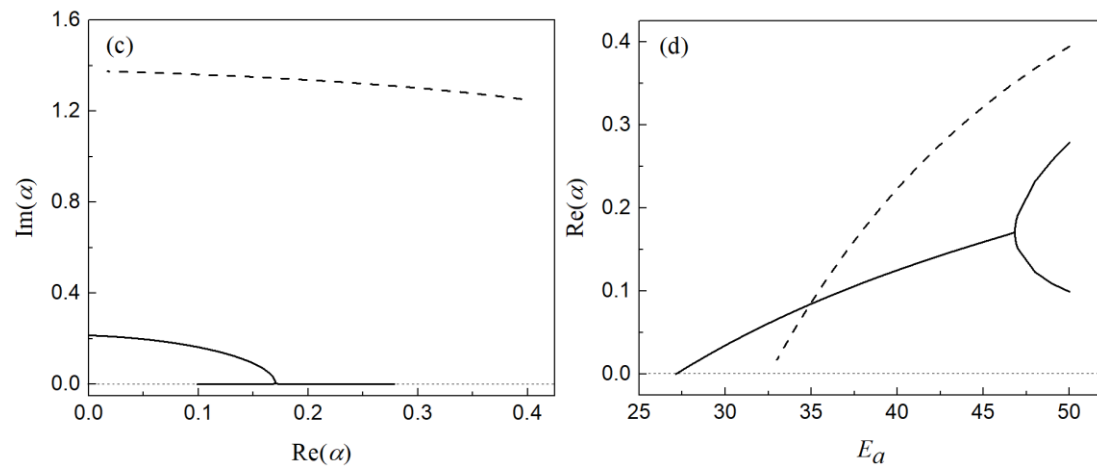
Figure 6.3 Stability spectrum showing (a) $Im(\alpha)$ vs $Re(\alpha)$ and (b) $Re(\alpha)$ vs E_a for $\tau^{c/v}=3$ and (c) $Im(\alpha)$ vs $Re(\alpha)$ and (d) $Re(\alpha)$ vs E_a for $\tau^{c/v}=5$. The solid curve represents the fundamental mode, and the dashed curve represents the first overtone. $\gamma=1.2$, $Q=50$, $\vartheta=20$ and $f=1$.
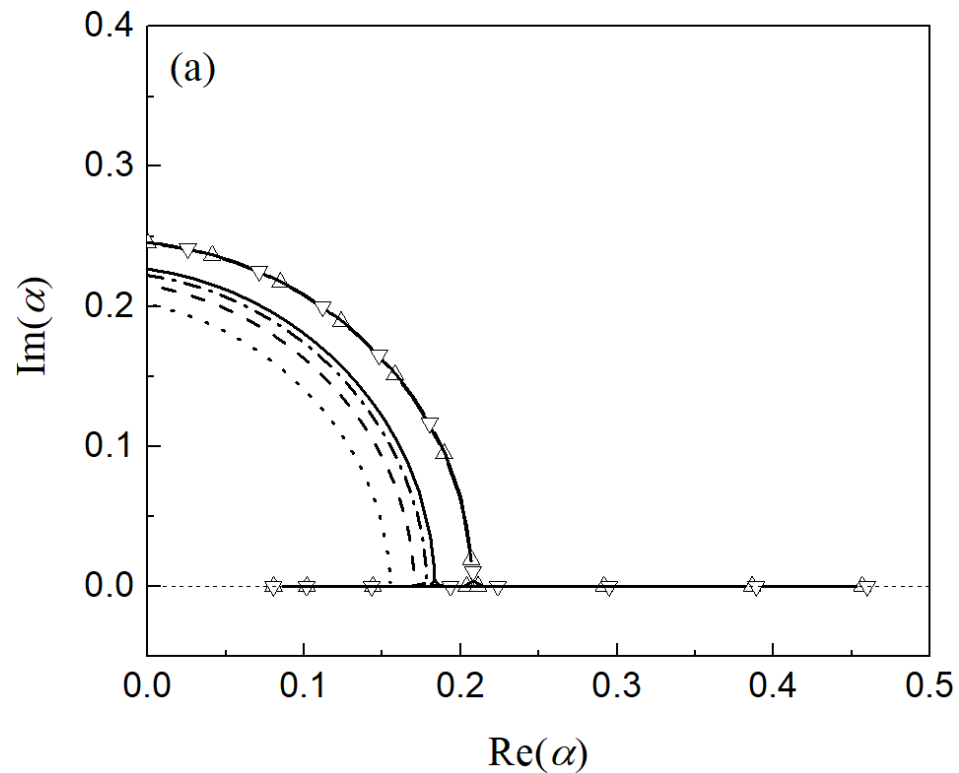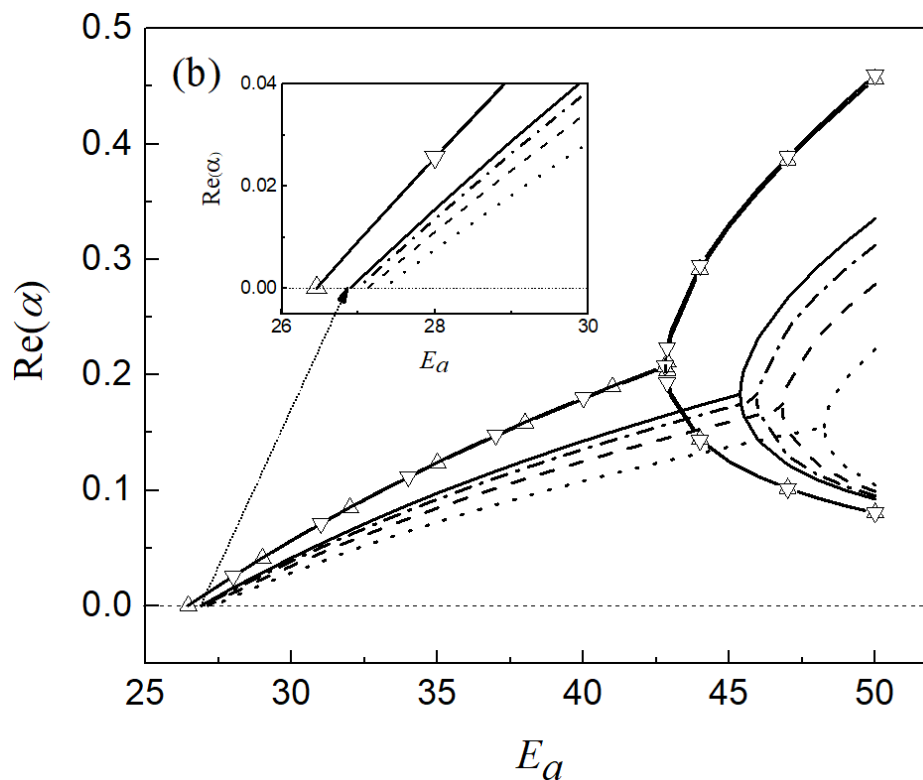
Figure 6.4 Stability spectrum showing (a) Im(α) vs Re(α) and (b) Re(α) vs E_a with the fundamental mode only at $\tau^{c/v}$=3 (dotted), $\tau^{c/v}$=5 (dashed), $\tau^{c/v}$=7 (dot-dash), $\tau^{c/v}$=9 (solid), $\tau^{c/v}$=275 (solid-Δ) and $\tau^{c/v}$=700 (solid-∇). γ=1.2, Q=50, ϑ=20 and f=1.

Table 6.2 Summary of the neutral stability limit E_a for fundamental mode at different $\tau^{c/v}$ by LSA.

τ^{α}	Neutral stability limit E_a
3	27.32
5	27.12
7	26.98
9	26.88
55	26.52
105	26.48
205	26.46
274	26.46
275	26.45
400	26.45
700	26.45

Figure 6.3 shows the relationship between the frequency and the growth rate of the

disturbance fundamental mode and first overtone in terms of $\text{Im}(\alpha)$ and $\text{Re}(\alpha)$, respectively. In additions, the dependence of the growth rate on E_a at $\tau^{c/v}=3$ and $\tau^{c/v}=5$ with $\gamma=1.2$, $Q=50$, $\vartheta=20$ and $f=1$ is shown. As seen, the neutral stability limit for the fundamental mode is at larger E_a for the case of $\tau^{c/v}=3$ (i.e., $E_a=27.32$), compared with that for the case of $\tau^{c/v}=5$ (i.e., $E_a=27.12$). With E_a increases, the growth rate increases accordingly, while the corresponding frequency approaches zero at $E_a=48.25$ and $E_a=46.82$ for $\tau^{c/v}=3$ and $\tau^{c/v}=5$, respectively. A further increase in E_a from these point would lead to the bifurcation of the fundamental eigenmode into two nonoscillatory eigenvalues (with zero $\text{Im}(\alpha)$) — one that decreases to zero asymptotically and the other increases with E_a. The overall features in this spectrum are similar to the case discussed in section 6.3.1 on the LSA of idealized detonation, but the values are shifted due to the presence of vibrational nonequilibrium.

The behaviour of the first overtone is relatively different from that of the fundamental mode. As presented in Figure 6.3, when E_a is beyond its neutral stability limit, the growth rate of the first overtone increases while its frequency decreases. Unlike the fundamental mode, there is no bifurcation of eigenvalues throughout the selected E_a range. By comparing with the spectra in the fundamental mode, the growth rate of the first overtone always has a steeper slope as E_a goes to higher value. Furthermore, migrations of the curves are observed as $\tau^{c/v}$ varies. For instance, the frequency is 1.27 for $\tau^{c/v}=3$ at $E_a=33$, whereas it is 1.37 for $\tau^{c/v}=5$ at the same E_a. Nevertheless, the overall trends in the first overtone are similar at different $\tau^{c/v}$. The existence of this mode may be attributed to the multi-chemical kinetics involved in LSA (in this case, the vibrational-chemical coupling mechanism involving both chemical reaction and vibrational relaxation) since the presences of this mode is also observed in the LSA of pathological detonation reported by Sharpe [19], but not in the case of idealized detonation considering one single-step Arrhenius chemistry only.

Regarding the analysis of the neutral stability limit in the fundamental mode, Figure 6.4 shows the relationship of the $\text{Im}(\alpha)$ and $\text{Re}(\alpha)$ and the dependence of $\text{Re}(\alpha)$ on E_a in the range of $25 < E_a \leq 50$ at $\tau^{c/v}=3, 5, 7, 9, 275$ and 700. Values of the neutral stability limit at different $\tau^{c/v}$ are also shown in Table 6.2. As seen, the neutral stability limit shifts to higher E_a value as $\tau^{c/v}$ decrease. Recalling the definition of $\tau^{c/v} \equiv \tau_c/\tau_v$, this implies that when vibrational relaxation is significant at low $\tau^{c/v}$, the growth rate of the fundamental mode decreases under the same activation energy E_a, and the detonation is stabilized. On the other hand, the bifurcation point at which the splitting of unstable mode into two (i.e., $\text{Im}(\alpha)=0$) shifts to a smaller $\text{Re}(\alpha)$ when $\tau^{c/v}$ is low. The splitting occurs at low growth rate also indicates that detonation is stabilized under

significant thermal (vibrational) nonequilibrium. A stability parameter proposed in the literature relating the detonation instability to the induction time scale and the reaction time scale is adopted here to explain the stabilization effect. As mentioned in Ng et al.'s work [22], the detonation stability is proportional to the ratio of induction length Δ_I to the exothermic reaction length Δ_R. On the other hand, our work in Chapter 3 revealed that the overall chemical reaction rate in detonation is always reduced and thus the half-reaction length (or Δ_R) is elongated under the vibrational nonequilibrium assumption. In that case, the stability parameter would give a smaller value at a ratio of Δ_I/Δ_R, indicating that the detonation is stabilized.

For the case of extremely large $\tau^{c/v}$, i.e., $\tau^{c/v}=275$ and $\tau^{c/v}=700$, the two stability spectra overlapped with each other as shown in Figure 6.4. Referring to Table 6.2, the percentage difference of stability limit at $\tau^{c/v}>100$ with that in $\tau^{c/v}=700$ is around 0.001% only. Both the stability limit and the bifurcation point in the spectrum remain unchanged when $\tau^{c/v} >275$, and the assumption of thermal equilibrium state should therefore be valid beyond this critical time ratio. The corresponding neutral stability limit is found at $E_a=26.45$, which is very close with the value obtained by numerical simulation (i.e., $E_a=26.47$) under the same parameter settings in section 5.1. A more comprehensive comparison will be presented later in section 6.4.4.

6.4.2 Stability spectrum by varying the overdrive factor at different time ratio
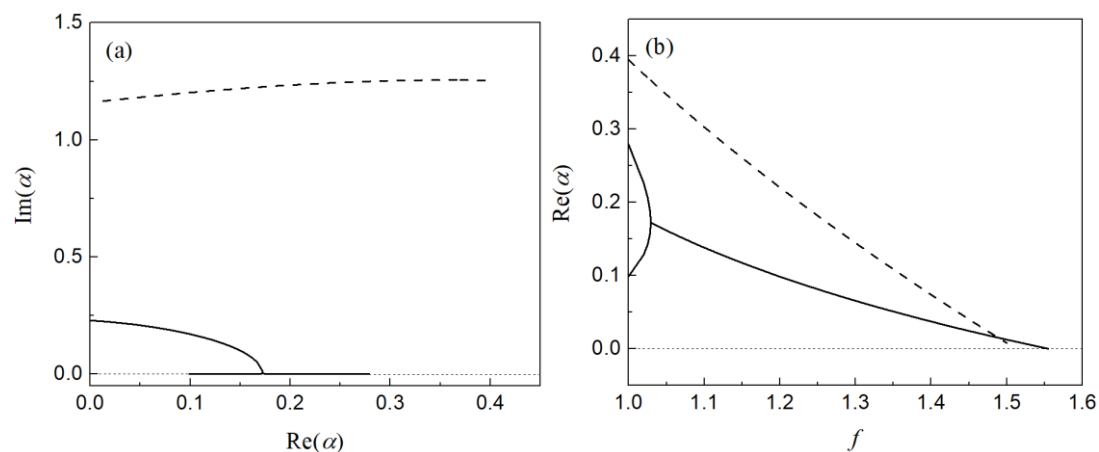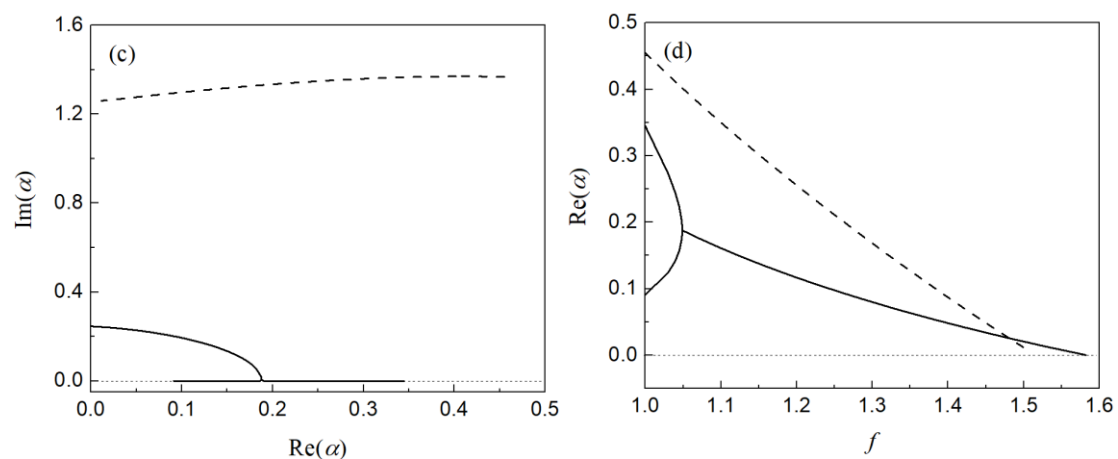
Figure 6.5 Stability spectrum showing (a) $Im(\alpha)$ vs $Re(\alpha)$ and (b) $Re(\alpha)$ vs f for $\tau^{c/v}=5$ and (c) $Im(\alpha)$ vs $Re(\alpha)$ and (d) $Re(\alpha)$ vs f for $\tau^{c/v}=10$. The solid curve represents the fundamental mode, and the dashed curve represents the first overtone. $\gamma=1.2$, $Q=50$, $\vartheta=20$ and $E_a=50$.
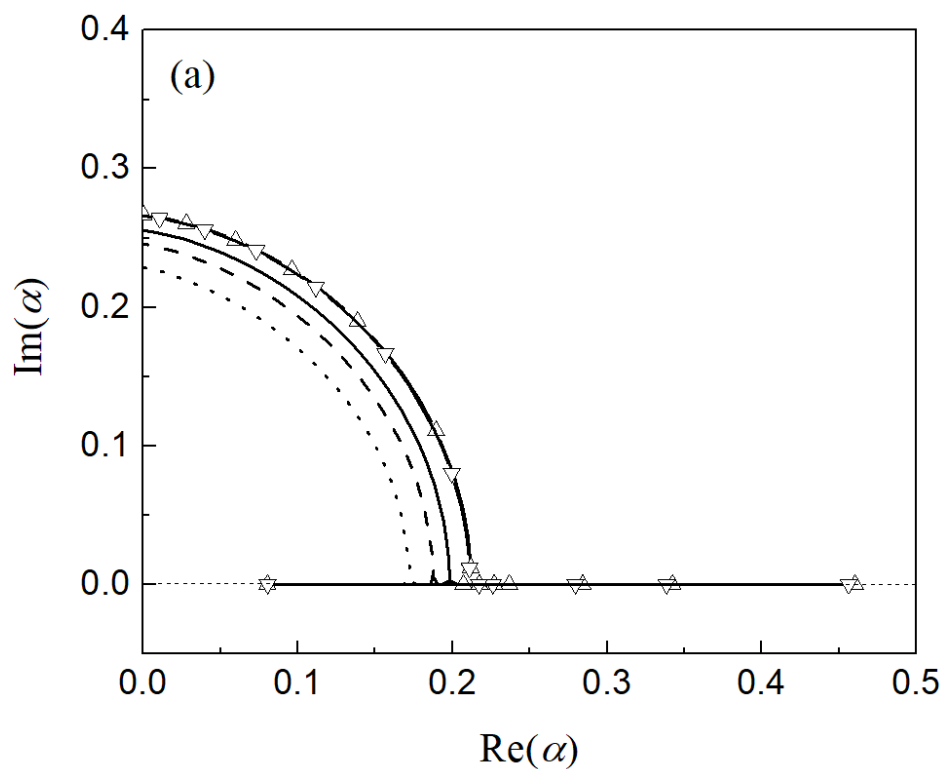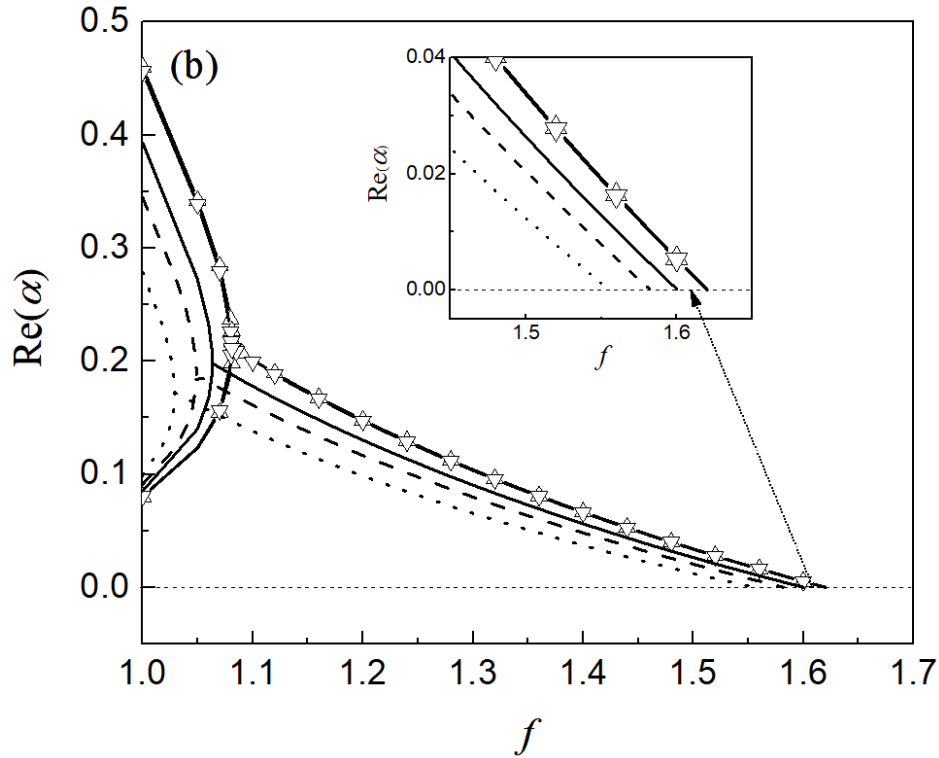
Figure 6.6 Stability spectrum showing (a) $\text{Im}(\alpha)$ vs $\text{Re}(\alpha)$ and (b) $\text{Re}(\alpha)$ vs f with the fundamental mode only at $\tau^{c/v}=5$ (dotted), $\tau^{c/v}=10$ (dashed), $\tau^{c/v}=20$ (solid), $\tau^{c/v}=252$ (solid-Δ) and $\tau^{c/v}=700$ (solid-∇). $\gamma=1.2$, $Q=50$, $\vartheta=20$ and $E_a=50$.

Table 6.3 Summary of the neutral stability limit f for fundamental mode at different $\tau^{c/v}$ by LSA.

$\tau^{c/v}$	Neutral stability limit f
5	1.555
10	1.582
20	1.600
30	1.607
200	1.610
251	1.619
252	1.620
400	1.620
700	1.620

As mentioned in the previous chapter, the increase of the degree of overdrive f can stabilize the detonation, and hence, a variation of the stability spectrum with f for the selected $\tau^{c/v}$, i.e., $\tau^{c/v}=5$ and 10 are investigated in this section and is presented in Figure 6.5. The corresponding neutral stability limit for the fundamental mode is at

f=1.555 for $\tau^{c/v}$=5 and at f=1.582 for $\tau^{c/v}$=10, above which the detonation is stabilized. While the parameters γ=1.2, Q=50, ϑ=20 and E_a=50 are fixed, two unstable nonoscillatory modes are observed at f=1 initially. As f increases, the two modes converge to a single oscillatory mode (i.e., with Im(α)>0) at f=1.0292 for $\tau^{c/v}$=5 and at f=1.0488 for $\tau^{c/v}$=10, respectively. With further increases in f, the growth rate of the unstable mode decreases to zero asymptotically, whereas the disturbance frequency increases until the neutral stability limit is reached. The overall stability behaviour is similar to that displayed in section 6.4.1, but the development of the spectrum is in the opposite way.

Considering the stability spectrum for the first overtone, the corresponding growth rate decay almost linearly to zero as f increases, with a decay rate much faster than that of the fundamental mode. In contrast to the tendency reported in Figure 6.3 under section 6.4.1, the frequency increases slightly with decreasing growth rate.

To closely examine the migration of the stability spectra for the fundamental mode under the change of $\tau^{c/v}$, the studied cases (i.e., $\tau^{c/v}$=5, 10, 20, 252, and 700) are grouped and presented in Figure 6.6, under a range of $1 \leq f \leq 1.7$. Table 6.3 summarized the corresponding neutral stability limit f for selected $\tau^{c/v}$. The neutral stability limit generally shifts to lower f as $\tau^{c/v}$ decrease. It implies that under the same f, the detonation is stabilized due to the vibrational nonequilibrium effect. Moreover, a shift of the convergence point to smaller Re(α) (or lower growth rate) at lower $\tau^{c/v}$ is observed in Figure 6.6a, and thus the stabilization effect by vibrational relaxation is further revealed. As discussed in section 5.3 under Chapter 5, the competition between the increase of f and the decrease of $\tau^{c/v}$ is again manifested through the present linear stability analysis.

Finally, two cases of very large $\tau^{c/v}$ (i.e., $\tau^{c/v}$=252 and 700) are presented in the same figure, and the overlapping of these two spectra reveals that no further shift of limit is identified. As seen in Table 6.3, the degree of shifting in the neutral stability limit becomes little as $\tau^{c/v}$ increases. For these particular parameter sets, the detonation can be treated as in the thermal equilibrium state when $\tau^{c/v} \geq 252$. The corresponding neutral stability limit is f=1.62.

6.4.3   Stability spectrum by varying characteristic vibrational temperature at different time ratio
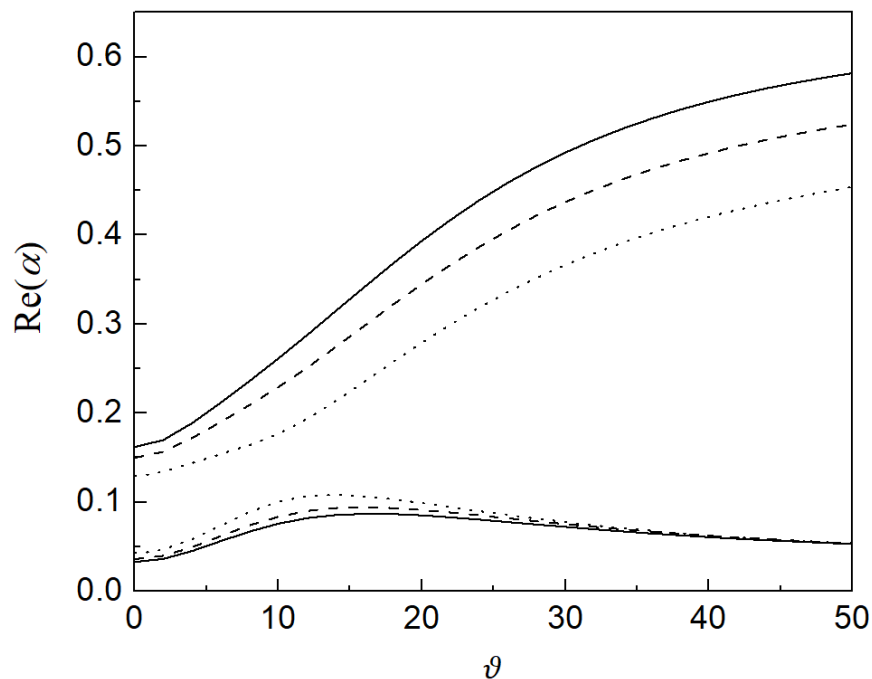
Figure 6.7 Stability spectrum showing $Re(\alpha)$ vs ϑ with the fundamental mode only for $\tau^{c/v}=5$ (dotted), $\tau^{c/v}=10$ (dashed) and $\tau^{c/v}=20$ (solid). $\gamma=1.2$, $Q=50$, $E_a=50$ and $f=1$.
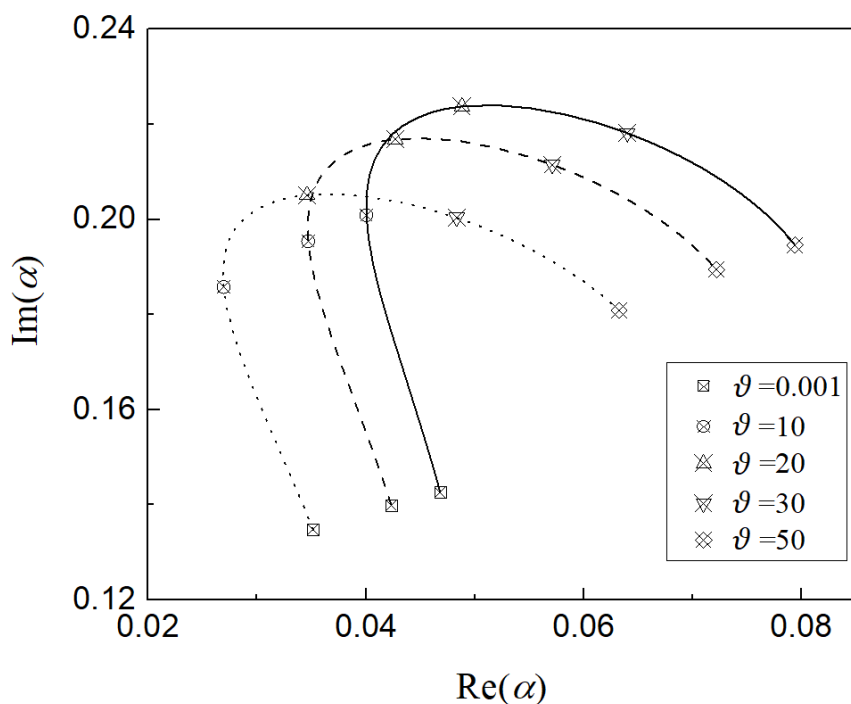
Figure 6.8 Stability spectrum showing $Im(\alpha)$ vs $Re(\alpha)$ of the fundamental mode only for $\tau^{c/v}=5$ (dotted), $\tau^{c/v}=10$ (dashed) and $\tau^{c/v}=20$ (solid) in the range of ϑ from 0.01 to 50. $\gamma=1.2$, $Q=50$, $E_a=30$ and $f=1$.

When the detonation is assumed to be at vibrational nonequilibrium, vibrational temperature ϑ is used to characterize the vibrational energy content inside the system. The change of ϑ under different $\tau^{c/v}$ for the fundamental mode is therefore worth investigating in this section, and two unstable conditions are considered in the analysis with $\gamma=1.2$, $Q=50$ and $f=1$: the case at $E_a=30$ in which only one unstable oscillatory mode exists, and the case at $E_a=50$ in which two nonoscillatory unstable modes are determined (Referring to Figure 6.4).

Figure 6.7 shows the dependence of the growth rate on ϑ at $E_a=50$ for $\tau^{c/v}=5$, 10 and 20. Since the unstable mode is nonoscillatory, $\text{Im}(\alpha)$ is always zero under this condition. As ϑ decreases, the difference in the growth rate between the two unstable modes is narrowed. The increase in $\tau^{c/v}$ generally moves the upper unstable mode to a higher level denoting higher growth rate (for instance, $\text{Re}(\alpha)=0.45$ for $\phi=50$ at $\tau^{c/v}=5$ and $\text{Re}(\alpha)=0.58$ for $\phi=50$ at $\tau^{c/v}=20$), while the effect on the lower unstable mode is relatively weak. In particular, the change of $\text{Re}(\alpha)$ for the upper unstable mode can be over 0.5, but the change of $\text{Re}(\alpha)$ for the lower unstable mode is within 0.05 only for all three cases. The lower $\text{Re}(\alpha)$ of the upper unstable mode at small ϑ reveals the stabilization of detonation. Note that although the convergence tendency of the growth rate for the two unstable eigenmodes along with the change of ϑ is similar to that presented in Figure 6.4, these modes do not converge to a single one, even at very small ϑ such as 0.001.

Another case of a single oscillatory unstable mode near the stability limit is shown in Figure 6.8, where the relationship of $\text{Re}(\alpha)$ and $\text{Im}(\alpha)$ at $E_a=30$ for $\tau^{c/v}=5$, 10 and 20 are demonstrated in the range of ϑ from 0.01 to 50. Similar to the case presented in the previous paragraph, no neutral stability is found under the selected ϑ range, but a minimum growth rate (or minimum $\text{Re}(\alpha)$) is identified at around $\vartheta=10$ for all three $\tau^{c/v}$ cases. Below this minimum growth rate, a further decrease in ϑ would lead to an increase in the growth rate again, while the frequency decreases accordingly. If ϑ increases beyond this minimum point, the growth rate increases comparatively faster, with the frequency increases first and then decreases. Generally, the stability spectrum shifts to higher $\text{Re}(\alpha)$ as $\tau^{c/v}$ increase, and this fit with the observations in Figure 6.4.

Recall the definition of the vibrational relaxation mechanism in Eq. (6.6), the relaxation rate depends heavily on the vibrational time scale τ_v (and thus $\tau^{c/v}$) instead of ϑ. Moreover, the low sensitivity of ϑ to the change of half reaction length under the vibrational nonequilibrium state has been also reported in Chapter Chapter 3under section 3.3. Together with the findings in this part, it is suggested that ϑ plays a minor

role in stabilizing the detonation whenever the state is under vibrational nonequilibrium. Therefore, no critical time ratio $\tau^{c/v}$ could be identified.

6.4.4   Comparison with stability analysis results computed by direct numerical simulation

Table 6.4 Comparison of the neutral stability limit and period of oscillation computed by LSA and DNS, respectively. $\gamma=1.2$, $Q=50$ and $\vartheta=20$.

Case	Linear stability analysis		Direct numerical simulation	
	NSL	PO	NSL	PO
I	E_a=26.46	10.63	E_a=26.47	10.64
II	E_a=27.13	12.14	E_a=27.14	12.15
III	f=1.62	8.02	f=1.62	8.03
IV	f=1.555	9.51	f=1.554	9.52

NSL: Neutral stability limit   PO: Period of oscillation

Case I: f=1 is fixed at thermal equilibrium

Case II: f=1 is fixed at thermal nonequilibrium with $\tau^{c/v}$=5

Case III: E_a=50 is fixed at thermal equilibrium

Case IV: E_a=50 is fixed at thermal nonequilibrium with $\tau^{c/v}$=5

Table 6.5 Conversion factor of $\text{Im}(\alpha)$ from the present work to the Erpenbeck scale at different f. $\gamma=1.2$, $Q=50$, $E_a=50$.

f	Conversion factor
1.000	2.40294170
1.550	2.88156885
1.555	2.88574914
1.580	2.90566893
1.590	2.91345575
1.600	2.92146604
1.620	2.93716081
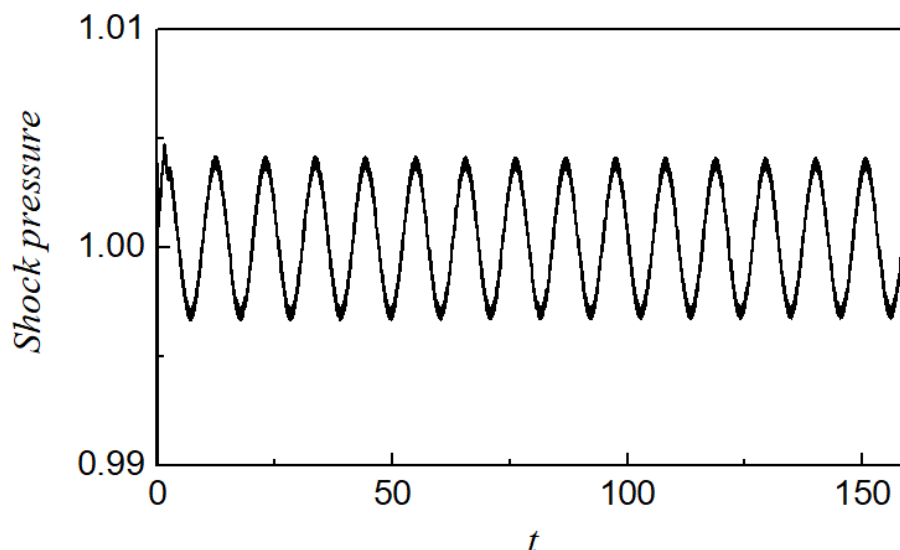
Figure 6.9 Shock pressure history at E_a=26.47 under the thermal equilibrium state computed by DNS. γ=1.2, Q=50, ϑ=20 and f=1.

Many literature have revealed that linear stability analysis (LSA) can give an excellent prediction on both the neutral stability limit and the corresponding period of oscillation (in terms of disturbance frequency) near the stability boundary. To justify the LSA findings in this chapter, direct numerical simulation (DNS) is conducted for the selected cases to see if the results computed in both approaches are matched. The numerical method strictly follows the discussion in Chapter 5. Notably, section 6.4.2 and 6.4.3 have demonstrated an extreme case of $\tau^{c/v}$=700 representing the thermal equilibrium state with predicted stability limit, and these would also be verified in this section.

Table 6.4 shows a comparison of the neutral stability limit and the period of oscillation obtained from both the LSA and the DNS for the selected four cases. The first two cases, i.e., Case I and Case II, vary with E_a under the thermal equilibrium state and the thermal nonequilibrium state for $\tau^{c/v}$=5, respectively, whereas the other two, i.e., Case III and Case IV, vary with f under the thermal equilibrium state and the thermal nonequilibrium state for $\tau^{c/v}$=5. Notably, as mentioned in section 5.1 under Chapter 5, the vibrational relaxation model was neglected in the chemical kinetics in order to describe a case of the thermal equilibrium state, while the vibrational energy term was calculated with $T_v = T_{tr}$. For reference, a shock pressure history for the case with E_a=26.47 under the thermal equilibrium state is presented in Figure 6.9, representing the condition for Case I. The period of oscillation in averaged is determined to be 10.64.

Regarding the normal mode results from LSA subjected to the changes of E_a and f, the cases with $\tau^{c/v}$=700 denoting the thermal equilibrium state are presented in Case I

and III, while the case with $\tau^{c/v}$=5 are presented in Case II and IV denoting the thermal nonequilibrium state. The period of oscillation PO in LSA can be evaluated through $Im(\alpha)$ as follows:

$$PO = \frac{2\pi}{Im(\alpha)} \tag{6.36}$$

where $Im(\alpha)$ is on the Erpenbeck scale. As discussed in section 6.3.1 also, it is convenient to use the Erpenbeck scale for the evaluation of the PO. The conversion factors have been summarized in Table 6.5 for reference. Taking Case I as an example, $Im(\alpha)$ obtained in LSA at E_a=26.46 is 0.245, and thus the period of oscillation can be calculated by $2\pi/(0.246 \times 2.40294170)$ equal to 10.63.

As seen in Table 6.4, the data from the two approaches matched closely with each other, and the difference was within 0.01. Hence, the findings in this chapter on LSA is well validated considering detonation with vibrational-chemical coupling kinetics.

6.5   Summary

A normal mode linear stability analysis of one-dimensional detonation with a vibrational-chemical coupling mechanism is investigated in this chapter. With the introduction of time ratio $\tau^{c/v}$, the chemical kinetics are constructed such that an Arrhenius reaction model is coupled with the vibrational relaxation model using the concept of averaged temperature. Parametric studies are then conducted by varying 1) the activation energy E_a in the Arrhenius model 2) the degree of overdrive f and 3) the characteristic vibrational temperature ϑ in vibrational relaxation model while γ=1.2 and Q=50 are kept constant.

On the variation of E_a with different $\tau^{c/v}$, both the fundamental mode and the first overtone are observed in the stability spectrum. The emergence of the first overtone may be attributed to the multi-chemical kinetics involved in the reaction model, analogous to the LSA on pathological detonation found in the literature. As $\tau^{c/v}$ decreases, neutral stability limit shifts to a higher E_a and the bifurcation point shifts to a slower growth rate accordingly. This implies that the detonation is stabilized under vibrational nonequilibrium, due to the fact that the overall reaction rate is reduced. Moreover, neither the neutral stability limit nor bifurcation point would be shifted in the stability spectrum when $\tau^{c/v} \geq 275$, and this critical condition is assumed to be at thermal equilibrium. At this stage, the vibrational time scale is sufficiently large

compared with the chemical time scale, and the equilibrium state is established quickly right after the shock. The corresponding neutral stability limit is at E_a=26.46.

Regarding the detonation with different degrees of overdrive f, both the fundamental mode and the first overtone are observed in the analysis. Similar to the discussion in Chapter 5, both the increase of f and the decrease of $\tau^{c/v}$ provide the stabilization effect in detonation propagation, and the competition between the two contributed to the shift of both the stability limit and the bifurcation point. Therefore, the neutral stability limit shifts to lower f as $\tau^{c/v}$ decreases, denoting the significant vibrational nonequilibrium state. The critical $\tau^{c/v}$ above which the thermal equilibrium is reached is at $\tau^{c/v}$=252 and the corresponding neutral stability limit is at f=1.62.

For the sensitivity study on the change of ϑ, two conditions are considered in the analysis—one has a single unstable oscillatory eigenmode, and the other has two unstable nonoscillatory eigenmodes. For the case with a single eigenmode, a minimum growth rate is determined at approximately ϑ=10 for all $\tau^{c/v}$, and a shift of the stability spectrum to a lower growth rate as $\tau^{c/v}$ decreases is again identified. Similarly, in the case of two eigenmodes, a shift of the upper eigenmode to the lower growth rate with decreasing $\tau^{c/v}$ is revealed, but little influence on the shift of the lower eigenmode is manifested under the change of ϑ. Overall, ϑ shows little effect on stabilizing the detonation compared with that of the change of E_a or f, and the number of eigenmodes remains unchanged throughout the selected ϑ ranges.

To justify the normal mode result from LSA, DNS is conducted on selected cases at different states of vibrational equilibrium and nonequilibrium to see if the computed stability limit and period of oscillation matched with each other. A conversion of the Erpenbeck scale with the present work is performed as necessary. It is shown that the difference between the two approaches is within a value of 0.01 in either the neutral stability limit or the period of oscillation. The analysis of the vibrational-chemical coupling mechanism in this chapter is well validated.

Chapter 7 Conclusions

7.1   Summary

Detonation, in reality, is inherently unstable during propagation. Recent numerical studies on gaseous detonation involving hydrogen and oxygen reveal that the vibrational mode of energy in molecules is not necessary to be at thermal equilibrium right after the start of a chemical reaction. The present work aims at investigating the importance of vibrational relaxation (and thus the vibrational-chemical coupling kinetics) in detonation phenomenon, in particular from the theoretical aspect. The critical issues include 1) the vibrational nonequilibrium effect on half-reaction length within the reaction zone, which is closely related to the detonation cell size, 2) the vibrational nonequilibrium effect on the detonation stability. Both analytical and numerical approaches are utilized in studying these problems such that the results could be compared for verifications. To simplify the theoretical model derivation, the chemical reaction model and vibrational relaxation model are taken to be the simplest form while the major detonation physics are retained.

With the establishment of the extended ZND model with a time ratio $\tau^{c/v}$ denoting the chemical reaction time scale versus vibrational relaxation time scale during detonation wave propagation, a different state of nonequilibrium could be evaluated through the change of $\tau^{c/v}$. By fixing γ and Q, parametric studies are conducted on this model by changing 1) activation energy E_a, 2) time ratio $\tau^{c/v}$ and 3) characteristic vibrational temperature ϑ using single-step or two-step Arrhenius equations. Results indicate that the half-reaction length is elongated if the state is further away from the equilibrium since the overall chemical reaction rate is reduced. Moreover, a critical time ratio $\tau^{c/v}$ exists, above which the half-reaction length converges to the equilibrium solution. The vibrational relaxation effect should be neglectable in this condition.

To justify the use of the extended ZND model for the prediction of half reaction length in large scale hydrogen-oxygen detonation simulations at thermal nonequilibrium, a case of stoichiometric hydrogen-oxygen-argon detonation is solved numerically as a benchmark for illustration. To imitate the detailed chemistry in simulation, parameters in single-step/two-step Arrhenius equations are modified accordingly. With these simplified chemical models, the half-reaction length ratio evaluated from the extended ZND model is compared with that from numerical simulation involving detailed chemistry. A better prediction is revealed in the case with hydrogen as the dominant species instead of oxygen. To further verify whether the simplified chemical models are

applicable in numerical simulation, simulations with modified single-step and two-step chemical models were performed and compared with the simulations using detailed chemistry in terms of half reaction length. Small discrepancies were determined. This extended ZND model could therefore be treated as an analytical tool in predicting the half-reaction length in simulations under vibrational nonequilibrium.

Considering the work on detonation stability, linear stability analysis (LSA) has been developed for almost half a century and the information regarding the number of eigenmodes, stability boundary and related frequencies could be obtained based on this analytical approach. However, LSA gives poor prediction if the detonation is far from the stability limit, due to the presence of a nonlinear effect. In this case, direct numerical simulation (DNS) would be a better choice to evaluate the unstable modes. Nevertheless, the stability behaviour computed from the two approaches should show a good agreement near the stability boundary which is linear in nature, and these have been verified in this report.

Following the establishment of LSA with the detonation considering vibrational-chemical coupling kinetics, three parameters vary independently in the analysis under the change of $\tau^{c/v}$ and the corresponding stability spectra are presented. These parameters include the activation energy E_a, the degree of overdrive f and the characteristic vibrational temperature ϑ. Generally, the neutral stability limit shifts to higher E_a and lower f independently as $\tau^{c/v}$ decreases, indicating that the detonation is stabilized under significant vibrational nonequilibrium. Compared with the two factors presented above, ϑ plays little role in stabilizing the detonation. On the change of E_a, the slow chemical reaction rate under vibrational nonequilibrium in overall is the major reason accounted for the stabilization effect; whereas on the change of f, the competition of the stabilization effect in both f and $\tau^{c/v}$ would lead to a shift of neutral stability limit eventually. The findings in LSA are finally validated by comparing it with the DNS approach under the same conditions. The discrepancies between the two approaches are small, indicating that the stability behaviour demonstrated in LSA is well justified.

In conclusion, the present study elucidates the importance of vibrational relaxation mechanism in gaseous detonation in terms of theoretical modelling. By modifying the well-known ZND detonation model, the overall chemical reaction rate under vibrational nonequilibrium is revealed and the resulted trend is similar to that obtained in numerical simulations. Together with a normal mode linear stability analysis under the same condition, it is shown that the detonation could be stabilized under the state

of vibrational nonequilibrium. The analytical tools developed in this study provide insights on how this coupling effect is manifested before conducting large scale numerical simulation on detonation under the same state of nonequilibrium.

7.2   Future work

The present work mainly focuses on the investigation in gaseous detonation, particularly the one involving hydrogen. The concept of vibrational-chemical coupling could be extended to other types of detonation problems if necessary, depending on the assumption or predictions made. Last but not least, the linear stability analysis presented in this report is one-dimensional only. The development of this analysis into two-dimensional form is possible and requires further investigations.

Appendices

A. Derivation of Rankine Hugoniot relation in extended ZND model

Starting from the Rayleigh line and Hugoniot curve in Eq. (2.11) and (2.21), while subscript 0 is dropped out for convenience:

$$\gamma M^2 = \frac{p-1}{1-v} \tag{A.1}$$

$$\frac{\alpha p v - 1}{\gamma - 1} + \frac{1}{2}(p+1)(v-1) + e_v - \lambda Q = 0 \tag{A.2}$$

From Eq. (A.1),

$$\gamma M^2 (1-v) + 1 = p \tag{A.3}$$

Substitute Eq. (A.3) into Eq. (A.2) gives

$$\frac{\alpha[\gamma M^2(1-v)+1]v - 1}{\gamma - 1} + \frac{([\gamma M^2(1-v)+1]+1)(v-1)}{2} - \lambda Q + e_v \\ = 0 \tag{A.4}$$

After some mathematical manipulation, Eq. (A.4) can be written in a form of quadratic equations with v as the subject,

$$v^2 - \frac{2[\gamma M^2 + 1 + M^2(\alpha - 1) + (\alpha - 1)/\gamma]}{M^2[\gamma + 1 + 2(\alpha - 1)]}v \\ + \frac{2 + \gamma M^2 - M^2 + [2(\gamma - 1)(\lambda Q - e_v)]/\gamma}{M^2[\gamma + 1 + 2(\alpha - 1)]} = 0 \tag{A.5}$$

By defining $\varsigma = \alpha - 1$, Eq. (A.5) is expressed in terms of ς,

$$v^2 - \frac{2(\gamma M^2 + 1)(1 + \varsigma/\gamma)}{M^2(\gamma + 1 + 2\varsigma)}v + \frac{2 + \gamma M^2 - M^2 + [2(\gamma - 1)(\lambda Q - e_v)]/\gamma}{M^2[\gamma + 1 + 2\varsigma]} = 0 \tag{A.6}$$

Solutions of v can be rewritten as quadratic form such that

Appendices

$$\upsilon \qquad \text{(A.7)}$$

$$= \frac{(\gamma M^2 + 1)(1 + \varsigma/\gamma)}{M^2(\gamma + 1 + 2\varsigma)}$$

$$\mp \sqrt{\frac{[(\gamma M^2 + 1)(1 + \varsigma/\gamma)]^2}{M^4(\gamma + 1 + 2\varsigma)^2} - \frac{2 + \gamma M^2 - M^2 + [2(\gamma - 1)(\lambda Q - e_{\mathrm{v}})]/\gamma}{M^2(\gamma + 1 + 2\varsigma)}}$$

After simplifications, the discriminant in Eq. (A.7) is reformulated as below

$$\frac{(M^2 - 1)^2}{M^4(\gamma + 1 + 2\varsigma)^2} - \frac{2M^2[\gamma^2 - 1 + 2\varsigma(\gamma - 1)]/\gamma}{M^4(\gamma + 1 + 2\varsigma)^2} \lambda Q \qquad \text{(A.8)}$$

$$+ \frac{2M^2[\gamma^2 - 1 + 2\varsigma(\gamma - 1)]/\gamma}{M^4(\gamma + 1 + 2\varsigma)^2} e_{\mathrm{v}} + \frac{(\gamma M^2 - 1)^2/\gamma^2}{M^4(\gamma + 1 + 2\varsigma)^2} \varsigma^2$$

$$+ \frac{2(1/\gamma + M^4)}{M^4(\gamma + 1 + 2\varsigma)^2} \varsigma$$

And the overall υ profile obtained from Rankine-Hugoniot analysis under steady-state can be expressed as

$$\upsilon = \frac{(\gamma M^2 + 1)(1 + \varsigma/\gamma)}{M^2(\gamma + 1 + 2\varsigma)} [1 \mp w_\upsilon(\varsigma)\xi(\lambda, e_{\mathrm{v}}, \varsigma)], \qquad \text{(A.9)}$$

where

$$w_\upsilon(\varsigma) = \frac{M^2 - 1}{(\gamma M^2 + 1)(1 + \varsigma/\gamma)},$$

$$\xi(\lambda, e_{\mathrm{v}}, \varsigma) = \sqrt{1 - \frac{\lambda Q}{\Omega(\varsigma)} + \frac{e_{\mathrm{v}}}{\Omega(\varsigma)} + \frac{\varsigma^2}{\Phi_1} + \frac{\varsigma}{\Phi_2}},$$

$$\Omega(\varsigma) = \frac{\gamma(M^2 - 1)^2}{2M^2[\gamma^2 - 1 + 2\varsigma(\gamma - 1)]},$$

$$\Phi_1 = \frac{\gamma^2(M^2 - 1)^2}{(\gamma M^2 - 1)^2},$$

$$\Phi_2 = \frac{\gamma(M^2 - 1)^2}{2(\gamma M^4 + 1)}$$

The derivation for profile p is similar to the discussion above, but Eq. (A.3) is replaced by the below expression in terms of p instead,

Appendices

$$1 - \frac{p - 1}{\gamma M^2} = v \qquad \text{(A.10)}$$

B. Derivation of linear stability analysis of detonation with vibrational relaxation

As discussed in Eq. (6.1), the reaction Euler equations are formulated as follows:

$$\frac{Dv}{Dt} - v\nabla \cdot u^l = 0, \quad \frac{Du^l}{Dt} + v\nabla \cdot p = 0, \quad \frac{De}{Dt} + p\frac{Dv}{Dt} = 0, \tag{B.1}$$

$$\frac{D\lambda}{Dt} = r = K(1-\lambda)\exp\left(-\frac{\phi}{T_a}\right), \quad T_a = \sqrt{T_{tr}T_v}$$

$$\frac{D\varepsilon}{Dt} = r_\varepsilon = \frac{\varepsilon^{eq} - \varepsilon}{\tau_v}$$

where the definition of e can be written as

$$e = \frac{pv}{\gamma - 1} - \lambda\varrho + \varepsilon, \quad T_{tr} = pv, \tag{B.2}$$

$$\varepsilon = \frac{\eta}{\exp(\eta/T_v) - 1} \tag{B.3}$$

Thus, the reactive Euler equation for energy is expressed in another form by considering the relation in Eq. (B.2), and is given below

$$v\frac{Dp}{Dt} + \gamma pv\nabla \cdot u = (\gamma - 1)(\varrho r - r_\varepsilon) \tag{B.4}$$

With the perturbation equations expressed in Eq. (6.28) and (6.29),

$$z = z^*(x) + z'(x)\exp(\alpha t), \quad \psi = \psi'\exp(\alpha t) \tag{6.28}$$

where

$$z = [v, u, p, \lambda, \varepsilon]^T \tag{6.29}$$

The linear differential equations for the complex perturbation eigenfunctions can be formulated one by one. Takes the mass conservation equations in Eq. (B.1) as an example,

$$\frac{\partial v}{\partial t} + u\frac{\partial v}{\partial x} - v\frac{\partial u}{\partial x} = 0 \tag{B.5}$$

Appendices

The corresponding perturbation for v and ψ are

$$v = v^*(x) + v'(x)\exp(\alpha t), \tag{B.6}$$
$$\psi = \psi'\exp(\alpha t) \tag{B.7}$$

And the derivatives of v and ψ would be

$$\frac{\partial v}{\partial x} = \frac{\partial v^*}{\partial x} + \frac{\partial v'}{\partial x}\exp(\alpha t) \tag{B.8}$$

$$\frac{\partial v}{\partial t} = \alpha v'\exp(\alpha t) \tag{B.9}$$

$$\frac{\partial \psi}{\partial x} = 0 \tag{B.10}$$

$$\frac{\partial \psi}{\partial t} = \alpha\psi'\exp(\alpha t) \tag{B.11}$$

Substituting Eq. (B.8) - (B.11) into Eq. (B.5) and linearized the perturbation equations will give

$$\alpha v' + \left(u^*\frac{\partial v'}{\partial x} - v^*\frac{\partial u'}{\partial x}\right) + \left(-\frac{\partial u^*}{\partial x}v' + \frac{\partial v^*}{\partial x}u'\right) - \left(\alpha\frac{\partial v^*}{\partial x}\psi'\right) = 0 \tag{B.12}$$

Other perturbation equations can then be constructed based on the steps discussed above. A full system of linear differential equations is then formulated as below,

$$\alpha v' + \left(u^*\frac{\partial v'}{\partial x} - v^*\frac{\partial u'}{\partial x}\right) + \left(-\frac{\partial u^*}{\partial x}v' + \frac{\partial v^*}{\partial x}u'\right) - \left(\alpha\frac{\partial v^*}{\partial x}\psi'\right) = 0 \tag{B.13}$$

$$\alpha u' + \left(u^*\frac{\partial u'}{\partial x} + \frac{v^*}{\gamma}\frac{\partial p'}{\partial x}\right) + \left(\frac{\partial u^*}{\partial x}u' + \frac{\partial p^*}{\partial x}\frac{v'}{\gamma}\right) - \left(\alpha\frac{\partial u^*}{\partial x}\psi'\right) = 0$$

$$\alpha p' + \left(\gamma p^*\frac{\partial u'}{\partial x} + u^*\frac{\partial p'}{\partial x}\right)$$

$$+ \left(\left[\frac{(\gamma - 1)}{v}\left(\left(\frac{\varrho r - r_\varepsilon}{v}\right) - \left(\varrho\frac{\partial r}{\partial v^*} - \frac{\partial r_\varepsilon}{\partial v^*}\right)\right)\right]v' + \frac{\partial p^*}{\partial x}u'\right.$$

$$+ \left[\gamma\frac{\partial u^*}{\partial x} - \frac{(\gamma - 1)}{v}\left(\varrho\frac{\partial r}{\partial p^*} - \frac{\partial r_\varepsilon}{\partial p^*}\right)\right]p' - \left[\frac{(\gamma - 1)}{v}\varrho\frac{\partial r}{\partial \lambda^*}\right]\lambda'$$

$$- \left[\frac{(\gamma - 1)}{v}\left(\varrho\frac{\partial r}{\partial \varepsilon^*} - \frac{\partial r_\varepsilon}{\partial \varepsilon^*}\right)\right]\varepsilon') - \left(\alpha\frac{\partial p^*}{\partial x}\psi'\right) = 0$$

$$\alpha\lambda' + \left(u^*\frac{\partial\lambda'}{\partial x}\right) + \left(-\frac{\partial r}{\partial v^*}v' + \frac{\partial\lambda^*}{\partial x}u' - \frac{\partial r}{\partial p^*}p' - \frac{\partial r}{\partial\lambda^*}\lambda' - \frac{\partial r}{\partial\varepsilon^*}\varepsilon'\right)$$

$$- \left(\alpha\frac{\partial\lambda^*}{\partial x}\psi'\right) = 0$$

$$\alpha\varepsilon' + \left(u^*\frac{\partial\varepsilon'}{\partial x}\right) + \left(-\frac{\partial r_\varepsilon}{\partial v^*}v' + \frac{\partial\varepsilon^*}{\partial x}u' - \frac{\partial r_\varepsilon}{\partial p^*}p' - \frac{\partial r_\varepsilon}{\partial\varepsilon^*}\varepsilon'\right) - \left(\alpha\frac{\partial\varepsilon^*}{\partial x}\psi'\right)$$

$$= 0$$

The system can be written in the form of

$$A^*z'_x + (\alpha \cdot I + C^*)z' - \alpha z_x^*\psi' = 0 \tag{B.14}$$

and it is analogous to Eq. (6.18) and (6.19).

Since the reaction model is in single-step Arrhenius form together with Park's two-temperature model, r is formulated as

$$r = K(1 - \lambda)\exp\left(-\frac{\phi}{\sqrt{p\upsilon T_v}}\right) \tag{B.15}$$

And p, υ, λ and ε (in terms of T_v) are the independent variables for the derivatives r.

r_ε is represented by the Landau-Teller model and the full expression is given as

$$r_\varepsilon = \frac{\dfrac{\eta}{\exp(\eta/p\upsilon) - 1} - \varepsilon}{\tau_v} \tag{B.16}$$

And p, υ, and ε are the independent variables for the derivatives r_ε.

References

[1] Li J-M, Teo CJ, Lim KS, Wen C-S, Khoo BC. Deflagration to detonation transition by hybrid obstacles in pulse detonation engines. 49th AIAA/ASME/SAE/ASEE Joint PropulsionConference2013. p. 3657.

[2] Ma F, Choi J-Y, Yang V. Thrust chamber dynamics and propulsive performance of single-tube pulse detonation engines. Journal of propulsion and power. 2005;21:512-26.

[3] Poludnenko AY, Chambers J, Ahmed K, Gamezo VN, Taylor BD. A unified mechanism for unconfined deflagration-to-detonation transition in terrestrial chemical systems and type Ia supernovae. Science. 2019;366:eaau7365.

[4] Mallard E, and H. Le Chatelier. Experimental and Theoretical Researches on the Combustion of Explosive Gaseous Mixtures. Ann mines. 1883;8:274-568.

[5] Abel FA. XIV. Contributions to the history of explosive agents. Philosophical transactions of the Royal Society of London. 1869:489-516.

[6] Zeldovich YB. On the theory of the propagation of detonation in gaseous systems. 1940.

[7] Von Neumann J. Theory of detonation waves. O.S.R.D. Rept.; 1942. p. 549.

[8] Döring W. On detonation processes in gases. Ann Phys. 1943;43:9.

[9] Lee JH. The detonation phenomenon: Cambridge University Press Cambridge; 2008.

[10] Fickett W, Davis WC. Detonation: University of California Press; 1979.

[11] Erpenbeck JJ. Stability of Idealized One-Reaction Detonations. Physics of Fluids. 1964;7:684.

[12] Erpenbeck JJ. Structure and stability of the square-wave detonation. Symposium (International) on Combustion. 1963;9:442-53.

[13] Erpenbeck JJ. Stability of Steady-State Equilibrium Detonations. Physics of Fluids. 1962;5:604-14.

[14] Fickett W, Wood WW. Flow Calculations for Pulsating One-Dimensional Detonations. The Physics of Fluids. 1966;9:903-16.

[15] Lee H, Stewart DS. Calculation of linear detonation instability: one-dimensional instability of plane detonation. Journal of Fluid Mechanics. 1990;216:103-32.

[16] Short M, Stewart DS. Cellular detonation stability. Part 1. A normal-mode linear analysis. Journal of Fluid Mechanics. 1998;368:229-62.

[17] Sharpe GJ. Linear stability of idealized detonations. Proceedings of the Royal Society of London Series A: Mathematical, Physical and Engineering Sciences. 1997;453:2603.

[18] Watt SD, Sharpe GJ. One-dimensional linear stability of curved detonations. Proceedings of the Royal Society of London Series A: Mathematical, Physical and

Engineering Sciences. 2004;460:2551.

[19] Sharpe GJ. Linear stability of pathological detonations. Journal of Fluid Mechanics. 1999;401:311-38.

[20] Kasimov AR, Stewart DS. Spinning instability of gaseous detonations. Journal of Fluid Mechanics. 2002;466:179-203.

[21] Ng HD, Radulescu MI, Higgins AJ, Nikiforakis N, Lee JHS. Numerical investigation of the instability for one-dimensional Chapman–Jouguet detonations with chain-branching kinetics. Combustion Theory and Modelling. 2005;9:385-401.

[22] Ng H, Higgins A, Kiyanda C, Radulescu M, Lee J, Bates K, et al. Nonlinear dynamics and chaos analysis of one-dimensional pulsating detonations. Combustion Theory and Modelling. 2005;9:159-70.

[23] Short M, Sharpe GJ. Pulsating instability of detonations with a two-step chain-branching reaction model: theory and numerics. Combustion Theory and Modelling. 2003;7:401-16.

[24] Sharpe GJ. Numerical simulations of pulsating detonations: II. Piston initiated detonations. Combustion Theory and Modelling. 2001;5:623-38.

[25] Sharpe GJ, Falle SAEG. Numerical simulations of pulsating detonations: I. Nonlinear stability of steady detonations. Combustion Theory and Modelling. 2000;4:557-74.

[26] He L, Lee JH. The dynamical limit of one-dimensional detonations. Physics of Fluids. 1995;7:1151-8.

[27] Sharpe GJ, Falle SAEG. One-dimensional numerical simulations of idealized detonations. Proceedings of the Royal Society of London Series A: Mathematical, Physical and Engineering Sciences. 1999;455:1203.

[28] Taylor BD, Kasimov AR, Stewart DS. Mode selection in weakly unstable two-dimensional detonations Combustion Theory and Modelling. 2009;13:973-92.

[29] Watt SD, Sharpe GJ. Linear and nonlinear dynamics of cylindrically and spherically expanding detonation waves. Journal of Fluid Mechanics. 2005;522:329-56.

[30] Tsuboi N, Katoh S, Hayashi AK. Three-dimensional numerical simulation for hydrogen/air detonation: Rectangular and diagonal structures. Proceedings of the Combustion Institute. 2002;29:2783-8.

[31] Eto K, Tsuboi N, Hayashi AK. Numerical study on three-dimensional CJ detonation waves: detailed propagating mechanism and existence of OH radical. Proceedings of the Combustion Institute. 2005;30:1907-13.

[32] Taylor B, Kessler D, Gamezo V, Oran E. Numerical simulations of hydrogen detonations with detailed chemical kinetics. Proceedings of the combustion Institute. 2013;34:2009-16.

[33] Taylor B, Kessler D, Oran E. Estimates of Vibrational Nonequilibrium Time Scales

in Hydrogen-Air Detonation Waves. 24th International Colloquium on the Dynamics of Explosive and Reactive Systems. Taipei, Taiwan2013.

[34] Voelkel SJ, Raman V, Varghese P. Non-Equilibrium Reaction Rates in Hydrogen Combustion. 25th International Colloquium on the Dynamics of Explosions and Reactive Systems (ICDERS), Leeds, UK, August2015. p. 2-7.

[35] Koo H, Raman V, Varghese PL. Direct numerical simulation of supersonic combustion with thermal nonequilibrium. Proceedings of the Combustion Institute. 2015;35:2145-53.

[36] Shi L, Shen H, Zhang P, Zhang D, Wen C. Assessment of Vibrational Non-Equilibrium Effect on Detonation Cell Size. Combustion Science and Technology. 2016;189:841-53.

[37] Tarver CM. Chemical energy release in one-dimensional detonation waves in gaseous explosives. Combustion and Flame. 1982;46:111-33.

[38] Tarver CM. Chemical energy release in the cellular structure of gaseous detonation waves. Combustion and Flame. 1982;46:135-56.

[39] Tarver CM. Chemical energy release in self-sustaining detonation waves in condensed explosives. Combustion and Flame. 1982;46:157-76.

[40] Tarver CM. Multiple Roles of Highly Vibrationally Excited Molecules in the Reaction Zones of Detonation Waves. The Journal of Physical Chemistry A. 1997;101:4845-51.

[41] Gavrikov A, Efimenko A, Dorofeev S. A model for detonation cell size prediction from chemical kinetics. Combustion and flame. 2000;120:19-33.

[42] Vincenti WG, Kruger CH. Introduction to physical gas dynamics1965.

[43] He H, Yu S-T, Zhang Z-C. Direct calculations of one-, two-, and three-dimensional detonations by the CESE method. 43rd AIAA Aerospace Sciences Meeting and Exhibit2005. p. 229.

[44] Shen H, Parsani M. The role of multidimensional instabilities in direct initiation of gaseous detonations in free space. Journal of Fluid Mechanics. 2017;813.

[45] Park C. Assessment of two-temperature kinetic model for ionizing air. Journal of Thermophysics and Heat Transfer. 1989;3:233-44.

[46] Millikan RC, White DR. Systematics of vibrational relaxation. The Journal of chemical physics. 1963;39:3209-13.

[47] Shi L. Assessment of vibrational non-equilibrium effect on detonation. Hong Kong: Department of Mechanical Engineering, The Hong Kong Polytechnic University; 2018.

[48] Knab O, Fruehauf HH, Messerschmid EW. Theory and validation of the physically consistent coupled vibration-chemistry-vibration model. Journal of Thermophysics and Heat Transfer. 1995;9:219-26.

[49] McBride BJ, Zehe MJ, Gordon S. NASA Glenn coefficients for calculating

References

thermodynamic properties of individual species. 2002.

[50] Law CK. Combustion physics. New York: Cambridge University Press; 2006.

[51] Kee RJ, Rupley FM, Meeks E, Miller JA. CHEMKIN-III: A FORTRAN chemical kinetics package for the analysis of gas-phase chemical and plasma kinetics. United States1996.

[52] Chang S-C. The method of space-time conservation element and solution element—a new approach for solving the Navier-Stokes and Euler equations. Journal of Computational Physics. 1995;119:295-324.

[53] Wen CY, Saldivar Massimi H, Shen H. Extension of CE/SE method to non-equilibrium dissociating flows. Journal of Computational Physics. 2018;356:240-60.

[54] Shen H, Wen C-Y. Theoretical investigation of shock stand-off distance for non-equilibrium flows over spheres. Chinese Journal of Aeronautics. 2018;31:990-6.

[55] Shen H, Liu K-X, Zhang D-L. Three-Dimensional Simulation of Detonation Propagation in a Rectangular Duct by an Improved CE/SE Scheme. Chinese Physics Letters. 2011;28:124705.

[56] Shen H, Wen C-Y, Parsani M, Shu C-W. Maximum-principle-satisfying space-time conservation element and solution element scheme applied to compressible multifluids. Journal of Computational Physics. 2017;330:668-92.

[57] Shen H, Wen C-Y, Zhang D-L. A characteristic space–time conservation element and solution element method for conservation laws. Journal of Computational Physics. 2015;288:101-18.

[58] Shen H, Wen C-Y. A characteristic space–time conservation element and solution element method for conservation laws II. Multidimensional extension. Journal of Computational Physics. 2016;305:775-92.

[59] Short M, Quirk JJ. On the nonlinear stability and detonability limit of a detonation wave for a model three-step chain-branching reaction. Journal of Fluid Mechanics. 1997;339:89-119.

[60] Uy KCK, Shi L, Wen CY. Chemical reaction mechanism related vibrational nonequilibrium effect on the Zel'dovich−von Neumann−Döring (ZND) detonation model. Combustion and Flame. 2018;196:174-81.

[61] Sichel M, Tonello N, Oran E, Jones D. A two–step kinetics model for numerical simulation of explosions and detonations in H2–O2 mixtures. Proceedings of the Royal Society of London A: Mathematical, Physical and Engineering Sciences: The Royal Society; 2002. p. 49-82.

[62] Burke MP, Chaos M, Ju Y, Dryer FL, Klippenstein SJ. Comprehensive H2/O2 kinetic model for high-pressure combustion. International Journal of Chemical Kinetics. 2012;44:444-74.

[63] Uy KCK, Shi L, Wen CY. Prediction of half reaction length for H2O2Ar detonation

with an extended vibrational nonequilibrium Zel'dovich −von Neumann −Döring (ZND) model. International Journal of Hydrogen Energy. 2019;44:7667-74.

[64] Taylor B, Kessler D, Gamezo V, Oran E. The Influence of Chemical Kinetics on the Structure of Hydrogen-Air Detonations. 50th AIAA Aerospace Sciences Meeting including the New Horizons Forum and Aerospace Exposition: American Institute of Aeronautics and Astronautics; 2012.

[65] Skrebkov OV. Vibrational non-equilibrium in the hydrogen–oxygen reaction. Comparison with experiment. Combustion Theory and Modelling. 2015;19:131-58.

[66] Buckmaster JD, Ludford GSS. The effect of structure on the stability of detonations I. Role of the induction zone. Symposium (International) on Combustion. 1988;21:1669-76.

[67] Stewart DS, Kasimov AR. State of Detonation Stability Theory and Its Application to Propulsion. Journal of Propulsion and Power. 2006;22:1230-44.

[68] Kabanov DI, Kasimov AR. Linear stability analysis of detonations via numerical computation and dynamic mode decomposition. Physics of Fluids. 2018;30:036103.